UNIVERSITY OF CALIFORNIA, SAN DIEGO

Star Formation with Adaptive Mesh Refinement and Magnetohydrodynamics

A dissertation submitted in partial satisfaction of the
requirements for the degree
Doctor of Philosophy

in

Physics

by

David C. Collins

Committee in charge:

Professor Michael L. Norman, Chair
Professor Paolo Padoan, Co-Chair
Professor Professor Daniel Dubin
Professor Professor Michael Holst
Professor Professor Barney Rickett

2009

The dissertation of David C. Collins is approved, and it is acceptable in quality and form for publication on microfilm and electronically:

_____

_____

_____

_____
Co-Chair

_____
Chair

University of California, San Diego

2009

DEDICATION

To Maggie, My Love.

And to our son. I'll see you next week.

TABLE OF CONTENTS

LIST OF FIGURES

LIST OF TABLES

ACKNOWLEDGEMENTS

I would like to thank my advisors, Mike Norman and Paolo Padoan, for the support and guidance they have given me on all facets of this project. It has been wonderful to learn so much from both of you.

This work would not have been possible without the extensive work and development by Hao Xu. His hard work and input have been invaluable.

Brian O'Shea has been without peer in helping me get up the knowledge ramp in many aspects of my graduate career, from software to physics to politics.

Everyone in the Laboratory for Computational Astrophysics, especially Alexei Kritsuk, Rick Wagner, James Bornder, and Robert Harkness, has all been extremely helpful on this development project. I've learned a huge amount from all of you.

My friends Anna-Clare Milazzo and Novimir Pablant have been extremely supportive through this process, helped me unwind and helped me stay on course when things were most challanging. Jeff Terich and Candice Eley have offered creative outlets and life outside of the lab that has helped keep me sane. Everyone else that I didn't mention, thank you.

I would like to thank my parents, Frank Collins and Louise Lawarre, for teaching me how to ask questions and love the beauty and wonder of the world so much.

Finally I would like to thank my wife, Marguerite, for her caring, devotion, and love; and for stepping up to the challenge of getting our lives ready for the next phase while I was busy finishing this one. And our little buddy, whose timing is spectacular; who has changed me even though I haven't seen his face yet. I didn't know I would be this excited. I love you both.

Chapter 1 has been submitted in full for publication in The Astrophysical Journal Suppliment series as Collins, D.C., Xu, H., Norman, M.L., Li,H., & Li., S "Cosmological AMR MHD with Enzo". The dissertation author was the primary author on this work.

VITA

2001	B. A. in Mathematics *cum laude*, University of Cincinnati
2001	B. S. in Physics *cum laude*, University of Cincinnati
2002-2005	Graduate Teaching Assistant, University of California, San Diego
2009	Ph. D. in Mathematics, University of California, San Diego

PUBLICATIONS

Xu, H., O'Shea, B. W., **Collins, D. C.**, & Norman, M.L. "The Biermann Battery in Cosmological MHD Simulations of Population III Star Formation", ApJL, 688, L57

Xu, H., Li., H, **Collins, D. C.**, Li, S., & Norman, M. L. "Formation of X-Ray Cavities by the Magnetically Dominated Jet-Lobe System in a Galaxy Cluster", ApJL, 681, L61

Collins, D.C., Xu, H., Norman, M.L., Li,H., & Li., S "Cosmological AMR MHD with Enzo", ArXiv e-prints 0902.2594

ABSTRACT OF THE DISSERTATION

Star Formation with Adaptive Mesh Refinement and Magnetohydrodynamics

by

David C. Collins
Doctor of Philosophy in Physics

University of California San Diego, 2009

Professor Michael L. Norman, Chair

Professor Paolo Padoan, Co-Chair

In this thesis, we develop an adaptive mesh refinement (AMR) code including magnetic fields, and use it to perform high resolution simulations of magnetized molecular clouds. The purpose of these simulations is to study present day star formation in the presence of turbulence and magnetic fields.

We first present MHDEnzo, the extension of the cosmology and astrophysics code Enzo to include the effects magnetic fields. We use a higher order Godunov Riemann solver for the computation of interface fluxes; constrained transport to compute the electric field from those interface fluxes, which advances the induction equation in a divergence free manner; divergence free reconstruction technique to interpolate the magnetic fields to fine grids; operator splitting to include gravity and cosmological expansion.

We present a series of test problems to demonstrate the quality of solution achieved. Additionally, we present several other solvers that were developed along the way.

Finally we present the results from several AMR simulations that study isothermal turbulence in the presence of magnetic fields and self gravity. Ten simulations with initial Mach number 8.9 were studied varying several parameters; virial parameter α from 0.52 to 3.1; whether they were continuously stirred or

allowed to decay; and the number of refinement levels (4 or 6). Measurements of the density probability density function (PDF) were made, showing both the expected log normal distribution and an additional power law. Measurements of the line of sight magnetic field vs. column density are done, giving excellent agreement with recent observations. The line width vs. size relationship is measured and compared with good agreement to observations, reproducing both turbulent and collapse signatures

The core mass distribution is measured and agrees well with observations of Serpens and Perseus core samples, but the power-law distribution in Ophiuchus is not reproduced by our simulations.

Finally we attempt to make contact with recent theoretical predictions of the star formation rate. Our measured rate is significantly higher than predicted, indicating that our root grid resolution is likely too low. Nonetheless, the simulations presented here are the first of their kind, and the general agreement with observations indicates the promise of our approach. We conclude by outlining future work which will explore numerical systematics more fully, and make detailed contact with observations.

Draft 4, revision 1183, April 26, 2009

Chapter 1

Introduction

1.1 Unsolved Problems in Star Formation

Stars are the most important objects in the night sky. They are the source of almost all the light in the night sky, either directly or indirectly. They are the source of all the elements heavier than Lithium, many of which are quite important to life on earth. Much is know about the composition and evolution of stars. However, parts of their birth process is still largely a mystery. See McKee & Ostriker (2007) for a recent review. This is in part due to difficulty in observations, as most of the process happens in highly obscured regions of cold, dense molecular clouds; and in part due to the extremely complex nonlinear behavior of magnetized turbulence which is now recognized as a primary component in the process (Padoan & Nordlund, 2002; Mac Low & Klessen, 2004; McKee & Ostriker, 2007).

There are currently two important unsolved problems in star formation: the rate of star formation and the distribution of masses of the stars. In this work we will discuss the development of an Adaptive Mesh Refinement code that incorporates magnetohydrodynamics, and then try to shed some light on these two questions using it.

In the rest of this chapter, we will discuss observational and theoretical background needed for the turbulent fragmentation model of star formation, the paradigm explored in this work, and to put it in context of stars forming in the galaxy. In chapter 2, we will discuss the implementation of MHD in Enzo. Chapter

3 will discuss numerical development that happened along the way that, for various reasons that will be discussed, were not suited to the numerical rigors of supersonic turbulence. Finally in chapter 4 we will present results from some new simulations that attempt to test the best models currently available with the highest resolution simulations of self gravitating MHD ever performed. These simulations are the first to combine magnetic fields with adaptive mesh refinement to model the conditions and length scales of real star forming regions. We compare the results of supersonic isothermal turbulent simulations with theory and observations to begin to further validate the paradigm of isothermal MHD turbulence as the primary vehicle regulating star formation in present day galaxies.

Unfortunately, due to some numerical setbacks, this last section is still somewhat of a work in progress– all the previously computed data was invalidated by the discovery of a code bug at the beginning of February 2009, so all the data presented here has been freshly simulated analyzed in the recent weeks. The data we will present here is extremely promising, and presents tests of the theory never before performed.

1.2 Observational Overview

1.2.1 Stellar Birth

The formation of stars has been broken into 4 distinct classes. Figure 1.1 shows a schematic of these 4 classes, plus the pre main sequence phase, and the main sequence star. We will be focusing on the stages leading up to this process, but it is useful to make the full connection to the stars in the night sky first. The first four stages are as follows:

Class 0 Dark cloud. These are classified by dark, cold (10 K) condensations roughly 10^4 AU in size (panel b in figure 1.1). It is the formation of these objects that we will be concerned with in this work.

Class I Collapsing protostar and the onset of deuterium burning. These objects now have an embedded protostar at the center, visible in the infrared, but

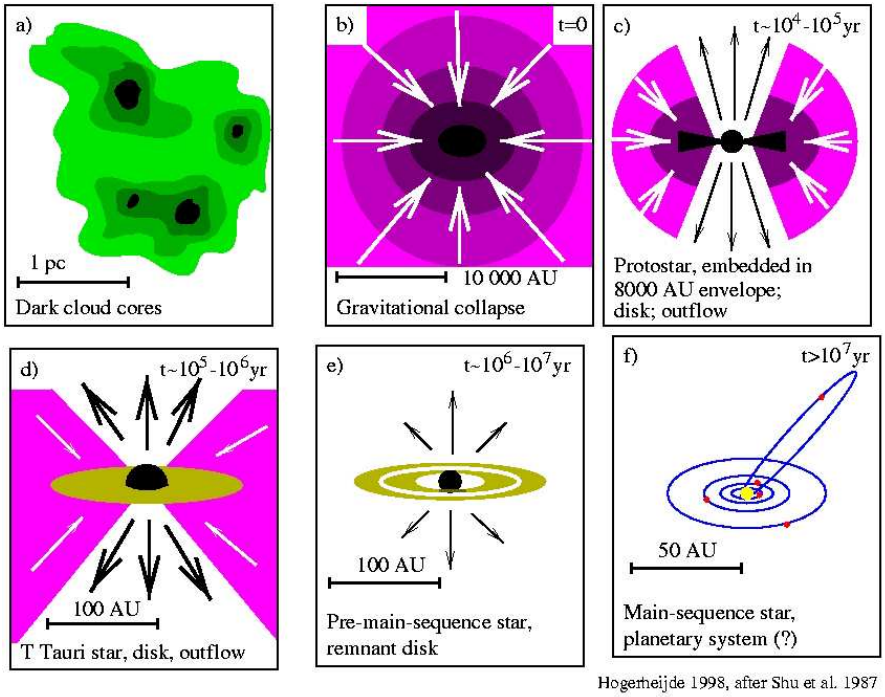

Figure 1.1: A schematic figure showing the six stages of stellar birth.

without sensitive infrared measurements, they are difficult to distinguish from Class 0 protostars. (panel c)

Class II Classical T-Tauri star. The star almost reached its final mass, and is classified by strong X-ray emission, due to the strong stellar magnetic field. There is now an identifiable circumstellar disk, and frequently a strong jet. (panel d)

Class III Weak Lined T-Tauri star. The disk has now been almost entirely been evaporated, launched through the jet, or been accreted onto the star. (panel e)

Zero Age Main Sequence The star is born onto the main sequence, and has decoupled from its birth environment.

We will be primarily concerned with the first two phases of this process: the formation and initial contraction of the cores.

1.2.2 Molecular Clouds

Molecular Clouds (MCs) and their larger friends Giant Molecular Clouds (GMCs) are massive structures that are the birth places for all present day star formation. They are large, ranging from $10^4 - 10^7 \mathrm{M}_\odot$, cold, in the $3 - 15K$ range, turbulent, and have number densities roughly $100\mathrm{cm}^{-3}$. Figure 1.2 shows an image of the Taurus molecular cloud mapped in ^{12}CO from Goldsmith et al. (2008). This figure shows two key features. First, the hierarchical structure of clumps inside of other dense clumps suggestive of its turbulent nature; and second, the elongated structures in the top left corner, which are most likely caused by freezing of material along magnetic fields. This map of the Taurus cloud represents the key features we wish to model. Padoan et al. (1999) performed a statistical comparison between numerical simulations of ideal super-Alfvénic MHD turbulence and the Perseus molecular cloud and found extremely good match on a number of statistical measures, strongly indicating that super-Alfvénic MHD turbulence is the correct underlying physics in these clouds. In this work I adopt this hypothesis and carry out numerical simulations to test its predictions, including greatly improved spatial resolution and self gravity.

1.2.3 Mass Distribution

The initial mass function (IMF) of stars was first measured by Salpeter (1955) who fit the number of stars in the solar neighborhood as a function of mass to a power law:

$$dN = 0.03(\frac{M}{\mathrm{M}_\odot})^{-1.35} d\ln M. \tag{1.1}$$

Highly detailed studies by Chabrier (2003), who fit multiple components of the galaxy and found that the distribution fits a power law above $1\mathrm{M}_\odot$, and a log normal below. Kroupa (2001) argue that the IMF is universal, indicating that a general underlying physical mechanism is responsible for star formation everywhere. The origin of the shape of the IMF is an important question in star formation. Turbulence begins to explain this distribution quite naturally, as we will discuss in sections 1.4.2 and 4.3.

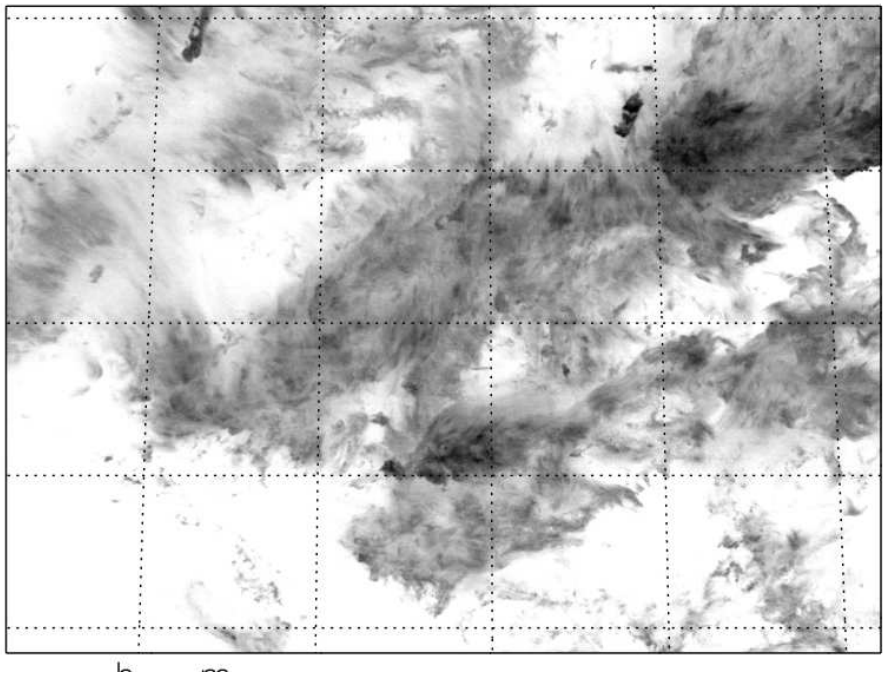

Figure 1.2: An image of the Taurus molecular cloud in ^{12}CO, from Goldsmith et al. (2008)

1.2.4 Velocity Statistics

Larson (1981) measured the velocity differences between a large number of clouds, and found that the line width σ scaled with the object size ℓ as

$$\sigma \propto (\ell)^{0.5} \tag{1.2}$$

which is consistent with supersonic turbulence (Passot et al., 1988), as will be discussed in section 1.3

1.2.5 Star Formation Rate

As first pointed out by Zuckerman & Evans (1974), if all molecular clouds were collapsing at the infall rates that were presumed from the super thermal velocities observed in molecular clouds, the star formation rate in the galaxy would be $30-300 M_{\odot} yr^{-1}$. However, the observed rate is only $4 M_{\odot} yr^{-1}$. This discrepancy is a fundamental problem in the theory of star formation, and many explanations

have been suggested to explain it (Shu et al., 1987; McKee & Ostriker, 2007). Mouschovias (1976) suggested that magnetic fields suspend the clouds, and the super thermal velocities were caused by Alfvén waves propagating through the cloud. This paradigm began to lose favor in the mid to late 1990s as works like Padoan (1995), Vazquez-Semadeni (1994), and Ostriker et al. (2001) began to demonstrate the strengths of the turbulent model. Krumholz & McKee (2005) presented a new theory that could predict the star formation rate using turbulent fragmentation, claiming another strong victory. This model will be discussed in depth and compared to our numerical work in sections 1.4.3 and 4.9.

1.2.6 Observed Magnetic Fields

The only known method of directly measuring the strength of magnetic fields in molecular clouds is through Zeeman splitting. Other methods, such as starlight polarization or dust grain alignment, provide estimates of field strength but not direct measurements. Zeeman splitting occurs when the magnetic field in the gas splits a hyperfine state in the gas in the cloud. Due to the angular momentum differences between the new split levels, the newly energy segregated photons also have different circular polarizations. Taking the difference of the two states gives (eventually) the strength of the magnetic field along the line of sight. An excellent review of measurements of magnetic fields in the galaxy can be found in Crutcher et al. (2003).

Troland & Crutcher (2008) and Falgarone et al. (2008) have recently published Zeeman splitting measurements of clouds using OH and CN, respectively. These results will be used for comparison in chapter 4

1.3 Turbulence

The most important advance in turbulence theory came in 1941 when Kolmogorov published his seminal theory on turbulence (Kolmogorov, 1941b,a); hereafter we will do as is done in the rest of the literature and refer to this as the K41 model. (These were recently translated in (Kolmogorov, 1991b,a)). His highly

phenomenological theory had several quite restrictive assumptions; that the fluid is spatially homogeneous, isotropic, inviscid, incompressible, and steady in time. The turbulent systems relevant for star formation are none of those things, and additionally they are magnetized. However, the results he found in 1941 are a useful starting point when relaxing those assumptions. First we will discuss this idealized picture.

1.3.1 Kolmogorov 1941 (K41)

The basic picture is one of a collection of eddies of various size scales. See figure 1.3 for a cartoon. These eddies are classified in three spatial regimes. The largest spatial scale is the driving scale. This is the source of the motions, and can be due to the motion of a spoon in a coffee cup or large scale differential rotation of the galaxy, to name a few. Eddies generated at this driving scale generate eddies at smaller scales. The physics of this cascade depends on the physics involved: in incompressible hydrodynamics, this happens through the stretching of vortex tubes and the shearing apart of eddies. The motion to smaller scales is a lossless process, and local in terms of the size of the eddy: eddies at scale ℓ generate eddies at only slightly smaller scales $\ell - \delta$. Motion of energy continue down to smaller and smaller scales through the second spatial regime, the inertial scale. This is characterized by a power law slope in the energy

$$E(k) \propto k^{-5/3}. \tag{1.3}$$

Derivation of this is fairly straight forward. Assume that on a given scale ℓ one has velocity v_ℓ. This should be thought of as the velocity differences across the structure ℓ, not the bulk motion of structures of that size. Energy transfer should happen on a timescale comparable to the circulation time for that eddy,

$$t_\ell = \ell / v_\ell.$$

Thus the energy transfer rate, which is assumed to be a constant of the fluid,

$$\epsilon = v_\ell^2 / t_\ell \tag{1.4}$$

$$= v_\ell^3 / \ell \tag{1.5}$$

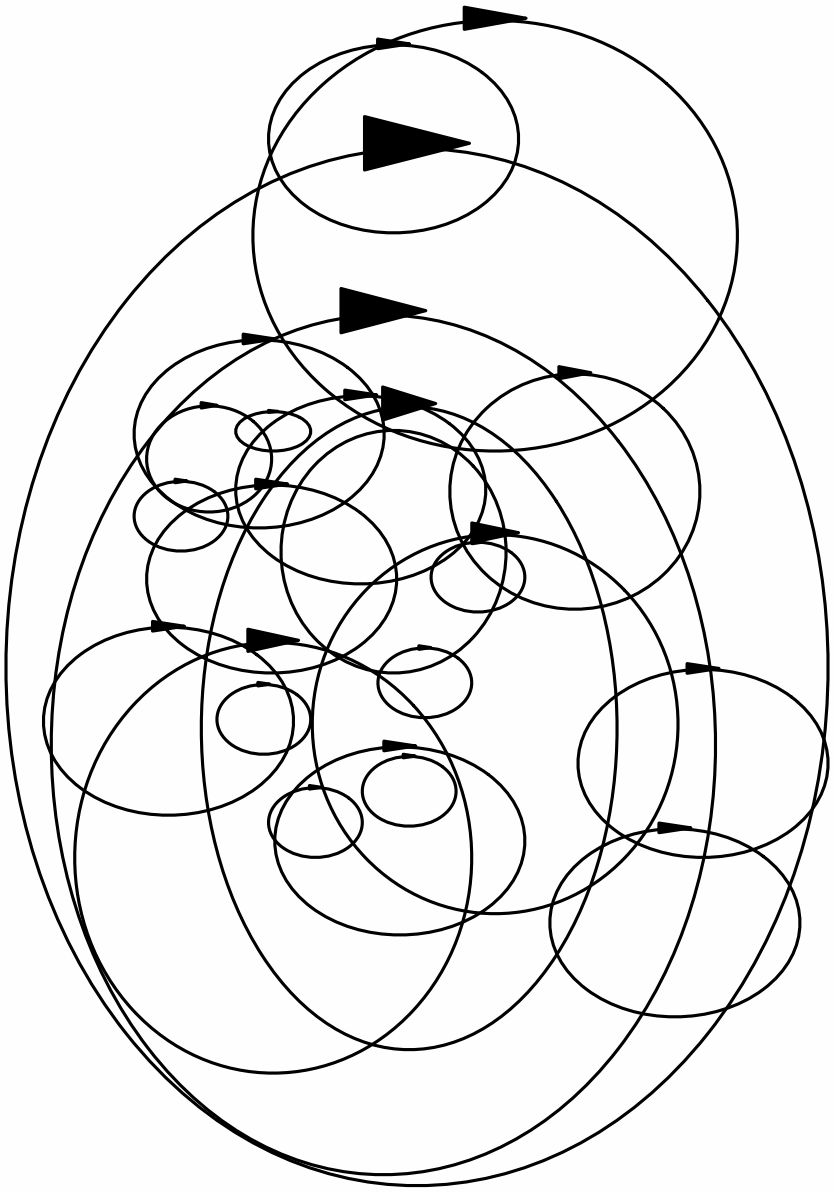

Figure 1.3: Turbulence in the K41 model is viewed as a collection of eddies of various sizes. Larger eddies transfer energy to smaller eddies.

from which we have

$$v_\ell = (\epsilon \ell)^{1/3}, \tag{1.6}$$

$$E_\ell = v_\ell^2 \tag{1.7}$$

$$= \epsilon^{2/3} \ell^{2/3} \tag{1.8}$$

where we have assumed $\rho = 1$, as is appropriate for incompressible fluids. Upon Fourier transform of equation 1.8, we have

$$E_k = \epsilon^{2/3} k^{-5/3}$$

The cascade ends where the dissipation length scale ℓ_D is reached at small wavelengths. This the length scale where the atomic forces work to dissipate the fluid motions. This can be estimated as the length scale where the fluid dissipation rate is on the order of the cascade transfer rate,

$$\frac{v_{\ell_D} \eta}{\ell_D^2} \approx \frac{v_{\ell_D}^2}{t_{\ell_D}} \tag{1.9}$$

$$\frac{\eta}{\ell_D^2} \approx \frac{v_{\ell_D}}{\ell_D} \tag{1.10}$$

$$\approx \frac{(\epsilon \ell_D)^{1/3}}{\ell_D} \tag{1.11}$$

$$\ell_D \approx \left(\frac{\eta^3}{\epsilon} \right)^{1/4} \tag{1.12}$$

where η is the kinematic viscosity. In numerical simulations, this scale is severely unresolved. For galactic gas, this length scale is on the order of 50AU For the bulk of the simulations in this work, the finest resolution element is 1000AU, and the dissipation length scale is as much as 30 times that. Figure 1.4 shows a schematic of these length scales, and also mentions both the direct cascade and the inverse cascade. Only the direct cascade occurs in 3 dimensional fluid turbulence, but MHD has one quantity that exhibits an inverse cascade, which will be discussed next.

One significant shortcoming of this theory is that it assumes that energy dissipation is uniform. However, numerical and laboratory simulations indicate that turbulence is intermittent both spatially and temporally (Anselmet et al.,

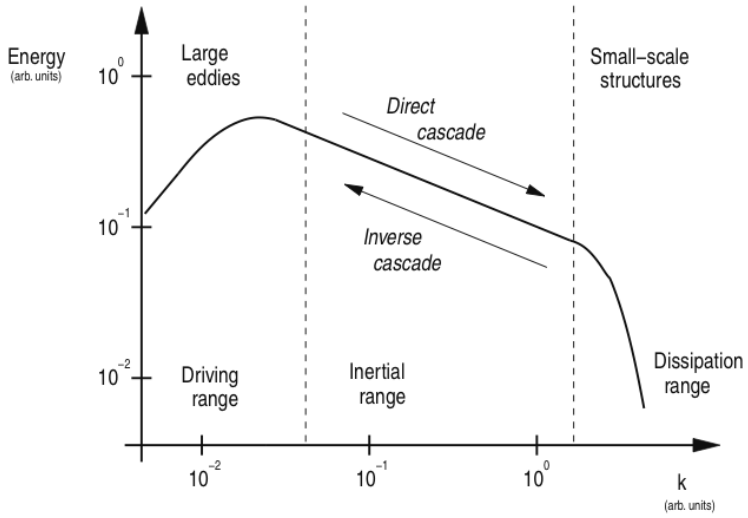

Figure 1.4: A schematic of the turbulent cascade, showing the turbulent generation scale at low k, the inertial range at intermediate k, and the dissipation range at high k. Taken from Müller (2009)

1984; Vincent & Meneguzzi, 1991; Müller & Biskamp, 2000). The most prominent and successful model that treats dissipation only in the most singular structures is the model of She & Leveque (1994). As we will not be exploring scalings outside of a very basic usage, we will only mention this here.

1.3.2 MHD Turbulence

Now we will present some of the deviations from the above picture caused by MHD effects. This work will not be testing the details of MHD turbulence, only using the results from turbulent environments, so we present this only for completeness of the overall picture of interstellar turbulence. MHD turbulence is both less well constrained theoretically and less well verified experimentally, and are still under much investigation.

The first major distinction with MHD is the fact that not all the quantities in MHD perform a direct cascade. The total energy, $E = 1/2 \int_V (v^2 + b^2) dV$, and cross helicity $H^C = 1/2 \int_V \mathbf{v} \cdot \mathbf{b}\ dV$, exhibits a direct cascade, but the magnetic helicity $H^M = 1/2 \int_V \mathbf{v} \cdot \mathbf{a}\ dV$ where $\mathbf{b} = \nabla \times \mathbf{a}$ defines the vector potential $\mathbf{a}$,

exhibits an inverse cascade. Structures in H^C transfer energy to larger scales. It is believed that this inverse cascade may be responsible, in some part, for the large scale magnetic fields observed in the galaxy.

MHD: Iroshnikov-Kraichnen

There are two major scaling arguments for MHD. The first is the Iroshnikov-Kraichnen (IK) relation (Iroshnikov, 1964; Kraichnan, 1965). This model retains the isotropy nature of the K41 model, which is a major source of criticism. IK uses the Elsässer variables $\mathbf{z}^{\pm} = \mathbf{v} \pm \mathbf{B}$, and considers the collision of counter-propagating waves, $\mathbf{z}^{+}$ vs $\mathbf{z}^{-}$. It is important that the waves are counter propagating, since co-propagating waves will never interact. This is not necessarily true in fluids with strong density gradients (McKee & Zweibel, 1995), but that is beyond the scope of this model. IK then assumes that the background field B_0 is larger than the perturbations causing the waves $\delta v, \delta B$ (which clearly conflicts with the assumption of isotropy) and again examines the transfer timescales, as K41 does. They arrive at the scalings for energy and dissipation length

$$E_{IK}(k) \propto (\epsilon B_0)^{1/2} k^{-3/2} \tag{1.13}$$

$$\ell_{D,IK} = \left(\frac{B_0 \eta^2}{\epsilon} \right)^{1/3} \tag{1.14}$$

MHD: Goldreich-Sridhar

The other dominant MHD scaling model is due to Goldreich and Sridhar (Goldreich & Sridhar, 1995; Sridhar & Goldreich, 1994), hereafter GS. Essentially they assume that there is a balance between the Alfvén timescale for a propagation of disturbance of size λ, $\tau_\lambda = \lambda / B_0$ and the eddy turnover time for a disturbance of size ℓ perpendicular to B_0, $\tau_\ell = \ell / z_\ell$, where z_ℓ is the amplitude of the disturbance. This yields two relations, one for the disturbances along B_0, and one for transverse scalings:

$$E_{k_\perp} \propto k_\perp^{-5/3} \tag{1.15}$$

$$E_{k_\parallel} \propto k_\parallel^{-2}. \tag{1.16}$$

1.3.3 Compressible Turbulence

The other major deviation from K41 at work in GMCs is the issue of compressibility. The Mach > 10 shocks developed in GMCs change the nature of the turbulence at least as much as the magnetic fields do. In a limiting case of infinitely compressible gas, Gotoh & Kraichnan (1993) examined turbulence in the Burgers equation, and found

$$E_{Burgers}(k) \propto \ k^{-2}.$$

Burgers equation is simply the Navier-Stokes equations without the pressure term or magnetic term. Thus a steeper spectrum than this would be quite surprising, since without the thermal and magnetic pressure terms opposing the shock, they can be essentially arbitrarily thin. And that is the most direct route to small structure.

Kritsuk et al. (2007) performed direct numerical simulations of isothermal Mach 6 shocks at extremely high resolution, and measured

$$E(k) \propto k^{-1.95}$$

which is much steeper than any of the other hydrodynamical models. They make contact with K41 by treating not the velocity v but the mass weighted velocity $u = \rho^{1/3}v$. This can be seen as replacing the energy transfer rate in equation 1.4 with the one that's proper to a compressible fluid, restoring the density:

$$\epsilon = \rho_\ell v_\ell^2 / t_\ell \tag{1.17}$$

which leads to

$$v_\ell = (\epsilon \ell / \rho_\ell)^{1/3} \tag{1.18}$$

$$u_\ell = (\epsilon \ell)^{1/3} \tag{1.19}$$

The scaling of this new quantity does numerically show a scaling exponent of $-5/3$, like K41.

1.3.4 The Decay of Turbulence

It has been shown by a number of works (Mac Low, 1999; Padoan & Nordlund, 1999; Ostriker et al., 2001) that supersonic turbulence decays in much less

than a free fall time, regardless of the presence of magnetic fields. Mac Low (1999) showed that the decay timescale $\tau_D = E_{kinetic}/\dot{E}_{kinetic}$ decays as

$$\tau_D/t_{ff} \simeq 3.9\frac{\lambda_{Turb}/\lambda_J}{\mathcal{M}} \tag{1.20}$$

where λ_{Turb} is the length scale of the initial perturbation, $\lambda_J = \sqrt{3\pi/32G\rho}$ is the Jeans Length, t_{ff} is the free fall time, and $\mathcal{M}$ is the RMS Mach number. However, it has been shown that clouds are likely a few free fall times old (see Mac Low & Klessen (2004) for a review), though that number is still under debate. Gravitational and magnetorotational instabilities in the galactic disk, supernovae, and stellar feedback have all been cited as plausible sources for this turbulence, but no definitive answer has been found yet.

1.4 Consequences of Turbulence

There are several significant consequences that lead us to believe that this is the dominant paradigm for star formation. With one mechanism star formation can begin to explain cloud lifetimes, the mass distribution, and the star formation rate.

1.4.1 Dual Role of Turbulence

Turbulence in molecular clouds does essentially two things: first, it prevents the global collapse of gravitationally unstable clouds; and second, it provides the density enhancements that actually do form regions that locally collapse. Klessen et al. (2000) did a series of runs varying the length scale of the driving and the Mach number in turbulent boxes both globally supported and globally unsupported. Unsurprisingly, all the unsupported runs formed stars, but even the globally supported simulations formed stars except for one case where the box was driven below the Jeans length. In almost all cases collapse was slowed to much lower rates than what one would expect from collapse alone. This is the central role of turbulence in molecular clouds– permitting some slow collapse, but preventing the cloud as a whole from collapsing entirely.

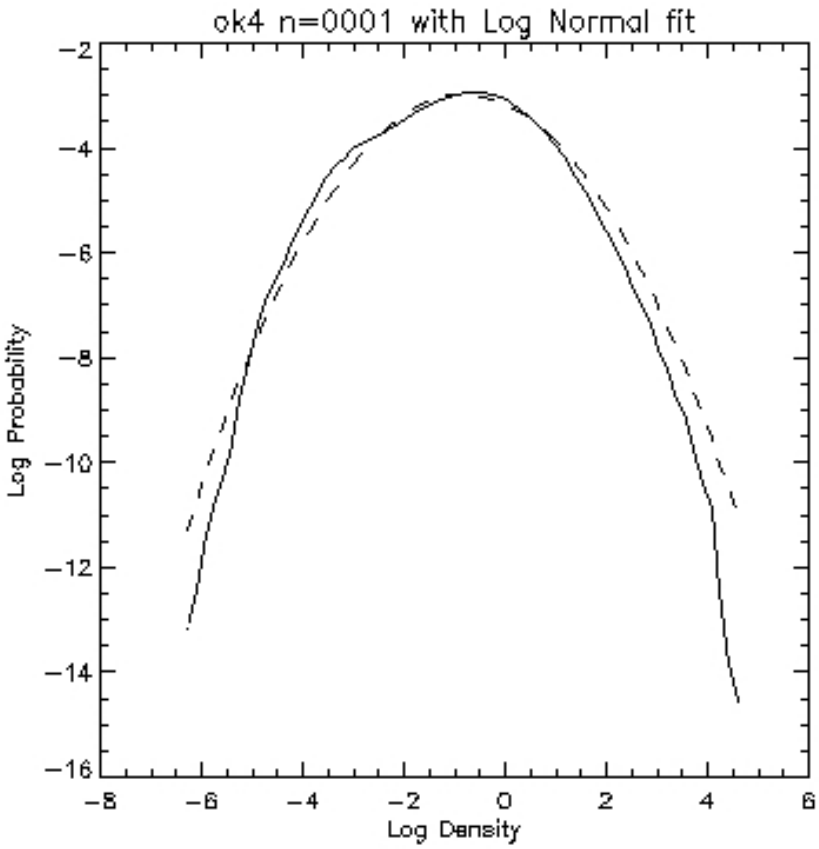

Figure 1.5: The density PDF of an isothermal MHD simulation with a fit to a lognormal

1.4.2 PDF

As will be discussed in section 4.3, the density probability distribution function (PDF) in isothermal turbulence produces a lognormal distribution. This distribution function can be used to begin to describe both the star formation rate and the mass distribution of clumps that will eventually become stars. Figure 1.5 shows the density PDF from a snapshot from the initial conditions from one of the runs presented in this work, with the fit to a lognormal demonstrating this distribution. We can see that the lognormal is a good fit to the density distribution over several orders of magnitude.

1.4.3 Star formation rate

Krumholz & McKee (2005), building on the work of Padoan (1995), use the density PDF of isothermal turbulence to predict the rate at which the star formation efficiency (the fraction of the cloud's mass in stars) of a cloud increases relative to its free fall time. They dub this "star formation rate per free fall time," SFR_{ff}, and define it as "the fraction of a cloud that can become stars in one free fall time." In essence, they define a length scale below which the velocity differences across a region are too small to support the clump against its own collapse. This in turn defines a density scale, and the gas above that density scale, according to this model, will collapse to form stars in one free fall time. In section 4.9, we discuss this model in greater detail, as well as how it compares to our simulations, and discuss some potential problems with it.

1.4.4 IMF

Padoan & Nordlund (2002) use the density PDF to predict the mass distribution of prestellar clumps in a cloud. They combine the shock jump conditions, an assumption about structure scaling, and the density PDF to model structures that are likely to collapse to form stars, and successfully reproduce key features of the observed mass distribution. In section 4.8, we discuss this model in more detail and compare it and observations to our simulations.

1.5 Numerics: AMR MHD

Star formation involves a huge dynamic range of length and mass scales. As discussed in section 1.2.2, mean densities of the progenitor clouds have number densities of 100cm^{-3}, and length scales of 10 pc or more. The prestellar cores we wish to study, on the other hand, have densities of 5×10^7cm^{-3} and length scales of 1000AU. With an outer box of 10pc, one would need 10^4 zones on a side to resolve 100AU, which would only resolve the objects by 10 zones; hardly enough to say anything meaningful about them. This scale of simulation, if done

at fixed resolution, may not be feasible in our lifetime. This is where Adaptive Mesh Refinement comes in.

Adaptive Mesh Refinement (AMR) is a technique of increasing resolution only where its needed. A simulation begins with a volume-filling regular mesh of zones. As the error in the solution increases, by whatever metric one chooses for "error", rectangular patches of a higher spatial resolution are added to those regions. Both the initial parent grid and new refined region are solved as if the other weren't there, and then the solutions are synchronized at the end of an integration timestep. This is discussed at length in section 2.1.11. In this work, we take the existing AMR framework implemented in the Enzo code and add magnetic fields. This was a substantial undertaking, as the magnetic fields require a different data stencil than the initial code structures used, so this required a substantial amount of reworking; magnetic fields also have the constraint $\nabla \cdot \mathbf{B} = 0$, which not only requires fine tuning of the algorithm, but also brings to light other numerical glitches in the software. Additionally, we wrote or installed four different MHD patch solvers in an attempt to find one that is both stable and accurate enough to tackle the extremely rigorous numerical challenge of super-Alfvénic MHD turbulence with gravity.

Chapter 2

Enzo MHD: Current Method

In this chapter, we describe the final version of the source code used in EnzoMHD. The earlier solvers will be described in chapter 3

This chapter is almost identical to the paper submitted to the Astrophysical Journal Supplement Series. Two major differences are in the test sections. We have omitted the section on galaxy clusters, and inserted section 2.2.1 on turbulence tests.

EnzoMHD is also a purpose code. In this chapter, we will discuss it as a cosmological code, but all the same machinery applies in non-cosmological mode. All algorithms used here reduce to the non-cosmological limit by setting $a \rightarrow 1, \dot{a} \rightarrow 0$, and $\ddot{a} \rightarrow 0$. This removes any frame dependent terms in the equations.

We will describe the numerical procedures in section 2.1, present test problems in section 2.2. In section 2.5 we present a simplified schematic to unify the pieces of the solver, and in sections 2.4 and 2.3 we expand on some of the more complex numerical procedures.

2.1 Numerics

2.1.1 Cosmological MHD Equations

EnzoMHD solves the MHD equations in a comoving coordinate frame.

$$\frac{\partial \rho}{\partial t} + \frac{1}{a}\nabla \cdot (\rho \mathbf{v}) = 0 \tag{2.1}$$

$$\frac{\partial \rho \mathbf{v}}{\partial t} + \frac{1}{a}\nabla \cdot (\rho \mathbf{v}\mathbf{v} + \bar{p} - \mathbf{B}\mathbf{B}) = -\frac{\dot{a}}{a}\rho \mathbf{v} - \frac{1}{a}\rho \nabla \Phi \tag{2.2}$$

$$\frac{\partial E}{\partial t} + \frac{1}{a}\nabla \cdot [\mathbf{v}(\bar{p} + E) - \mathbf{B}(\mathbf{B} \cdot \mathbf{v})] = -\frac{\dot{a}}{a}(\rho v^2 + \frac{2}{\gamma - 1}p + \frac{B^2}{2}) - \frac{\rho}{a}\mathbf{v} \cdot \nabla \Phi \tag{2.3}$$

$$\frac{\partial \mathbf{B}}{\partial t} - \frac{1}{a}\nabla \times (\mathbf{v} \times \mathbf{B}) = -\frac{\dot{a}}{2a}\mathbf{B} \tag{2.4}$$

with the equation of state

$$E = \frac{1}{2}\rho v^2 + \frac{p}{\gamma - 1} + \frac{1}{2}B^2 \tag{2.5}$$

$$\bar{p} = p + \frac{1}{2}B^2 \tag{2.6}$$

Here, ρ is the comoving density, p is the comoving gas pressure, v is the proper peculiar velocity, $\mathbf{B}$ is the comoving magnetic field, E is the total peculiar energy per unit comoving volume, $\bar{p}$ is the total comoving pressure, γ is the ratio of the specific heats, Φ is the proper peculiar gravitational potential from both dark-matter and baryons, $a = (1 + z_i)/(1 + z)$ is the expansion factor and t is time.

In this formulation, the comoving quantities that are evolved by the solver are related to the proper observable quantities by the following equations:

$$\rho_{proper} = \rho * a(t)^3 \tag{2.7}$$

$$p_{proper} = p_{comoving} * a^3 \tag{2.8}$$

$$\mathbf{v}_{proper} = \mathbf{v}_{comoving} - \dot{a}\mathbf{x} \tag{2.9}$$

$$\Phi_{proper} = \Phi - \frac{1}{2}a\ddot{a}\vec{x}^2 \tag{2.10}$$

$$\mathbf{B}_{proper} = \mathbf{B}_{comoving} a^{\frac{-3}{2}} \tag{2.11}$$

It should be noted that the relationship between $\mathbf{B}_{proper}$ and $\mathbf{B}_{comoving}$ in equation 2.11 is different than that stated in other cosmological MHD codes like Li

et al. (2008). This is due to the additional expansion factor that we use in equation 2.4. The proper magnetic field decreases proportional to a^{-2} in all formulations of the cosmological MHD equations, but in the formulation we use one half power of a is included as a comoving source term and is due to the redshifting of the photons that carry the magnetic field.

For non-cosmological simulations, the same equations hold, but with with $a = 1, \dot{a} = 0$ and $\ddot{a} = 0$. This effectively removed each appearance of a from the left hand side, and eliminates the terms involving $\dot{a}$ from the right. For ease of reference, these are:

$$\frac{\partial \rho}{\partial t} + \nabla \cdot (\rho \mathbf{v}) = 0 \tag{2.12}$$

$$\frac{\partial \rho \mathbf{v}}{\partial t} + \nabla \cdot (\rho \mathbf{v}\mathbf{v} + \bar{p} - \mathbf{B}\mathbf{B}) = -\rho \nabla \Phi \tag{2.13}$$

$$\frac{\partial E}{\partial t} + \nabla \cdot [\mathbf{v}(\bar{p} + E) - \mathbf{B}(\mathbf{B} \cdot \mathbf{v})] = -\mathbf{v} \cdot \nabla \Phi \tag{2.14}$$

$$\frac{\partial \mathbf{B}}{\partial t} - \nabla \times (\mathbf{v} \times \mathbf{B}) = 0 \tag{2.15}$$

with the same equation of state, equations 2.5 and 2.6. Here, ρ is the density, p is the gas pressure, v is the velocity, $\mathbf{B}$ is the magnetic field, E is the total energy per unit volume, $\bar{p}$ is the total gas pressure, γ is the ratio of the specific heats, Φ is the gravitational potential. The mechanism to switch between the two systems of equations will be described in section 2.1.6.

To solve these equations, we operator split eqns (2.1)-(2.4) into four parts: the left hand side of equations (2.1)-(2.3), the left hand side of equation (2.4), the gravitational acceleration (the two terms involving $\nabla\Phi$), and the expansion terms (the two terms involving $\dot{a}$.) These will be discussed in sections 2.1.6 - 2.1.7. In section 2.1.10, we will discuss the dual energy formulation in Enzo for hypersonic flows, and in section 2.1.11 we will discuss the Adaptive Mesh Refinement algorithm. We first discuss the data structures used to carry all this data in section 2.1.2

In the following, we will often have cause to separate the purely fluid dynamical quantities $\rho, \vec{v}, E$ from the magnetic field $\vec{B}$. Unless otherwise noted, 'fluid

quantities' will refer to the former only.

For ease of reference, we have supplied a schematic summary of the steps involved in section 2.5.

2.1.2 Data Structure

In Enzo, both parallelism and AMR are done in block decomposed manner. Each patch of space, called a `grid`, is treated as a unique computational problem with Dirichlet boundary conditions which are stored in a number of Ghost Zones (see section 2.1.5.) The number of ghost zones depends on the method used. The pure-hydro methods in Enzo, ZEUS and PPM, use 3 ghost zones. The method we describe here uses 5 ghost zones.

Grids are arranged in a strictly nested hierarchy, with each grid having a cell width half that of its parent (pure hydro Enzo can take any integer refinement, but the interpolation for MHD is restricted to factors of 2.) See figure 2.1. Each processor keeps a copy of the entire hierarchy, while only one of the processors actual stores the data.

For all physics modules described in this paper, an individual grid cares not for where it sits in space or the hierarchy, and communicates with other grids only through boundary condition fills (section 2.1.5) and the AMR cycle (section 2.1.11).

EnzoMHD in its default mode tracks 14 fields, stored at 3 different points of the cell. The 5 hydrodynamic quantities, $\rho, \mathbf{v}, E_{total}$ are stored at the center of the cell, denoted (i, j, k), and represent the volume average of the respective quantities. These are the same quantities stored in non-MHD Enzo.

EnzoMHD tracks 2 copies of the magnetic field and the electric field. One copy of the magnetic field is stored in the face of the cell perpendicular to that field component, and represents the area average of that field component over that face. This is the primary representation of the magnetic field. So $B_{f,x}$ is stored in the center of the x face, denoted $(i - \frac{1}{2}, j, k)$, $B_{f,y}$ in the y face at $(i, j - \frac{1}{2}, k)$, and $B_{f,z}$ in the z face at $(i, j, k - \frac{1}{2})$. It is this field that remains divergence free under

the cell centered divergence operator:

$$\begin{aligned}\nabla \cdot \mathbf{B_f} =& \frac{1}{\Delta x}(B_{f,x,i+\frac{1}{2},j,k} - B_{f,x,i-\frac{1}{2},j,k}) + \\ & \frac{1}{\Delta y}(B_{f,y,i,j+\frac{1}{2},k} - B_{f,y,i,j-\frac{1}{2},k}) + \\ & \frac{1}{\Delta z}(B_{f,z,i,j,k+\frac{1}{2}} - B_{f,z,i,j,k-\frac{1}{2}})\end{aligned} \tag{2.16}$$

The magnetic data structures are one element longer in each longitudinal direction, so for an $nx \times ny \times nz$ grid patch, the $B_{f,x}$ structure is $(nx+1) \times ny \times nz$.

The second representation of the magnetic field is centered with the fluid quantities at the center of the cell. This field is used wherever a cell centered magnetic quantity is needed, most notably in the hyperbolic solver in section 2.1.6. It's equal to the first order average of the face centered magnetic field:

$$\begin{aligned}B^{n+1}_{c,x,i,j,k} &= 0.5 * (B_{f,x,i+\frac{1}{2},j,k} + B_{f,x,i-\frac{1}{2},j,k}) \\ B^{n+1}_{c,y,i,j,k} &= 0.5 * (B_{f,y,i,j+\frac{1}{2},k} + B_{f,y,i,j-\frac{1}{2},k}) \\ B^{n+1}_{c,z,i,j,k} &= 0.5 * (B_{f,z,i,j,k+\frac{1}{2}} + B_{f,z,i,j,k-\frac{1}{2}})\end{aligned} \tag{2.17}$$

The final data structure used in EnzoMHD is the Electric Field, which is stored along the edges of the computational cell. This represents a linear average of the electric field along that line element. Each component is centered along the edge its parallel to, so E_x lies along the x edge of the cell at $(i, j-\frac{1}{2}, k-\frac{1}{2})$, etc. It is longer than the fluid fields by one in each transverse direction, so E_x would be $nx \times (ny+1) \times (nz+1)$.

Each grid also stores one copy of each of the above mentioned fields for use in assigning ghost zones to subgrids. This is described further in 2.1.5. A temporary field for fluxes is also stored, which exists only while the hyperbolic terms are being updated. This data structure is also stored on the faces of the zone. There are three fluxes for all 7 MHD quantities.

For other configurations of EnzoMHD, more or fewer fields may be used. In purely isothermal mode (which is at present an option only in EnzoMHD, not in Enzo) the total energy field is not tracked, and the isothermal sound speed is taken as a global scalar quantity. This reduces the number of fields tracked everywhere

the total energy shows up. With dual energy formalism on (see section 2.1.10) an additional field corresponding to either gas energy or entropy is stored, giving an additional field where needed. Future work will include multi-species chemistry and more complex cooling, which will include additional fields for each species.

2.1.3 Consistency

In several places throughout the flow of Enzo, there may be more than one data structure using and writing to a given variable at a given point in space. Ghost zones and face centered fields (fluxes and magnetic fields) are examples of this. In EnzoMHD, it is imperative that all data at a given point is identical, regardless of the data structure describing it. This may seem like an unnecessary comment, but it isn't; in pure hydro simulations, numerical viscosity will damp out small perturbations caused by slight inconsistencies in data description. Thus in practice, especially in large, stochastic simulations, errors can go unnoticed. Often these discrepancies are negligible, other times not, especially when one is concerned with the conservation of a particular variable, like $\nabla \cdot \mathbf{B}$. By construction EnzoMHD preserves $\nabla \cdot \mathbf{B}$ to machine precision, but it never *forces* $\nabla \cdot \mathbf{B} = 0$; so if it's not zero at the beginning of a time step, it's not going to be at the end, either. It is also worth mentioning that inconsistencies in any quantity will cause inconsistencies in the flow, which will in turn cause $\nabla \cdot \mathbf{B}$ issues. Thus any improper handling of *any* fluid quantity will cause errors in $\nabla \cdot \mathbf{B}$ that will persist and usually grow to catastrophic proportions in a relatively short period of time.

There is a prominent redundancy in the magnetic field, namely the field on the surface of the active zones of grids. See figure 2.2. Care is taken to include enough ghost zones, and frequent enough ghost zone exchange between grids, that after a time step, two neighboring grids have reached exactly the same answer on the surface between the two grids completely independently.

2.1.4 Time Stepping

Enzo uses hierarchical time stepping to determine it's time step. The minimum of 4 different criteria is taken for each level, which will be described in sections 2.1.4 - 2.1.4. Timesteps are taken in order of coarsest to finest, in a 'W' cycle. See figure 2.3. Given 3 levels, level 0 takes the first step of Δt. Then level 1 takes a single step of $\Delta t/2$. Then level 2 takes one step of $\Delta t/4$. Then, given that there are only three levels, it takes another timestep so it is temporally in line with the level above. The last three steps repeat: level 1 then takes its second and final step of $\Delta t/2$ so it is now at the same time as level 0, followed by two steps on level 2.

In principle, if a given level has a cell size Δx and the next level of refinement has cell size $\frac{\Delta x}{r}$, where r is the refinement factor, the more refined grid will have, in principle, time step size $\frac{\Delta t}{r}$. In Enzo, the step size is chosen for each level and each subgrid time step. In practice, owing to more finely resolved structures having slightly higher fast shock speeds, fine grids may in fact take more than r time steps for each parent grid step. In some rare cases, such as cosmological expansion limiting, a finer grid may take less than r steps.

Time Stepping: Hydro

For the hydrodynamics, the harmonic mean of the 3 Courant conditions is used. This was demonstrated to be the most robust time stepping criterion possible for multi dimensional flows by Godunov et al. (1961).

$$\begin{aligned} \Delta t_{hydro} =& \frac{1}{1/t_x + 1/t_y + 1/t_z} \\ t_x =& min(\frac{\Delta x}{c_{f,x}}) \\ t_y =& min(\frac{\Delta y}{c_{f,y}}) \\ t_z =& min(\frac{\Delta z}{c_{f,z}}) \end{aligned} \tag{2.18}$$

where the min is taken over the zones on a level, and $c_{f,x}, c_{f,y}$ and $c_{f,z}$ are the fast MHD shock speeds along each axis:

$$c_{f,x}^2 = \frac{1}{2}\left(a^2 + \frac{\mathbf{B}\cdot\mathbf{B}}{\rho} + \sqrt{(a^2 + \frac{\mathbf{B}\cdot\mathbf{B}}{\rho})^2 - 4a^2B_x^2/\rho}\right) \tag{2.19}$$

and similar definition for the other two.

Time Stepping: Gravitational Acceleration

The time step is also restricted to be less than the time it takes for the gravitational acceleration alone to move a parcel of fluid half of one zone.

$$\Delta t_{accel} = min(\frac{1}{2}\sqrt{\frac{\Delta x}{a_i}}) \tag{2.20}$$

where $i = x, y, z$ and the min is taken of the zones on a level.

Time Stepping: Cosmological Expansion

An additional restriction comes from the cosmological expansion, requiring the timestep to be less than the cosmological expansion timescale,

$$\Delta t_{expansion} = \eta\frac{a}{\dot{a}} \tag{2.21}$$

where η is typically 0.01.

Time Stepping: Particle Motion

The fourth timestep criterion is based on restricting particle displacement in a single timestep to be smaller than a single zone:

$$\Delta t_{particles} = min(\frac{a\Delta x}{v_{i,p}}) \tag{2.22}$$

where min is over velocity component i and particle p.

2.1.5 Boundary Conditions and Ghost Zones

Ghost Zones are filled in one of three means.

1. **Copying.** The dominant mechanism for filling ghost zones copying from active zones that occupy the same physical space. This also takes into account periodic boundary conditions. For EnzoMHD, face centered fields are copied from the faces of all cells, including those that border on active cells. This is somewhat redundant for reasons described in 2.1.3.

2. **External** Root grids that lie along the domain wall filled with the external boundary routine. If the external boundary condition is not periodic, the grids zones are filled by a predetermined algorithm; for instance, outflow boundary conditions set ghost zones to be equal to the outermost active zone, akin to a Neumann condition of zero slope. These involve outflow, reflecting, and a completely general 'inflow'. Note that this is called only on the root grid, and not on subgrids that happen to lie on the edge. This can cause spurious waves at reflecting or outflow boundaries with AMR. Also note for EnzoMHD, the only external boundary conditions that have been tested are periodic and outflow.

3. **Interpolation** The third mechanism is used on refined grids whose ghost zones do not occupy the active space of another grid; these grids have their ghost zones filled by interpolation from the parent grid. Since Enzo uses hierarchical time stepping, subgrid steps that begin in the middle of a parent grid step fill their ghost zones from a linear interpolation of the parent grid time steps at t^n and t^{n+1}.

2.1.6 Left Hand Side: Hyperbolic terms

With the exception of the $1/a$ term that appears in front of each $\nabla\cdot$ operator, the left hand side of equations 2.1-2.4 are the familiar Ideal MHD equations. A form of equations (2.1) - (2.4) more relevant for this treatment is the following:

$$\frac{\partial \boldsymbol{V}}{\partial t} + \frac{\partial \boldsymbol{F}}{\partial x} = 0 \tag{2.23}$$

where

$$\mathbf{V} = \begin{pmatrix} \rho \\ \rho v_x \\ \rho v_y \\ \rho v_z \\ B_y \\ B_z \\ E \end{pmatrix} \tag{2.24}$$

$$\mathbf{F} = \begin{pmatrix} \rho v_x \\ \rho v_x^2 + p + B^2/2 - B_x^2 \\ \rho v_x v_y - B_x B_y \\ \rho v_x v_z - B_x B_z \\ B_y v_x - B_x v_y = -E_z \\ B_z v_x - B_x v_z = E_y \\ (E + p + B^2/2) v_x - B_x (\mathbf{B} \cdot \mathbf{v}) \end{pmatrix} \tag{2.25}$$

$$p = (E - \frac{1}{2}\rho \mathbf{v}^2 + \frac{1}{2}\mathbf{B}^2(\gamma - 1)) \tag{2.26}$$

These form a hyperbolic system of equations, which have been studied extensively in the literature. To take advantage of the work already done on this type of system of equations for our cosmological algorithm, we first multiply the cell width dx by the expansion factor a. This allows us to use any non-cosmological solver for cosmological applications. Upon completion of the solver, dx is divided by a to restore dx to the original comoving value.

Equation 2.23 is solved by first re-writing it in conservation form, that is taking suitable integrals in time and space. The resulting update is, in one dimension,

$$\hat{V}_{i,j,k}^{n+1} = \hat{V}_{i,j,k}^{n} - \frac{\Delta t}{\Delta x}(\hat{F}_{x,i+\frac{1}{2},j,k}^{n+\frac{1}{2}} - \hat{F}_{x,i-\frac{1}{2},j,k}^{n+\frac{1}{2}}) \tag{2.27}$$

where $\hat{V}$ represents the spatial average of the conserved quantities, and $\hat{F}$ represents an space and time average of the flux, centered in time at $t = t + \Delta t/2$. $\hat{V}$ is the quantity we store in the cells, and $\hat{F}$ comes from the hyperbolic solver.

The solver we use to solve the hyperbolic equations is that of Li et al. (2008), which is comes in three parts: spatial reconstruction, time centering, and the solution of the Riemann problem. Spatial reconstruction is done using piecewise linear monotonized slopes on the primitive variables $(\rho, \mathbf{v}, p, \mathbf{B})$. Time centering of the interface states by $\Delta t/2$ is performed using either the MUSCL-Hancock (Li et al., 2008) or Piecewise Linear Method (Colella & Glaz, 1985) integration. The Riemann problem is then solved using either the HLLC Riemann solver of Li (2005), HLLD solver of Miyoshi & Kusano (2005), or the isothermal HLLD solver of Mignone (2007). These fluxes are computed for the conserved, cell centered variables $(\rho, \rho\mathbf{v}, E, \mathbf{B_c})$. These fluxes are then differenced to obtain the update values of the fluid quantities only. The fluxes for the magnetic field are stored for use in the Constrained Transport algorithm, discussed in section 2.1.7. This is done in one dimension on successive sweeps along the x, y, and z directions. To reduce operator splitting error, the order of the sweeps is permuted. For more details, see Li et al. (2008).

In isothermal mode, the same method is used, but the energy terms in V and F are removed, and only the isothermal HLLD can be used.

2.1.7 Constrained Transport and the Divergence of B

One of the biggest challenges for an MHD code is to maintain the divergence free constraint on the magnetic field ($\nabla \cdot \mathbf{B} = \mathbf{0}$). Brackbill & Barnes (1980) found that non-zero divergence can grow exponentially during the computation and cause the Lorentz force to be non-orthogonal to the magnetic field. There are three major ways to assure the divergence remains zero. The first is a divergence-cleaning (or Hodge Projection) approach by Brackbill & Barnes (1980), which solves an extra Poisson's equation to recover $\nabla \cdot \mathbf{B} = \mathbf{0}$ at each time step. But Balsara & Kim (2004) found that non-locality of the Poisson solver introduces substantial spurious small scale structures in the solution. Additionally, solving Poisson's equation on an AMR mesh is computationally expensive. The second method involves extending the MHD equations to include a divergence wave (Powell et al., 1999; Dedner et al., 2002) which then advects the divergence out of the domain. As most

of our solutions are done on periodic domains, this is also an undesirable solution. The third method, and the one we have employed in Enzo, is the constrained transport (CT) method of Evans & Hawley (1988). This method centers the magnetic field on the faces of the computational cells and the electric field on the edges. Once the electric field is computed (more on this later) it's curl is taken to update the magnetic field. This ensures $\nabla \cdot \mathbf{B} = 0$ for all time, provided it's true initially.

$$B^{n+1}_{f,x,i-\frac{1}{2},j,k} = B^{n}_{x,i-\frac{1}{2},j,k} - \Delta t(\frac{1}{\Delta y}(E_{z,i-\frac{1}{2},j+\frac{1}{2},k} - E_{z,i-\frac{1}{2},j-\frac{1}{2},k}) + \frac{1}{\Delta z}(E_{y,i-\frac{1}{2},j,k+\frac{1}{2}} - E_{y,i-\frac{1}{2},j,k-\frac{1}{2}})) \tag{2.28}$$

Plugging equation 2.54 into the divergence operator 2.16 to find $\nabla \cdot \mathbf{B}^{n+1}_f$, one finds all terms are eliminated except the initial divergence $\nabla \cdot \mathbf{B}^{n}_f$.

The CT algorithm of Evans & Hawley (1988) was extended to work with finite volume methods by Balsara & Spicer (1999). This method uses the fact that the MHD Flux has the electromotive force as two of its components (see the 5^{th} and 6^{th} components of eqn. 2.25), so using these components then incorporates all the higher order and shock capturing properties of the Godunov solver into the evolution of the electric field. These components, which are centered at the face the computational cell, are then averaged to obtain an electric field at the edges of the cell. This was the first CT method applied to Enzo, so unless otherwise noted, the simulations presented here were done with this method. The reader is encouraged to read Balsara & Spicer (1999) for the full details. Full details of this method can be found in section 3.3

Gardiner & Stone (2005) extended this idea to include higher order spatial averaging, which eliminates a number of numerical artifacts present in Balsara & Spicer (1999) and increases the accuracy of the method. This method uses the fluxes from the Riemann solver, plus additional information from the data in the cell to construct a linear interpolation from the cell face to the cell edge. The reader is encouraged to see that paper for the details.

After the curl is taken and the face centered field $\mathbf{B_f}$ is updated, it is then averaged to obtain $\mathbf{B_c}$, via equation 2.17.

2.1.8 Right Hand Side: Gravitational Acceleration

In cosmological simulations, Enzo tracks the proper peculiar gravitational potential.

$$\nabla^2\Phi = \frac{4\pi G}{a}(\rho_b + \rho_d - \rho_0) \tag{2.29}$$

where ρ_b and ρ_d are baryonic and dark matter comoving density respectively, and ρ_0 is the comoving background density. For non-cosmological simulations, the dark matter and background density are ignored.

The gravitational potential Φ is solved in Enzo using a combination of methods. First, the root grid potential (which covers the entire computational domain) is solved for using a fast Fourier transform. Then the subgrids (which hopefully do not cover the computational domain) are solved using a multigrid relaxation technique. This resulting potential Φ is then differenced to obtain the acceleration $\mathbf{g} = \nabla\Phi$. Specifically,

$$\mathbf{g}_i = \frac{1}{2}(\Phi_{i+1} - \Phi_{i-1}) \tag{2.30}$$

As mentioned before, the fluxes are computed at the half time point $t + 1/2\Delta t$. In order to keep the velocity and consistent with this time centering, they are first advanced by a half time step:

$$\mathbf{v} = \mathbf{v} + \frac{\Delta t}{2}\mathbf{g} \tag{2.31}$$

After the fluxes are differenced to obtain the new state v_x^{n+1}, these states are then updated with the accelerations. For the velocity update, a density field centered in time is used. We follow the same formulation used by Colella & Woodward (1984)

$${v_x}^{n+1} = {v_x}'^{n+1} + \Delta t \frac{\frac{1}{2}(\rho^{n+1} + \rho^n)A_x}{\rho^{n+1}} \tag{2.32}$$

$$E^{n+1} = E'^{n+1} - \frac{1}{2}\rho^{n+1}({v_x}'^{n+1})^2 + \frac{1}{2}\rho^{n+1}({v_x}^{n+1})^2 \tag{2.33}$$

2.1.9 Right Hand Side: Expansion Source Terms

The cosmological expansion source terms are treated in much the same way as the gravitational source terms. First, a half time step is added to the values

before the flux is computed.

$$\mathbf{v}'^{n} = \mathbf{v}^{n} - \frac{1}{2}\Delta t \frac{\dot{a}}{a}\rho^{n} \tag{2.34}$$

$$p'^{n} = p^{n} - \frac{1}{2}\Delta t \frac{\dot{a}}{a} 3(\gamma - 1)p^{n} \tag{2.35}$$

$$\mathbf{B}_{c}'^{n} = \mathbf{B}_{c}^{n} - \frac{1}{2}\Delta t \frac{\dot{a}}{2a}\mathbf{B}_{c}^{n} \tag{2.36}$$

The quantities $\mathbf{v}'^{n}$, p'^{n} and $\mathbf{B}'^{n}$ are then used in the rest of the solver described in section 2.1.6. After the fluxes are differenced, the source terms are then added to the fluid quantities in full. This is done in a semi-implicit manner, by averaging the quantities to be updated in time. For instance, the expansion contribution to the magnetic field is

$$\frac{\partial \mathbf{B}}{\partial t} = -\frac{\dot{a}}{2a}\mathbf{B} \tag{2.37}$$

which is discretized

$$\mathbf{B}_{exp}^{n+1} - \mathbf{B}^{n+1} = -\frac{\dot{a}}{2a}\left(\frac{\mathbf{B}_{exp}^{n+1} + \mathbf{B}^{n+1})}{2}\right) \tag{2.38}$$

and solving for $\mathbf{B}_{exp}^{n+1}$ we have

$$x = \frac{\dot{a}}{4a} \tag{2.39}$$

$$\mathbf{B}_{exp}^{n+1} = \frac{(1-x)}{(1+x)}\mathbf{B}^{n+1} \tag{2.40}$$

Pressure and velocity are updated in a similar manner. See appendix 2.5 for the full update.

2.1.10 Dual Energy Formalism

Hypersonic flows are quite common in cosmological simulations. Due to the extremely large gravitational forces, the ratio of kinetic energy $E_{kinetic}$ to gas internal energy $E_{internal}$ can be as high as 10^8. This leads to problems when computing the internal energy in this type of flow, as the universe does math with infinite accuracy, but computers do not. Higher order Godunov code typically

track only the total energy (equation 2.5). Thus finding the internal energy from the total energy tracked by the software,

$$E_{internal} = E_{total} - E_{kinetic} - E_{magnetic}$$

involves the small difference of two (or three) large numbers, which causes problems when the small number ($E_{internal}$) is near the roundoff noise of the original numbers (E_{total} and $E_{kinetic} + E_{magnetic}$).

To overcome this, we have implemented two algorithms that solve an additional equation to track the small numbers; the modified entropy equation given in Ryu et al. (1993) and the internal energy equation given in Bryan et al. (1995). These two equations are:

$$\frac{\partial S}{\partial t} + \frac{1}{a}\nabla \cdot (S\mathbf{v}) = -\frac{3(\gamma-1)\dot{a}}{a}S \tag{2.41}$$

$$\frac{\partial \rho e}{\partial t} + \frac{1}{a}\nabla \cdot (\rho e\mathbf{v}) = -\frac{3(\gamma-1)\dot{a}}{a}\rho e + \frac{p}{a}\nabla \cdot \mathbf{v} \tag{2.42}$$

where $S \equiv p/\rho^{\gamma-1}$ is the comoving modified entropy and e is the internal energy. The modified entropy equation is valid only outside the shocks where the entropy is conserved. Use of either (not both) of these equations is at the discretion of the simulator.

Through the course of the simulation, the ratio of internal energy to total energy is monitored. When this ratio is less than some preset value η, one of the modified equations is used. As in Li et al. (2008), we use $\eta = 0.008$. They note that reducing this parameter will cause a decrease in the volume filled by low temperature gas, as most of the gas affected by the switch is cold, high velocity gas. The optimal choice for this parameter is still an open question for the general situation. Li et al. (2008) compared this two approaches and found almost identical results.

2.1.11 Adaptive Mesh Refinement

Structured AMR, initially devised by Berger & Colella (1989), is a technique for increasing resolution of a simulation in parts of a simulation that require higher resolution for increased accuracy or suppression of numerical artifacts, while

conserving memory and CPU cycles in areas that don't. Refinement criteria will not be described here, as they vary from simulation to simulation. AMR has four basic necessary parts:

1. **Patch Solver** This is the algorithm that actually solves the finite volume PDEs in question, as described by sections 2.1.6 - 2.1.10. The approximations used for the patch solver are conservative in a finite volume sense, and the rest of the choices are made to preserve that conservation.

2. **Refinement Operator** This is the routine that creates fine resolution elements from coarse ones. In Enzo, we use conservative, volume weighted interpolation for the fluid quantities $\rho, E, \vec{v}$. For the magnetic fields, we use the method described by Balsara (2001), with some slight modifications in implementation. This method constructs a quadratic divergence free polynomial, and area-weighted averages are used for the fine grid quantities. This is described in more detail in appendix 2.4.

3. **Projection Operator** This is the routine that projects the fine grid data back to the parent coarse grid. For Enzo, the parent grid is simply replaced by a volume-weighted average of the fine cells. For the face centered magnetic field, this is an area weighted average, though in practice we don't explicitly average the magnetic field, as discussed in below and in appendix 2.4.1

4. **Correction Operator** Once the projection operator replaces the solution on the coarse grids, the evolution on the coarse grids is no longer consistent with the underlying equations in the manner they were discretized. That is to say, the total change of any conserved quantity inside the region is no longer equal to the flux across its surface. For the Enzo hydro fields, this is corrected with the flux correction mechanism. More details on this and the modifications in EnzoMHD see appendix 2.3

EnzoMHD does all of these steps for the fluid quantities, but for the magnetic field it slightly alters this procedure. In order to overcome a shortcoming in the original data structures used in Enzo, we combined the projection and correction operations for the magnetic fields in one step. The net effect of the correction

operator is to ensure that all zones are updated by finest resolution fluxes available, even if they were updated by coarse data initially. For the magnetic field update, we don't project the actual magnetic field that is of interest, but rather the electric field (effectively the 'flux' for B_f), then take the curl of the newly projected electric field. Thus the coarse magnetic data co-located with the fine grids get updated with the fine data, and the bounding zones don't need correction at all.

More detail on this process can be found in appendices 2.4 and 2.3

2.2 Numerical Experiments

EnzoMHD has many configurations available. Here, we test some of the possible configurations, to indicate the quality of solution possible with EnzoMHD.

2.2.1 MHD Tests without AMR

We first test our code in unigrid (fixed resolution) mode, in order to ensure consistency of the patch solver with the algorithm described in Li et al. (2008). We do two one dimensional cosmology tests (Caustics and Zel'dovich Pancake), two one dimensional non-cosmological tests (Brio and Wu and the Kim Isothermal), one 2d non-cosmological test (Orszag Tang) and one 3d cosmological test, and one 3d turbulence test.

Brio and Wu shock tube

The shock tube defined by Brio & Wu (1988) is a standard test of any MHD solver, as it displays a number of the important MHD waves, including a compound wave. Compound waves are not a property of pure hydrodynamics, because the system is convex. However, due do the more complex nature of the MHD equations, certain initial conditions can cause flows in which at one point the shock speed in a given family is higher than the wave speed for that family, causing a shock, but lower in the post shock region, causing a rarefaction immediately following the shock.

This can be seen in figure 2.4. The problem was run with 800 zones to a time $t = 0.2$, using the HLLD solver in Enzo. This shock tube shows, from left to right, a fast rarefaction, slow compound (shock+rarefaction), contact, slow shock, and fast rarefaction. It can be seen that this solver captures this shock tube problem quite well.

Isothermal Tests

One of the primary application areas of EnzoMHD will be in simulating turbulence and star formation in cold molecular clouds. Due to the fast cooling time of these environments, an isothermal equation of state is a good approximation a large portion of these processes. In simulations done by Kritsuk et al. (2007) using Enzo and other works by the same authors an isothermal equation of state is approximated by using an adiabatic solver and setting $\gamma = 1.001$.

To test if this approximation is appropriate for this code, we ran the isothermal shock tube of Kim et al. (1999). One can see from figure 2.5 that this approach works well, as shock jumps and positions are all correct, and features are reasonably sharp. This test was run with 256 zones to a time of 0.1.

However, in turbulent simulations with gravitational collapse, the measured value of the sound speed, $\sqrt{p/\rho}$, is initially uniform, but after a few hundred timesteps can vary by as much as 1000, which is far from isothermal. It is believed that the difference between this code and what has been done in the past with Enzo stems from the Riemann solver. The HLL family of Riemann solvers assumes a particular wave structure in computing the interface flux. This wave structure, for HLLC and HLLD, contains a contact discontinuity which is not present in the isothermal Riemann fan, and does not reduce appropriately in the $\gamma \rightarrow 1$ limit. To combat this, we installed the Isothermal variant of HLLD by Mignone (2007). The results of this code on the Kim test are nearly identical to that in figure 2.5 and not reproduced here. The problem seen are, of course, eliminated as the sound speed is set as an input parameter.

One-dimension MHD Caustics

This test is taken from Li et al. (2008), which initially derived from a pure hydro version from Ryu et al. (1993). This problem is used to test the ability of the code to capture shocks and to deal with hypersonic flows. Initially, $v_x = -\frac{\pi}{2} sin(2\pi x)$, $\rho = 1$ and $p = 10^{-10}$. Caustics are formed because of the compression by the velocity field. The Mach number of the initial peak velocity is 1.2×10^4. The pressure can easily become negative for such high Mach number flow.

We performed the test with same magnetic field settings as in Li et al. (2008). The magnetic field in the x and z directions are always zero while $B_y = 0, 0.001, 0.02$ and 0.05. The calculation was done with 1024 cells and the results at $t = 3$ are shown in figure 2.6. Our results match the results from CosmoMHD (Li et al., 2008) quite well, as expected.

The Zel'Dovich Pancake

The Zel'Dovich pancake is a popular test problem for codes that include gravity in comoving coordinates. The problem setups are taken from Li et al. (2008). This takes place in a purely baryonic universe with $\Omega = 1$ and $h = \frac{1}{2}$. The initial scale factor $a_i = 1$ corresponds to $z_i = 20$. The initial velocity field is sinusoidal with the peak value $0.65/(1 + z_i)$, and $v = 0$ at the center of the box. The initial comoving box size is $64h^{-1}Mpc$. The shocks forms at $z = 1$. The initial baryonic density and pressure are uniform with $\rho = 1$ and $p = 6.2 \times 10^{-8}$. The tests were run with 1024 cells, both with and without magnetic fields. Our results are almost identical to the results from CosmoMHD (Li et al., 2008), as expected. Results can be seen in figure 2.7.

Orszag-Tang

The Orszag-Tang Vortex was originally developed by Orszag & Tang (1979) to demonstrate that small scale structure can be generated by the nonlinearities in the MHD equations. It initially starts with a single large scale rotating velocity structure and two circular magnetic structures. From these simple large scale

initial conditions, substantial small scale structure is formed. It now serves as a standard test problem to demonstrate the accuracy and diffusivity of MHD codes.

The initial conditions are on a 2 dimensional periodic box, 256 zones on a side. $\mathbf{v} = v_0(-sin(2\pi y)\hat{x} + sin(2\pi x)\hat{y}, \mathbf{B} = B_0(-sin(2\pi y)\hat{x} + sin(4\pi x)\hat{y}), v_0 = 1, B_0 = 1/\sqrt{4\pi}, \rho_0 = 25/(36\pi), p_0 = 5/(12\pi)$, and $\gamma = 5/3$ which gives a peak Mach number of 1 and peak $\beta = p_0/(B_0^2/2) = 10/3$. Figure 2.8 shows the density at $t = 0.48$, from which one can see that the solution agrees with other solutions to the problem in the literature.

3D Adiabatic Universe with MHD

We have also performed the 3D adiabatic CDM Universe test described by Li et al. (2008) both with and without magnetic fields. We also compared the non-magnetized results with the results run using the PPM solver (Colella & Woodward, 1984). Adiabatic evolution of a purely baryonic Universe was computed with an initial CDM power spectrum with the following parameters: $\Omega = \Omega_b = 1$, $h = 0.5$, $n = 1$ and $\sigma_8 = 1$ in a computational volume with side length $L = 64h^{-1}Mpc$. The transfer function from Bardeen et al. (1986) was used to calculate the power spectrum of the initial density fluctuations. Evolution was done from $z = 30$ to $z = 0$. We used 256^3 cells for each simulation. The comparisons are made at the final epoch, $z = 0$. Though this test is identical to that of Li et al. (2008), our results can't compared with theirs directly since different random seeds were used for the realization of the initial density and velocity.

Figure 2.9 shows a comparison of the mass-weighted temperature distribution, figure 2.10 is a comparison of the volume-weighted density distribution. The discrepancies between PPM and MHD solvers are small, indicating the two codes perform roughly the same. The nature of the differences is expected, since PPM solver has third order accuracy while the MHD solver has second order accuracy and larger numerical diffusion. This allows PPM to capture shocks in fewer zones, which causes the dense shocked gas to not only have a smaller volume fraction, but also be hotter and slightly less dense than in the MHD solver.

We have also done a similar run with the same initial conditions to the

above, but with an initial magnetic field, $B_x = B_z = 0,\ B_y = 2.5 \times 10^{-9}$ Gauss, which is 4.32×10^{-7} in code units. Figure 2.11 shows the scaled divergence of the magnetic fields, averaged over the entire box, as a function of redshift. The scaled divergence is $< |h\nabla \cdot \mathbf{B}/|\mathbf{B}|| >$, where $h = 1/256$ is the spatial scale, and $|B|$ is the local maximum magnetic field strength, is the most relevant measure of the potential numerical effects of divergence. The divergence of the magnetic fields is close to the round-off error.

Comparison of Turbulent Evolution

Turbulence is one of the primary physical environments of astrophysical fluids. Thus is is extremely important to understand how a code performs in a turbulent environment.

The Santa Barbara Turbulence Comparison project, which began in November 2007, is an attempt to quantify the performance of several difference codes on the same Hydrodynamic and Magnetohydrodynamic Turbulent flow. Initial conditions were prepared by Åake Nordlund, and distributed to a number of simulators, who then ran the simulation with their respective codes. The initial conditions were initially uniform density and magnetic field with plasma $\beta = 22$. The field was stired with Gaussian velocity distribution until a steady state mach number of 8.9 was reached. This initial state was then run without driving on 6 different MHD codes; Flash (Fryxell et al., 2000), Ramses (Fromang et al., 2006), PPML (Ustyugov & Popov, 2008) and 3.6, EnzoMHD, Zeus (Stone & Norman, 1992), and Phantom-SPH (Rosswog & Price, 2007).

This comparison was fairly elaborate, and only two of the results are reported here. Figures 2.12 and 2.13 show the power spectrum after $t = 0.2$, roughly twice the time it takes an average shock to cross the box for the velocity and magnetic field, respectively. The primary point we wish to draw here is the relative strength of the small scale structure to the right of each set of curves. It is generally seen in both theory and practice that in turbulent flow, the transfer of power from large scale to small is a conservative process until the smallest scale is reached. This dissipative scale is driven my microphysics in real fluids, but by

the details of the numerical solver in numerical ("Made Up") physics. So one can easily gague the relative dissipation in the method by the power seein in the small scale end of the power spectrum.

The part of the graph that's relevant for this discussion in each of figure 2.12 and 2.13 is the pink curve, labled Enzo. This was done with EnzoMHD with the Isothermal HLLD solver. In both figures, one first notes that the inertial range scaling, the part of the graph that is not the large scale driving and not the small scale dissipation, from roughly $k/k_{min} = 1$ to $k/k_{min} = 1.5$, the slopes of most of the curves are comparable. This demonstrates that each code responds relatively similarly to eachother. The notable exception is the yellow curve, Phantom-SPH. This is an SPH code, and has much less development time under its belt, and is obviously doing the worst. The more interesting features come in the small strcture at high k/k_{min}. In figure 2.12, one sees that the velocity dissipation is comperatble to both Ramses and PPML, indicating that the dissipation is as low as relaistically obtainable. However, in figure 2.13, EnzoMHD has clearly the lowest power of the grid based codes, indicating that it has the weakest dissipation properties. It is currently believed that this is due to the CT method used. While Athena CT is quite good, the other methods use more sophisticated mechanisms that use either higher order time evolution, as in Flash, or characteristic tracing or some other reconstruction that more closely tracks the fluid dynamics, as in Ramses, PPML, and Zeus.

Two other similar comparisons have been done in this work. They can be found in sections 3.5, which shows DaveThena, this method, PPM, and PPML; and 3.1.2 which only shows the Ryu and Jones method.

2.2.2 MHD Tests with AMR

To test the Adaptive Mesh Refinement, we ran a sample of the tests from the previous section with AMR, to ensure no spurious artifacts are introduced by the AMR. These are the Adiabatic Expansion test in section 2.2.2 and the one dimensional caustic and pancake tests (sections 2.2.2 and 2.2.2).

Three-dimension MHD Adiabatic Expansion

This test is taken from Bryan et al. (1995). This test uses a completely homogenous universe with initial $T_i = 200K$ and $v_i = 100km/s$ in the x-direction at an initial redshift of $z_i = 20$. In the code units, the initial density is 1.0 and initial velocity is 2.78×10^{-3} and the initial pressure is 1.24×10^{-9}. Additionally we have a uniform magnetic field $B_x = B_y = B_z = 1 \times 10^{-4}$ in code units, which is $2.66 \times 10^{-7}G$ in cgs.

The simulation used a 16^3 root grids with 2 levels of refinement in the center region and ran to $z = 0$.

The expansion terms in eqns (2.1) - (2.4) operate like drag terms, so that in the absence of a source, the velocity decreases as $v = v_i a^{-1}$, the temperature as $T = T_i a^{-2}$ and the magnetic field should decrease as $a^{-1/2}$.

The temperature at $z = 0$ is $0.453406K$, 0.024% below the analytic result of $0.453515K$. The velocity at $z = 0$ is $4.76176km/s$, compared to the analytic result $4.7619km/s$, a 0.0029% discrepancy. The final magnetic field strength is $6.03 \times 10^{-10}G$ (2.18×10^{-5} in the code units), a difference of 0.0006% with respect to the analytic solution. Figure 2.14 shows the B_y as a function of redshift, the solid line shows the theoretical value.

One-dimensional MHD Caustics with AMR

We also ran the the 1d MHD Caustic test with AMR, using 256 root grid zones with 2 levels of refinement, again by a factor of 2, giving an effective resolution is 1024 cells. Figure 2.15 shows comparisons of density and gas pressure of non-AMR and AMR runs with different initial magnetic field strengths, as described before. Figure 2.16 shows the comparisons of B_y for runs with different initial values of B_y. In both plots, the AMR result is sampled to the finest resolution. The AMR runs give almost identical results to the unigrid runs, while the CPU time and memory were greatly saved in the AMR runs.

Zel'Dovich Pancake with AMR

We also ran the pancake problem with AMR. The problem was set up with the same initial conditions as the unigrid run, but with a root grid of 256 root cells and 2 levels of refinement by 2. We compared these results having effectively 1024 cells to the results of our previous high resolution which actually had 1024 cells. Figure 2.17 shows comparisons of density and gas pressure between the non-AMR and AMR runs, with different initial values for B_y. Figure 2.18 shows the comparisons of B_y with different initial values. Again, the AMR computation got very similar results, while saving CPU and memory resources.

2.3 Flux Correction

At any given time in an AMR simulation, there are points in space that are described by more than one data structure. In a finite volume hydro calculation, with cell centered data fields, this occurs at the boundary between coarse and fine grids in the Flux fields, $\vec{F}$. In an AMR MHD calculation, with face centered magnetic fields, this occurs at the same boundary, in the face centered magnetic field, and the edge centered electric field. Ensuring consistency between data is vital for the conservation of quantities like mass, energy, momentum, and $\nabla \cdot \mathbf{B}$. Flux Correction is essential for this consistency.

2.3.1 Conservation Form

It is useful to briefly describe the basic formulation of the methods used in Enzo and EnzoMHD before moving on to the flux correction mechanism.

Any conservative system, such as ideal MHD, can be written in a differential form as

$$\frac{\partial V}{\partial t} + \nabla \cdot F = 0 \tag{2.43}$$

where V and F are suitably defined, in our case by 2.24 and 2.25. Here we ignore any source terms.

In finite volume methods, we store average quantities of V and F, and rewrite the conservation law in Conservation Form, using the Fundamental Theorem and Stokes Theorem. Starting with eqn 2.43, and integrating, we get:

$$\int_t^{t+\Delta t}\int_V \frac{\partial V}{\partial t} dV dt = -\int_t^{t+\Delta t}\int_A F \cdot dA dt \tag{2.44}$$

where the volume V is taken from the point (x, y, z) to $(x + \Delta x, y + \Delta y, z + \Delta z)$. Now let

$$\hat{V}^n = \frac{1}{\Delta V}\int_V V(x, y, z, t^n) dV \tag{2.45}$$

$$\tilde{F}_{x,I+\frac{1}{2},J,K} = \frac{1}{\Delta y \Delta x}\int_{\Delta y,\Delta z} F(x = I + \frac{1}{2}, y, z) \cdot \hat{x} dy dz \tag{2.46}$$

where $\hat{x}$ is the unit vector in the x direction. Similar definitions apply $\tilde{F}_y$ and $\tilde{F}_z$, and

$$\hat{F}_x = \frac{1}{\Delta t}\int_{\Delta t} \tilde{F}_x dt \tag{2.47}$$

The averaging here was taken explicitly in two steps to emphasize that Δx,Δy and Δz are possibly functions of t, as the are in cosmological hydrodynamics. Putting this all together, we get the equations in their final analytical form before discretization (also the last form we'll be using here)

$$\begin{aligned}\hat{V}^{n+1}_{I,J,K} = \hat{V}^n_{I,J,K} - \Delta t(&\frac{1}{\Delta x}(\hat{F}_{x,I+\frac{1}{2},J,K} - \hat{F}_{x,I-\frac{1}{2},J,K}) + \\ &\frac{1}{\Delta y}(\hat{F}_{y,I,J+\frac{1}{2},K} - \hat{F}_{y,I,J-\frac{1}{2},K}) + \\ &\frac{1}{\Delta z}(\hat{F}_{z,I,J,K+\frac{1}{2}} - \hat{F}_{z,I,J,K-\frac{1}{2}}))\end{aligned} \tag{2.48}$$

Note that equation 2.48 is an exact equation, since only averages and the fundamental theorem of calculus have been used up to this point. The trick in finite volume methods such as our MHD is finding appropriate approximations to $\hat{F}$ that are both accurate and stable.

2.3.2 Conservation Form and AMR: Enter Flux Correction.

As mentioned at the beginning of the section, an AMR simulation has multiple data structures representing a single point in space. In entirely cell centered

codes such as PPM, the only such instance is at the surface of a fine grid boundary, where both the fine grid and coarse grid represent the flux at that point. Moreover, after the fine grid field is projected into the coarse, there's a mismatch on the coarse grid itself as to the value of the flux at the surface. The value of that discrepancy can be easily found. After the projection, a coarse grid at a point (I, J) has the value (restricting to 2d, for clarity)

$$\hat{V}_{I,J}^{n+1} = \sum_{\substack{i=I\pm\frac{1}{4} \\ j=J\pm\frac{1}{4}}} \hat{q}_{i,j}^{n+1} \tag{2.49}$$

where lower case quantities denote the value of the fine grid data. Expanding the time update for $\hat{q}^{n+1}$ in space and time, we find that

$$\hat{V}_{I,J}^{n+1} = \sum_{\substack{i=I\pm\frac{1}{4} \\ j=J\pm\frac{1}{4}}} \hat{q}_{i,j}^{n} - (\sum_{m=n}^{n+1} \sum_{x,j=J\pm\frac{1}{4}} \frac{\Delta t^m}{\Delta V^m} \hat{f}_{I+\frac{1}{2},j}^{m} + \; - \sum_{m=n}^{n+1} \sum_{x,j=J\pm\frac{1}{4}} \frac{\Delta t^m}{\Delta V^m} \hat{f}_{I-\frac{1}{2},j}^{m}) \tag{2.50}$$

$$-(y \; and \; z \; terms)$$

By construction of the interpolation polynomial (and projection at the last timesteps) the first term is just equal to $\hat{V}_{I,J}^{n}$, which means that, by equation 2.48 $\hat{V}_{I,J}$ effectively sees, at the point $I + \frac{1}{2}$,

$$\frac{\Delta t}{\Delta V} \hat{F}_x = \sum_{m=n}^{n+1} \sum_{x,j=J\pm\frac{1}{4}} \frac{\Delta t^m}{\Delta V^m} \hat{f}_{I+\frac{1}{2},j}^{m} :=< f_x > \tag{2.51}$$

However, for the cell $(I - 1, J)$, which has no corresponding fine grid flux, $\hat{F}_{I+\frac{1}{2}}$ come from the discretization method on the coarse grid. There is absolutely no reason for the two to match, so we have a discrepancy in the descriptions of the data. This can be solved by simply replacing the less refined data that $\hat{V}_{I+1,J}$ used with the more refined average, given by equation 2.51:

$$\hat{V}_{I+1,J,_{fc}} = \hat{V}_{I+1,J} + \frac{\Delta t}{\Delta V} \hat{F}_{x,I+\frac{1}{2},J} - \sum_m \sum_j \frac{\Delta t^m}{\Delta V^m} \hat{f}_{x,I+\frac{1}{2},j}^{m} \tag{2.52}$$

Now every place $\hat{F}_{x,I,J}$ show up in our method, the exact same approximation is used.

2.3.3 Flux Correction and MHD

A similar formalism to that described in 2.3.1 is used for to advance the magnetic fields in EnzoMHD, but instead of using volume averages, we use area averages. The magnetic evolution is given by the induction equation:

$$\frac{\partial \vec{B}}{\partial t} = -\nabla \times \vec{E} \tag{2.53}$$

When discretized, equation 2.53 yields the equation

$$\hat{B}^{n+1}_{x,I+\frac{1}{2},J} = \hat{B}^{n}_{x,I+\frac{1}{2},J} - \frac{\Delta t}{\Delta y \Delta z}(\Delta z(\hat{E}_{z,I+\frac{1}{2},J+\frac{1}{2},K} - \hat{E}_{z,I+\frac{1}{2},J-\frac{1}{2},K}) + \Delta y(\hat{E}_{y,I+\frac{1}{2},J,K+\frac{1}{2}} - \hat{E}_{y,I+\frac{1}{2},J,K-\frac{1}{2}})) \tag{2.54}$$

where

$$\hat{B}^{n}_{x,I+\frac{1}{2},J,K} = \frac{1}{\Delta y \Delta z}\int_A \vec{B}(x = I + \frac{1}{2}, y, z, t^n) \cdot \hat{x} dy dz \tag{2.55}$$

$$\hat{E}^{n} = \frac{1}{\Delta t}\int_t^{t+\Delta t} \frac{1}{\Delta x}\int_x \vec{E} \cdot dl dt \tag{2.56}$$

which is also exact, and the main problem is finding a suitable approximation for $\hat{E}$.

Again, after the area-weighted projection of the fine grid field $\hat{b}_x$ into the coarse grid $\hat{B}_x$, there's a discrepancy between the electric field at a refined point on the surface of a refined grid, as it's seen by both grids that have subgrids and grids that don't. In Balsara (2001), he suggests a similar flux correction mechanism to that of the standard hydro, described in 2.3.2. However, due to an issue with the initial implementation of flux correction in Enzo (which has since been fixed) and ease of computational logic, we chose a different route. In EnzoMHD, instead of projecting fine grid magnetic fields into coarse magnetic fields and then correcting zones in the coarse grid, we project the electric field and then take the curl of the entire coarse grid. Thus, all coarse grid magnetic fields see the most accurate data at the same time, and no a-posteriori correction needs to be done. Where there are no subgrids, the coarse grid sees an electric field that comes from the CT module

in section 2.1.7, and where there are subgrids it sees

$$\hat{E}^{n}_{z,i-\frac{1}{2},j-\frac{1}{2},k} = \frac{\Delta t^{n}}{\Delta t}(e^{n+\frac{1}{2}}_{z,i-\frac{1}{2},j-\frac{1}{2},k-\frac{1}{4}} + e^{n+\frac{1}{2}}_{z,i-\frac{1}{2},j-\frac{1}{2},k+\frac{1}{4}}) + \frac{\Delta t^{n+\frac{1}{2}}}{\Delta t}(e^{n+\frac{3}{4}}_{z,i-\frac{1}{2},j-\frac{1}{2},k-\frac{1}{4}} + e^{n+\frac{3}{4}}_{z,i-\frac{1}{2},j-\frac{1}{2},k+\frac{1}{4}}) \quad (2.57)$$

While a complete flux correction treatment would potentially save on memory and flops, in practice the extra memory is negligible compared to the total memory and time used by the rest of Enzo, and the extra floating point operations done here are offset by increase cache utilization of the data, as the entire grid is done in a single stride one sweep instead of an essentially random access pattern.

As described in section 2.1.5, some of the subgrids get their boundary conditions updated from the parent zones. Because of this, the curl of the magnetic field is actually taken twice. The first time is done immediately after the hyperbolic update, in order to ensure that the parent zones are up to date for the interpolation of the ghost zones of the subgrids that need it. The second time is after the subgrids project their electric field to the parent, to ensure maximal accuracy of the parent grids. This additional call takes negligible time, as the curl has relatively few operations. See appendix 2.5 for the details of this order of operations.

2.4 AMR MHD Reconstruction

2.4.1 MHD Reconstruction

For completeness, we will briefly outline the AMR reconstruction used in EnzoMHD. The reader is encouraged to see the details in the original paper by Balsara (2001).

In this appendix, we have dropped the subscript f from the face centered fields, as the face centered field is the only one in question.

Balsara's reconstruction method for the magnetic field is a 3 dimensional, quadratic reconstruction of all 3 vector fields simultaneously. If we let $\mathbf{b}$ be the polynomial fit to the discrete face centered field field B, the general reconstruction is

$$b_x(x,y,z) = a_0 + a_x x + a_y y + a_z z + a_{xx}x^2 + a_{xy}xy + a_{xz}xz \tag{2.58}$$

$$b_y(x,y,z) = b_0 + b_x x + b_y y + b_z z + b_{xy}xy + b_{yy}y^2 + b_{yz}yz \tag{2.59}$$

$$b_z(x,y,z) = c_0 + c_x x + c_y y + c_z z + c_{xz}xz + c_{yz}yz + c_{zz}z^2 \tag{2.60}$$

The coefficients are found by the following constraints:

1. The analytic reconstruction should be divergence free.

2. At the faces of the parent cell, the reconstruction should reduce to a bilinear reconstruction, where the slopes are monotonized with the minmod slope limiter. For instance,

$$b_x(x = \frac{\Delta x}{2}, y) = B_{x,i+\frac{1}{2},j,k} + \frac{\Delta_y B_{x,i+\frac{1}{2}}}{\Delta y}y + \frac{\Delta_z B_{x,i+\frac{1}{2}}}{\Delta z}z \tag{2.61}$$

where

$$\Delta_y B_{x,i+\frac{1}{2}} = minmod(B_{x,i+\frac{1}{2},j+1} - B_{x,i+\frac{1}{2},j}, B_{x,i+\frac{1}{2},j} - B_{x,i+\frac{1}{2},j-1}) \tag{2.62}$$

$$minmod(x,y) = \begin{cases} x, & |x| < |y| \text{ and } xy > 0 \\ y, & |y| < |x| \text{ and } xy > 0 \\ 0, & xy < 0 \end{cases} \tag{2.63}$$

The *minmod* slope is used in order to minimize oscillations. Area weighted averages over these polynomials are then used to assign the fine grid values.

Often, a fine grid patch will encroach on unrefined territory. This results in the refinement of coarse zones that a.) share a face with fine grids but b.) don't have corresponding fine grids of their own. Balsara refers to this as "Prolongation" of the fine grid. To avoid generating any divergence at the boundary of the face, the interpolation polynomials need to match the old fine data. The interpolation equations above (eqns 2.58 - 2.60) do not have enough degrees of freedom to accommodate that many data points. In this case, Balsara describes a new polynomial that DOES have enough degrees of freedom, by adding 3^{rd} order cross terms to equations 2.58 - 2.60:

$$\begin{aligned} b_x(x,y,z) =& a_0 + a_x x + a_y y + a_z z + a_{xx}x^2 + a_{xy}xy + a_{xz}xz \\ &+ a_{yz}yz + a_{xyz}xyz + a_{xxz}x^2 z + a_{xxy}x^2 y \end{aligned} \tag{2.64}$$

$$\begin{aligned} b_y(x,y,z) =& b_0 + b_x x + b_y y + b_z z + b_{xy}xy + b_{yy}y^2 + b_{yz}yz \\ &+ b_{xz}xz + b_{yyz}y^2 z + b_{xyz}xyz + b_{xyy}xy^2 \end{aligned} \tag{2.65}$$

$$\begin{aligned} b_z(x,y,z) =& c_0 + c_x x + c_y y + c_z z + c_{xz}xz + c_{yz}yz + c_{zz}z^2 \\ &+ c_{xy}xy + c_{yzz}yz^2 + + c_{xzz}xz^2 + c_{xyz}xyz \end{aligned} \tag{2.66}$$

The yet undetermined coefficients are found by matching the polynomial to a bilinear fit on the face:

$$b(x = \frac{\Delta x}{2}, y, z) = B_{x,i+\frac{1}{2},j,k} + \frac{\Delta_y B_{x,i+\frac{1}{2}}}{\Delta y} y + \frac{\Delta_z B_{x,i+\frac{1}{2}}}{\Delta z} z + \frac{\Delta_{yz} B_{x,i+\frac{1}{2}}}{\Delta y \Delta z} yzp \tag{2.67}$$

and now the finite differences are taken from the finest grid:

$$\begin{aligned} \Delta_{yz} B_{x,i+\frac{1}{2}} = 4((&B_{x,i+\frac{1}{2},j+\frac{1}{2},k+\frac{1}{2}} - B_{x,i+\frac{1}{2},j-\frac{1}{2},k+\frac{1}{2}}) - \\ &(B_{x,i+\frac{1}{2},j+\frac{1}{2},k-\frac{1}{2}} - B_{x,i+\frac{1}{2},j-\frac{1}{2},k-\frac{1}{2}})) \end{aligned} \tag{2.68}$$

$$\begin{aligned} \Delta_{y} B_{x,i+\frac{1}{2}} = ((&B_{x,i+\frac{1}{2},j+\frac{1}{2},k+\frac{1}{2}} - B_{x,i+\frac{1}{2},j-\frac{1}{2},k+\frac{1}{2}}) + \\ &(B_{x,i+\frac{1}{2},j+\frac{1}{2},k-\frac{1}{2}} - B_{x,i+\frac{1}{2},j-\frac{1}{2},k-\frac{1}{2}})) \end{aligned} \tag{2.69}$$

where B is the field on the fine grid. Note that since this is now a centered difference, the minmod slope limiter is not used.

2.4.2 Implementation in Enzo

In order to avoid complicated book keeping routines to determine which cells are being prolonged into, and from which direction, we formulate only one interpolation polynomial, given by equations 2.64-2.66. The necessary finite differences for a given refinement region are taken from the finest data available, as

in equations 2.68 and 2.69. The last four terms in each reconstruction polynomial are there exclusively to ensure consistency of Old Fine Grid Data, so for faces that have no Fine Data before the reconstruction, these are set to zero. Since the reconstruction polynomial exactly matches the old fine grid data, this also eliminates the need to copy the old fine grid data to the newly refined patch.

2.5 Schematic for the Cosmological MHD Code

In this section, we present a schematic of the MHD code, for clarity and easy reference.

Step 0.– We start with conserved quantities density, total energy, and momentum $(\rho^n_{BM}, E^n_{total}, \mathbf{p}^n_{DM})$, and primitive quantities velocity and gas pressure $(v^n_{BM},\ P^n_{gas})$ for the baryonic matter; face and cell centered magnetic fields (B^n_c, B^n_f); and Lagrangian dark matter mass, position, and velocity $(\rho^n_{DM}, \mathbf{x}^n, \mathbf{v}^n_{DM})$. These are all at time t^n. Where needed, primitive quantities will be described by $U = (\rho_{DM}, P_{gas}, \mathbf{v}_{DM}, \mathbf{B})$, and conserved quantities by $V = (\rho_{DM}, E_{total}, \mathbf{p}_{DM}, \mathbf{B})$. Conversion between the two is done as needed.

Step 1. Solve Poisson's equation for the acceleration field at $t^{n+\frac{1}{2}}$

$$\phi^n \Longleftarrow \rho^n_{BM} + \rho^n_{DM} \tag{2.70}$$

$$\phi^{n+1/2} = \phi^n(1 + \frac{\Delta t^n}{2\Delta t^{n-1}}) - \phi^{n-1}\frac{\Delta t^n}{2\Delta t^{n-1}} \tag{2.71}$$

$$g^{n+1/2}_i = \frac{1}{2a^{n+1/2}\delta x_i}(\phi^{n+1/2}_{i+1} - \phi^{n+1/2}_{i-1}) \tag{2.72}$$

Step 2.– Update particle positions and velocities. (Strictly speaking, this happens after the Expansion step, but the narrative works better if it's here.)

$$\mathbf{v}^{n+1/2}_{DM} = \mathbf{v}^n_{DM} - \frac{\Delta t^n}{2}\frac{\dot{a}^{n+1/2}}{a^{n+1/2}}\mathbf{v}^n_{DM} - \frac{\Delta t^n}{2}\mathbf{g}^{n+1/2} \tag{2.73}$$

$$\mathbf{x}^{n+1}_{DM} = \mathbf{x}^n_{DM} + \Delta t^n(\mathbf{v}^{n+1/2}_{i,DM}/a^{n+1/2}) \tag{2.74}$$

$$v^{n+1}_{i,DM} = v^{n+1/2}_{i,DM} - -\frac{\Delta t^n}{2}\frac{\dot{a}^{n+1/2}}{a^{n+1/2}}v^{n+1/2}_{i,DM} - \frac{\Delta t^n}{2}g^{n+1/2}_i \tag{2.75}$$

Step 3.– Apply half of the gravitational and expansion update to the fields

that require it, to obtain the temporary state $\tilde{U} = (\rho, \tilde{P}^n_{total}, \tilde{\mathbf{v}}^n_{BM}, \tilde{B}^n_c)$

$$\tilde{\mathbf{v}}^n_{BM} = \mathbf{v}^n_{BM} - \frac{\Delta t^n}{2}\frac{\dot{a}^n}{a^n}\mathbf{v}^n_{BM} - \frac{\Delta t^n}{2}\frac{1}{a^n}\mathbf{g}^{n+1/2} \tag{2.76}$$

$$\tilde{p}^n = p^n - \frac{\Delta t^n}{2}\frac{2\dot{a}^n}{a^n}p^n \tag{2.77}$$

$$\tilde{\mathbf{B}}^n_c = \mathbf{B}^n_c - \frac{\delta t^n}{4}\frac{\dot{a}^n}{a^n}\mathbf{B}_c \tag{2.78}$$

$$\tilde{U} = (\rho, \tilde{P}^n_{total}, \tilde{\mathbf{v}}^n_{BM}, \tilde{B}^n_c) \tag{2.79}$$

Step 4. Compute interface states at $i \pm \frac{1}{2}, n + \frac{1}{2}$ using linear spatial reconstruction and second order time integration:

$$U^{n+\frac{1}{2}}_{i+\frac{1}{2},L}, U^{n+\frac{1}{2}}_{i+\frac{1}{2},R} \Longleftarrow \tilde{U}_{i-1}, \tilde{U}_i, \tilde{U}_{i+1}, \tilde{U}_{i+2} \tag{2.80}$$

Step 5. Compute approximation of the flux in equation 2.25 at the interface $i + \frac{1}{2}$. This is done by solving the Riemann problem using one of the solvers mentioned in section 2.1.6

$$\hat{F}^{n\,\frac{1}{2}}_{i+\frac{1}{2}} = Riemann(U^{n+\frac{1}{2}}_{i+\frac{1}{2},L}, U^{n+\frac{1}{2}}_{i+\frac{1}{2},R}) \tag{2.81}$$

Step 6. Update the conserved quantities with the new fluxes:

$$(V^{n+1}_i)_{MHD} = V^n_i - \frac{\Delta t}{\Delta x}[\hat{F}_{i+\frac{1}{2}} - \hat{F}_{i-\frac{1}{2}}] \tag{2.82}$$

Step 7. Compute Electric field from Fluxes

$$E^{n+\frac{1}{2}}_{i+\frac{1}{2},j+\frac{1}{2}} \Longleftarrow \hat{F}_{i+\frac{1}{2}} \tag{2.83}$$

Step 9. Update magnetic fields from electric fields for the first time.

$$B^{n+1}_f = B^n_f - \frac{\Delta t}{a}\nabla \times E^{n+\frac{1}{2}}_{i+\frac{1}{2},j+\frac{1}{2}} \tag{2.84}$$

Step 8.–Gravitational step for the baryonic matter, with time centered density

$$(\mathbf{p}^{n+1}_{i,BM})_{MHD,Grav} = (\mathbf{p}^{n+1}_{i,BM})_{MHD} - \Delta t^n \frac{(\rho^n + \rho^{n+1}_{MHD})}{2} g^{n+1/2}_i \tag{2.85}$$

Step 9.–Expansion step for the baryonic matter,

$$(\mathbf{v}^{n+1}_{BM})_{MHD,Grav,exp} = \frac{1 - (\Delta t^n/2)(\dot{a}^{n+1/2}/a^{n+1/2})}{1 + (\Delta t^n/2)(\dot{a}^{n+1/2}/a^{n+1/2})}(\mathbf{v}^{n+1}_{BM})_{MHDGrav} \tag{2.86}$$

$$p^{n+1} = \frac{1 - (\Delta t^n)(\dot{a}^{n+1/2}/a^{n+1/2})}{1 + (\Delta t^n)(\dot{a}^{n+1/2}/a^{n+1/2})}(p^{n+1})_{MHD} \tag{2.87}$$

Step 10. Recurse to finer grids. Integrate fine grids from t^n to t^{n+1}

$$V^{n+1}_{FineGrids} \Longleftarrow V^{n}_{FineGrids} \tag{2.88}$$

Step 11.–Flux correction step for conserved baryon field quantities

$$V^{n+1}_{MHD,Grav,exp,fc} \Longleftarrow (\hat{F}^{n+1/2}), (\hat{F}^{n+1/2})_{FineGrids}, V^{n+1}_{MHDGrav,exp} \tag{2.89}$$

Step 12.–Project conserved baryon field quantities and electric field from fine grids to coarse grids. This is done *after* the flux correction step to avoid any bookkeeping errors. The average is taken over Δt^n and the surface of each $FineGrid$.

$$V^{n+1}_{ParentGrid} = \ < V^{n+1}_{FineGrid} >_{t,surface} \tag{2.90}$$

$$E^{n+\frac{1}{2}}_{ParentGrid} = \ < E^{n+\frac{1}{2}}_{FineGrid} >_{t,surface} \tag{2.91}$$

Step 13. Update magnetic fields from electric fields for the final time.

$$B^{n+1}_f = B^n_f - \frac{\Delta t}{a} \nabla \times E^{n+\frac{1}{2}}_{ParentGrid} \tag{2.92}$$

Step 14. Apply expansion to the Face Centered Fields

$$B^{n+1}_{f,exp} = \frac{1 - (\Delta t^n/4)(\dot{a}^{n+1/2}/a^{n+1/2})}{1 + (\Delta t^n/4)(\dot{a}^{n+1/2}/a^{n+1/2})} (B^{n+1}_f) \tag{2.93}$$

Step 15. Compute cell centered magnetic field from face centered (with the expansion subscript from step 9 dropped for clarity)

$$\begin{aligned} B^{n+1}_{c,x,i,j,k} &= 0.5 * (B_{f,x,i+\frac{1}{2},j,k} + B_{f,x,i-\frac{1}{2},j,k}) \\ B^{n+1}_{c,y,i,j,k} &= 0.5 * (B_{f,y,i,j+\frac{1}{2},k} + B_{f,y,i,j-\frac{1}{2},k}) \\ B^{n+1}_{c,z,i,j,k} &= 0.5 * (B_{f,z,i,j,k+\frac{1}{2}} + B_{f,z,i,j,k-\frac{1}{2}}) \end{aligned} \tag{2.94}$$

Step 16. We have now finished an update of this level. Rebuild the hierarchy from this level down.

$$V^{n+1}_{New\ FineGrids} \Longleftarrow V^{n+1} \tag{2.95}$$

$$B^{n+1}_{f,New\ FineGrids} \Longleftarrow B^{n+1}_f \tag{2.96}$$

Chapter 1 has been submitted in full for publication in The Astrophysical Journal Suppliment series as Collins, D.C., Xu, H., Norman, M.L., Li,H., & Li., S "Cosmological AMR MHD with Enzo"

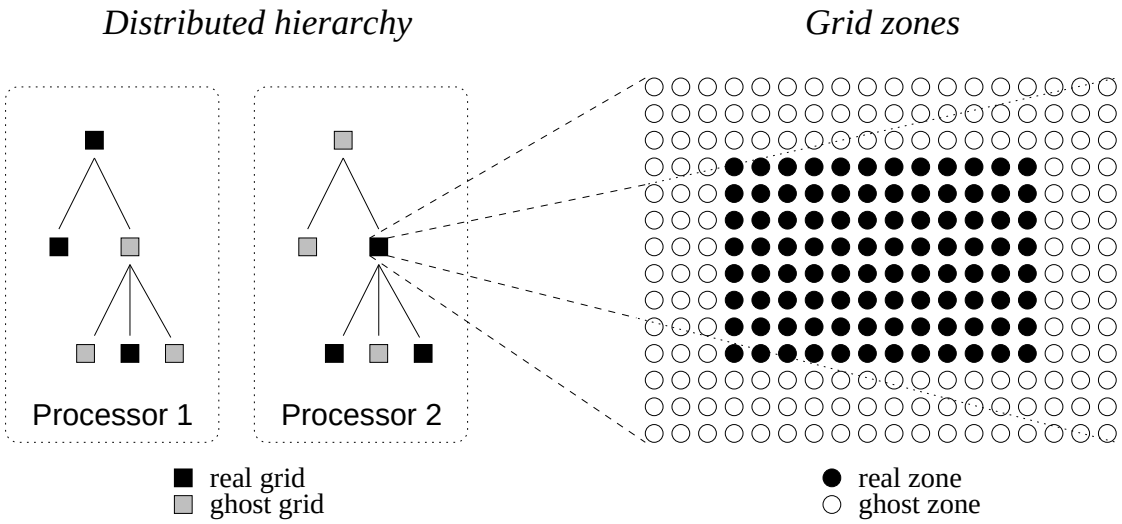

Figure 2.1: A schematic of a parallel AMR hierarchy on two processors (left) and a grid patch with ghost zones (right). Image courtesy James Bordner, initially appeared in (Norman et al., 2007)

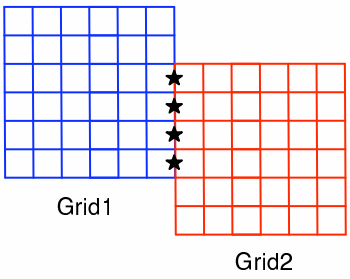

Figure 2.2: Data redundancy of the face centered magnetic fields: the face centered field denoted by the stars are updated by both grid 1 and grid 2. Enough ghost zones are exchanged to ensure that the entire stencil for the update of these fields is the same in both data structures.

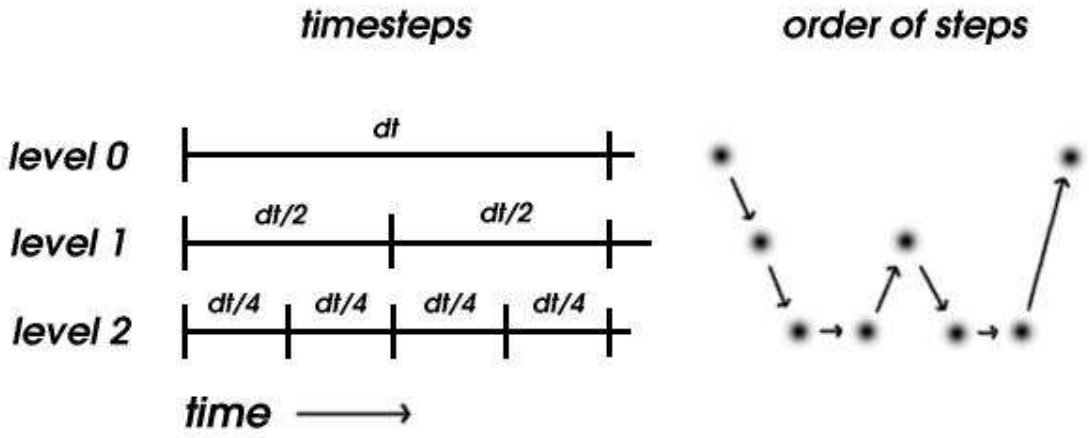

Figure 2.3: A depiction of the timestep strategy in Enzo

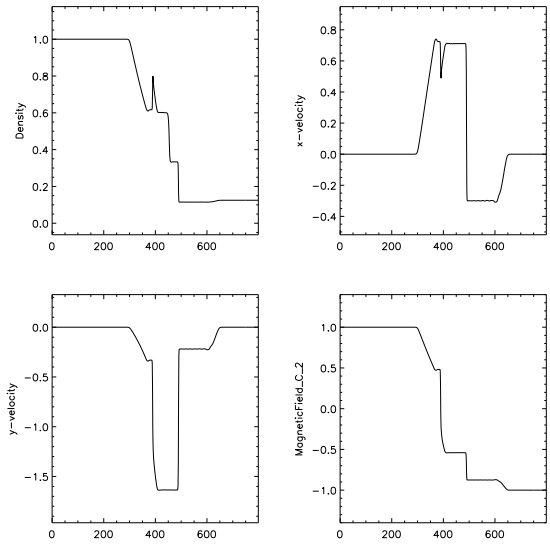

Figure 2.4: The shock tube of Brio & Wu (1988), showing from left to right a fast rarefaction, slow compound (shock+rarefaction), contact, slow shock, and fast rarefaction. T=0.08, and 800 zones were used.

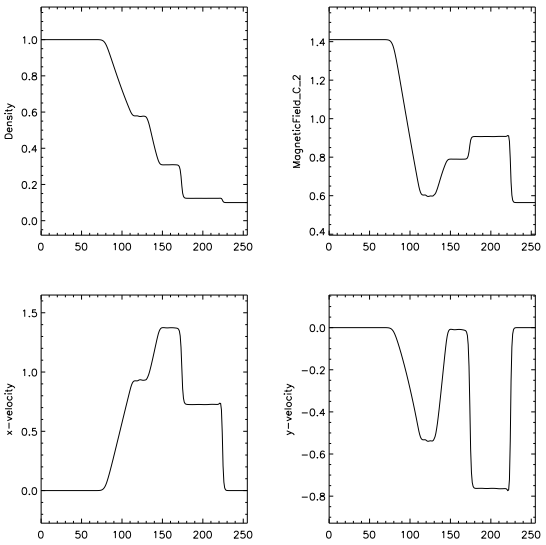

Figure 2.5: The shock tube of Kim et al. (1999), run with 256 zones to t=0.1.

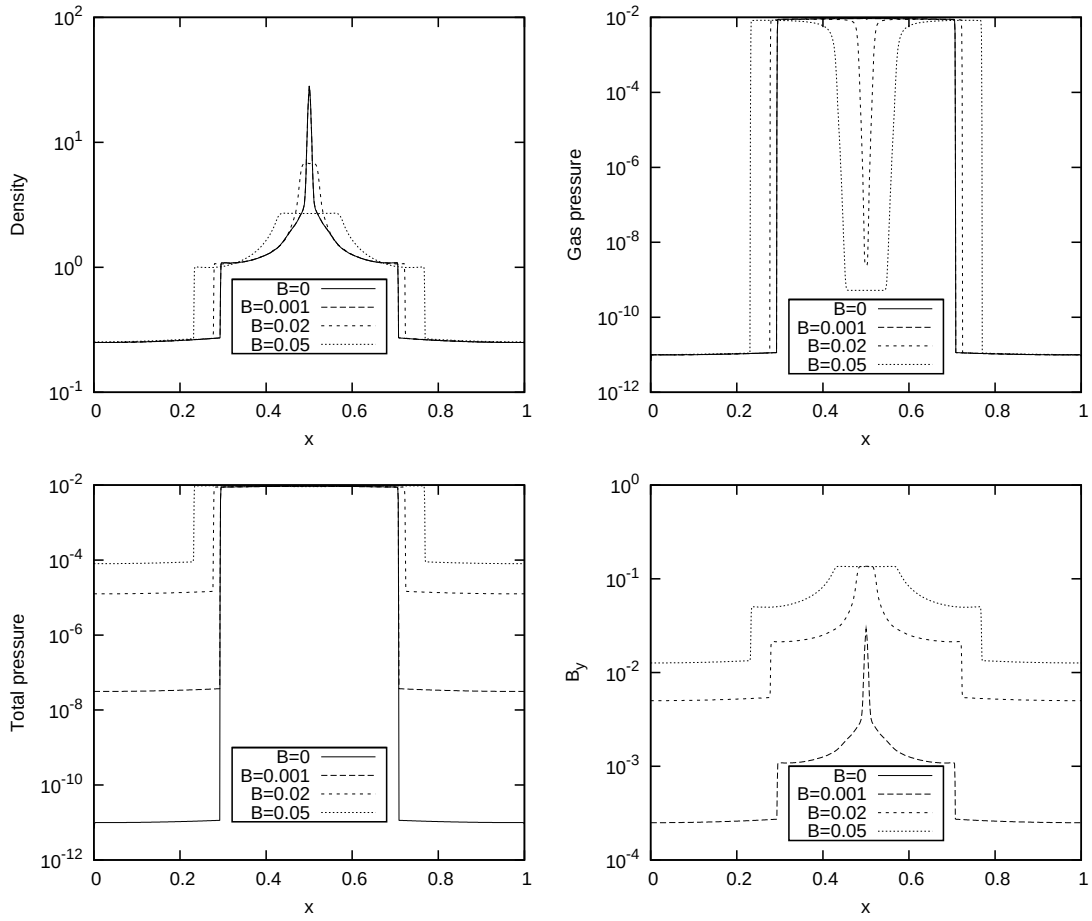

Figure 2.6: 1-D MHD caustics at $t = 3$. Density, gas pressure, total pressure and B_y are plotted. For the small field runs, almost no change can be seen, while larger field runs decrease the peak of the density considerably due to the increased pressure.

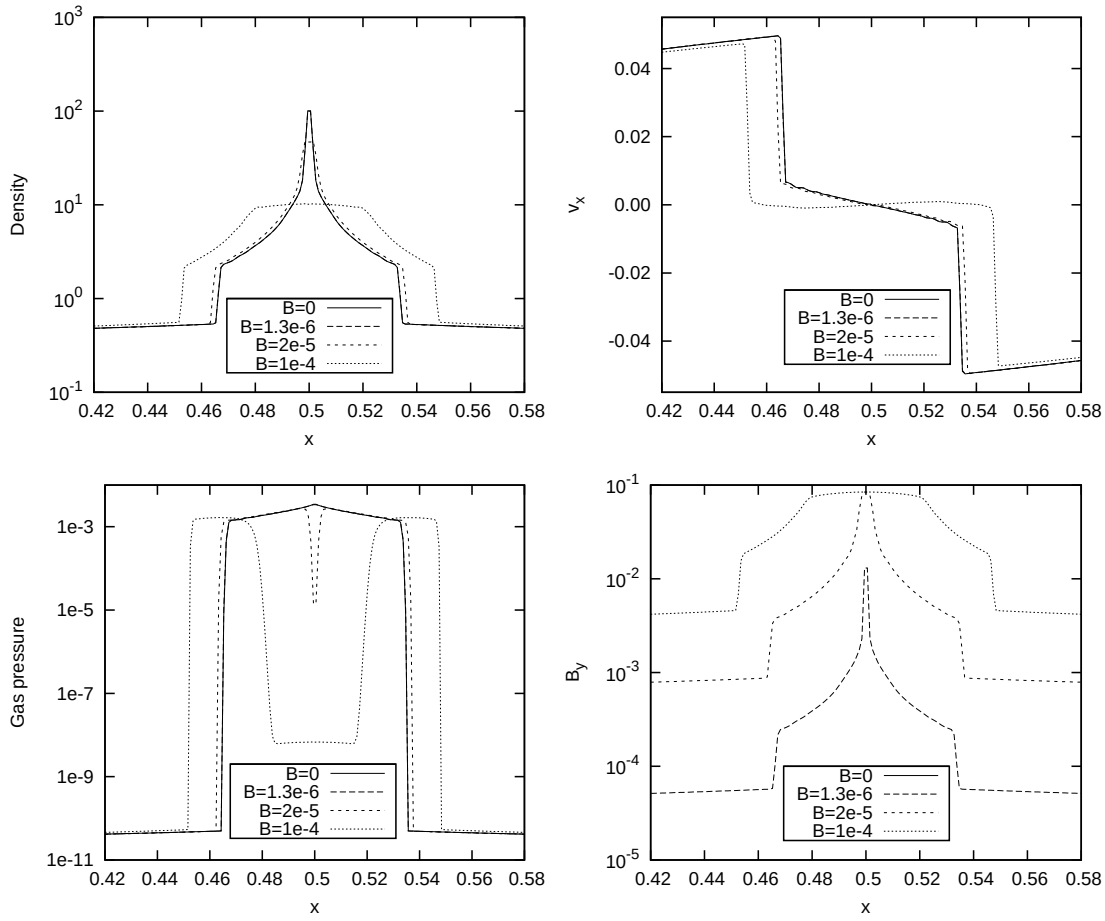

Figure 2.7: The Zel'Dovich Pancake problem with various values of the magnetic field, at $t = 0$. Increasing the magnetic field strength increases the central magnetic pressure, reducing the density and changing the overall solution structure. Results match those of Li et al. (2008).

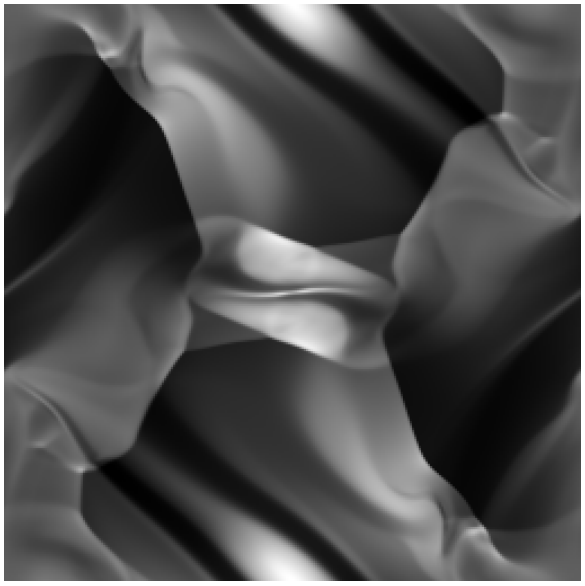

Figure 2.8: Density from the Orszag-Tang vortex, at t=0.48. Initial conditions are uniform density, with a single rotating velocity structure and two circular magnetic structures. This generates significant small scale structure, which has been used to compare effective resolution of different MHD schemes.

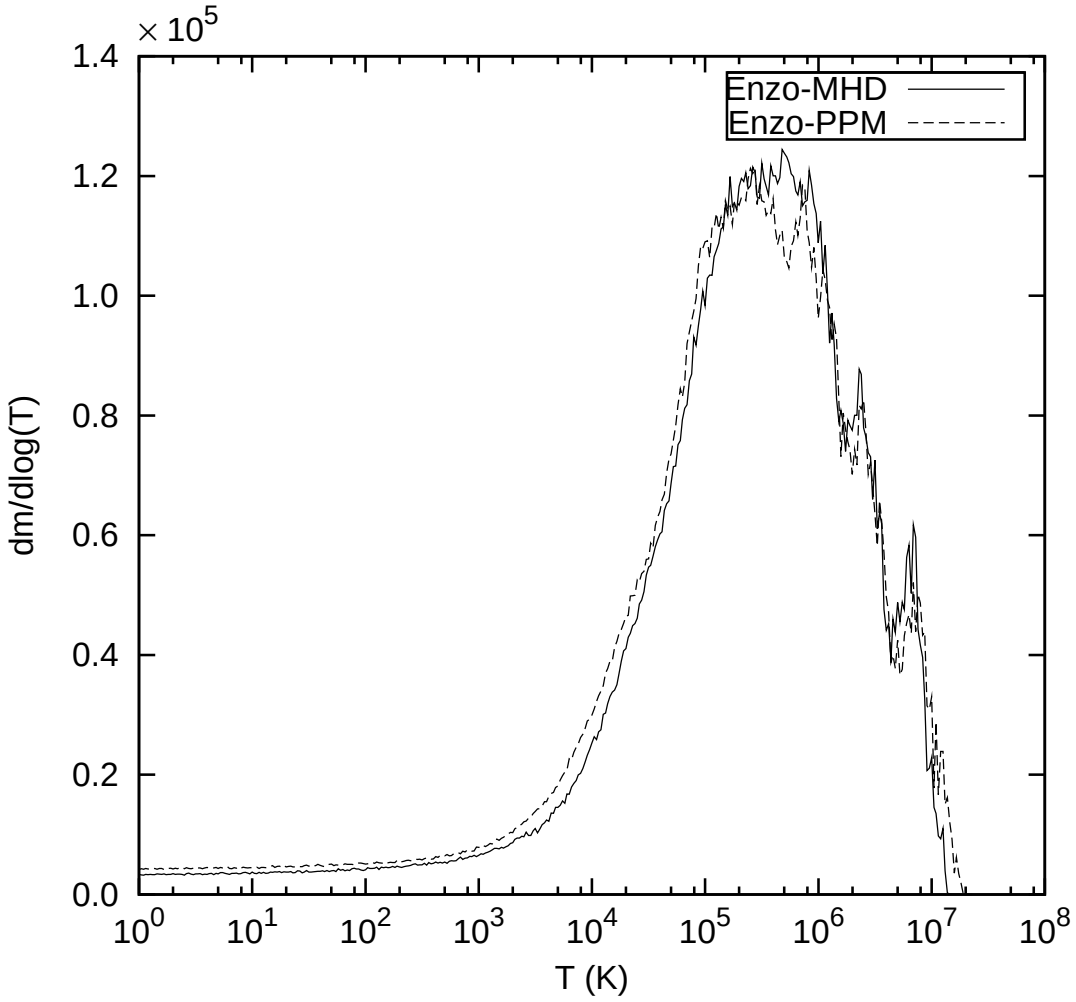

Figure 2.9: Comparison of mass-weighted temperature histogram at $z = 0$ for the 3D purely baryonic adiabatic Universe simulation. The solid line is from the MHD code and the dashed line is from Enzo-PPM.

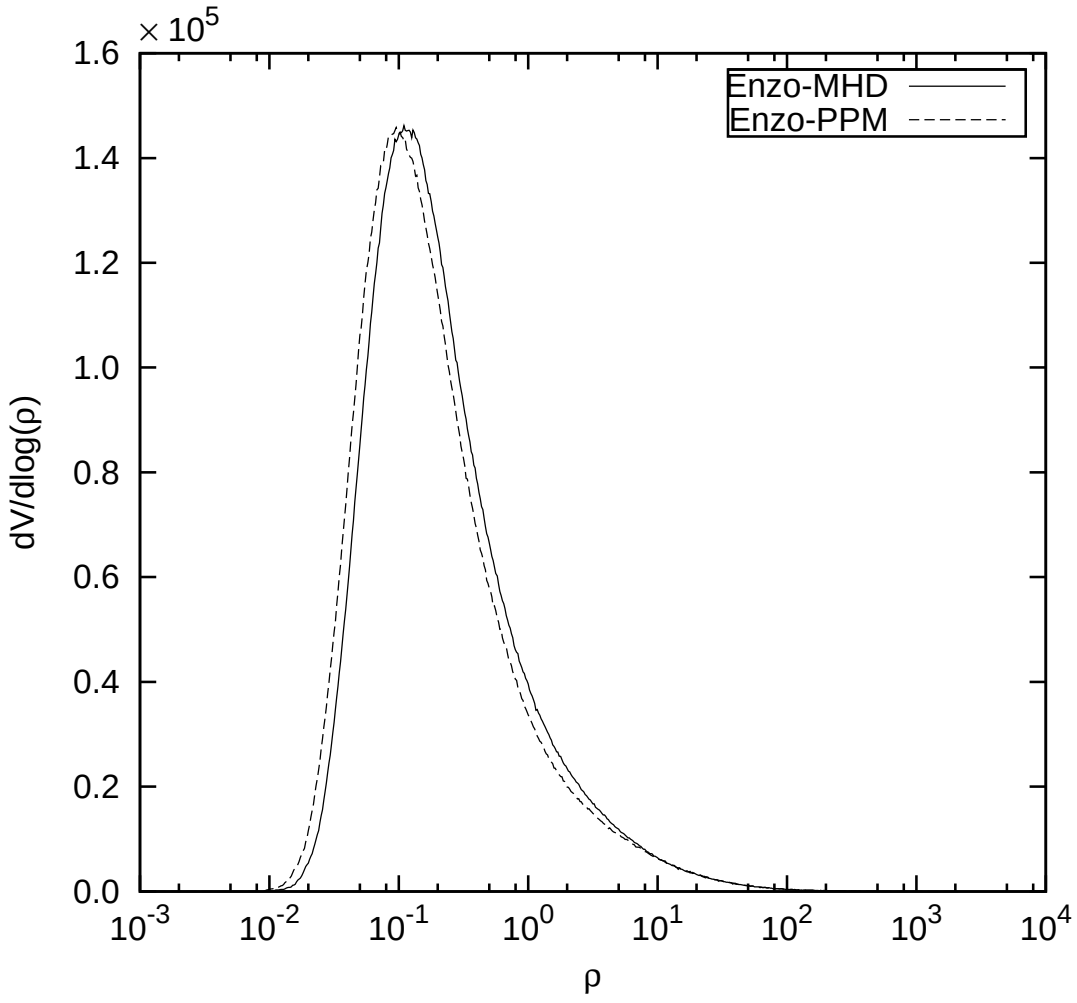

Figure 2.10: Comparison of volume-weighted density histogram at $z = 0$ for the 3D purely baryonic adiabatic Universe simulation. The solid line is from the MHD code and the dashed line is from Enzo-PPM.

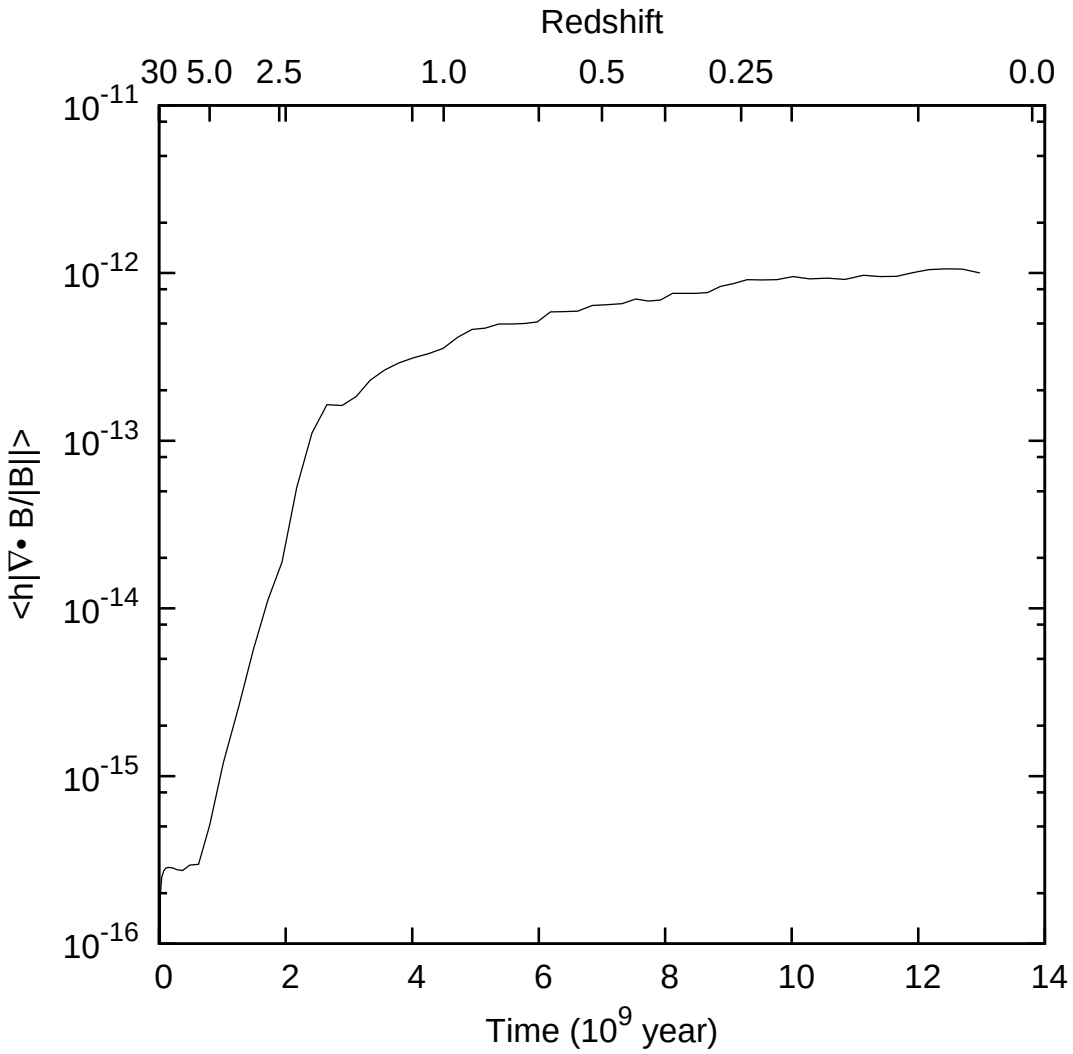

Figure 2.11: The scaled divergence $< |h\nabla \cdot \mathbf{B}/|\mathbf{B}|| >$ of the magnetic fields for the 3-D simulations of a purely baryonic adiabatic Universe. Here $h = 1/256$ is the scale length and $||B||$ is the local magnetic field norm, and the average is over the entire volume. Scaled divergence is a more relevant measure of numerical effects of divergence than the strict divergence. As desired, the divergence is near the machine round off noise, the theoretical limit.

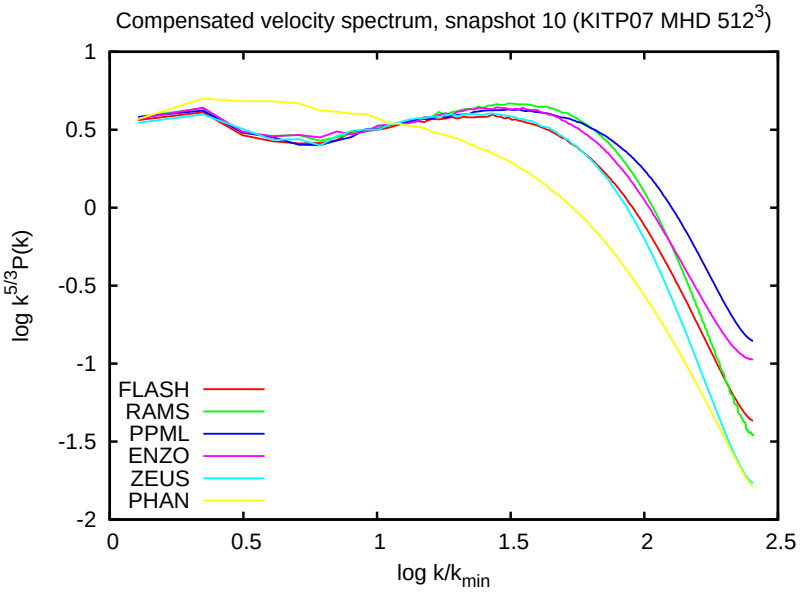

Figure 2.12: The power spectrum of the velocity field for 6 MHD codes on decaying MHD turbulence; Flash in red (Fryxell et al., 2000), Ramses in green, (Fromang et al., 2006), PPML in blue (Ustyugov & Popov, 2008) and 3.6, EnzoMHD with the Li solver in magenta, Zeus in light blue (Stone & Norman, 1992), and Phantom-SPH in yellow (Rosswog & Price, 2007). The Li solver has lower numerical viscosity than most other methods.

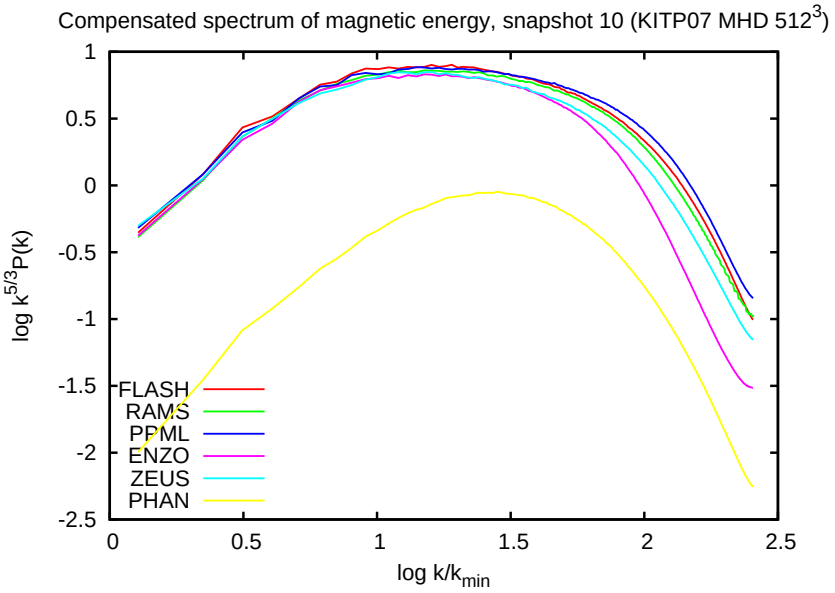

Figure 2.13: The power spectrum of the magnetic field for 6 MHD codes on decaying MHD turbulence; Flash in red (Fryxell et al., 2000), Ramses in green, (Fromang et al., 2006), PPML in blue (Ustyugov & Popov, 2008) and 3.6, EnzoMHD with the Li solver in magenta, Zeus in light blue (Stone & Norman, 1992), and Phantom-SPH in yellow (Rosswog & Price, 2007). The Li solver is somewhat more magnetically diffusive than the others.

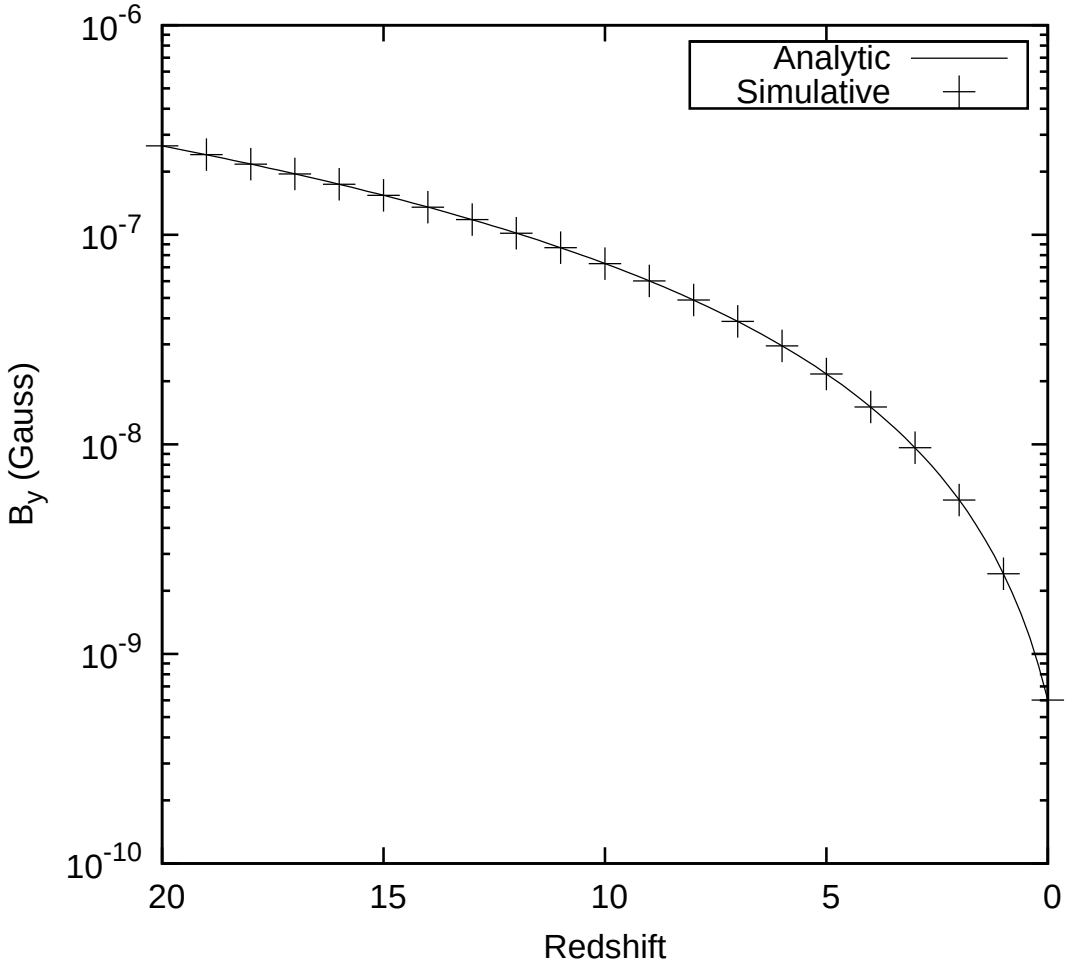

Figure 2.14: Magnetic field in the y direction in the AMR MHD adiabatic expansion test. The pluses show the results of simulation and the solid line is the analytic result.

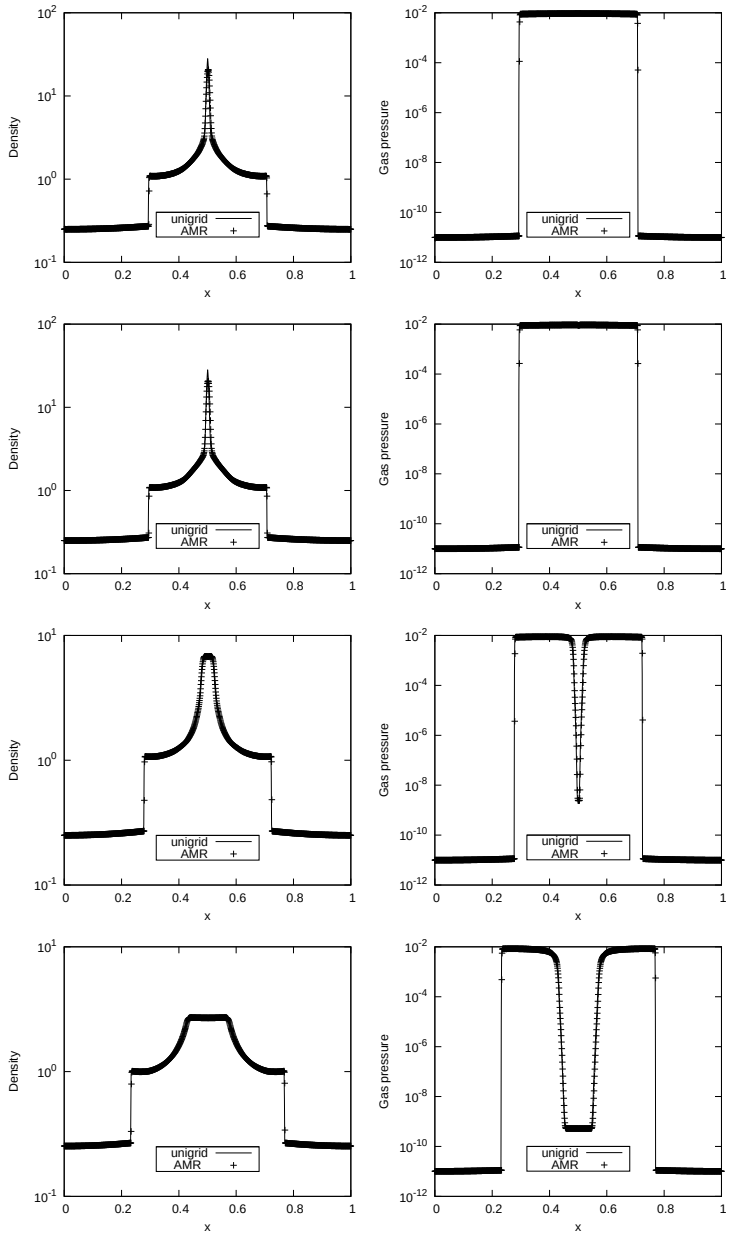

Figure 2.15: Comparisons of density and pressure in the MHD Caustic tests, non-AMR vs AMR. The left column shows density and the right column shows gas pressure. Initial magnetic field of each row from top to bottom is 0, 0.001, 0.02 and 0.05.

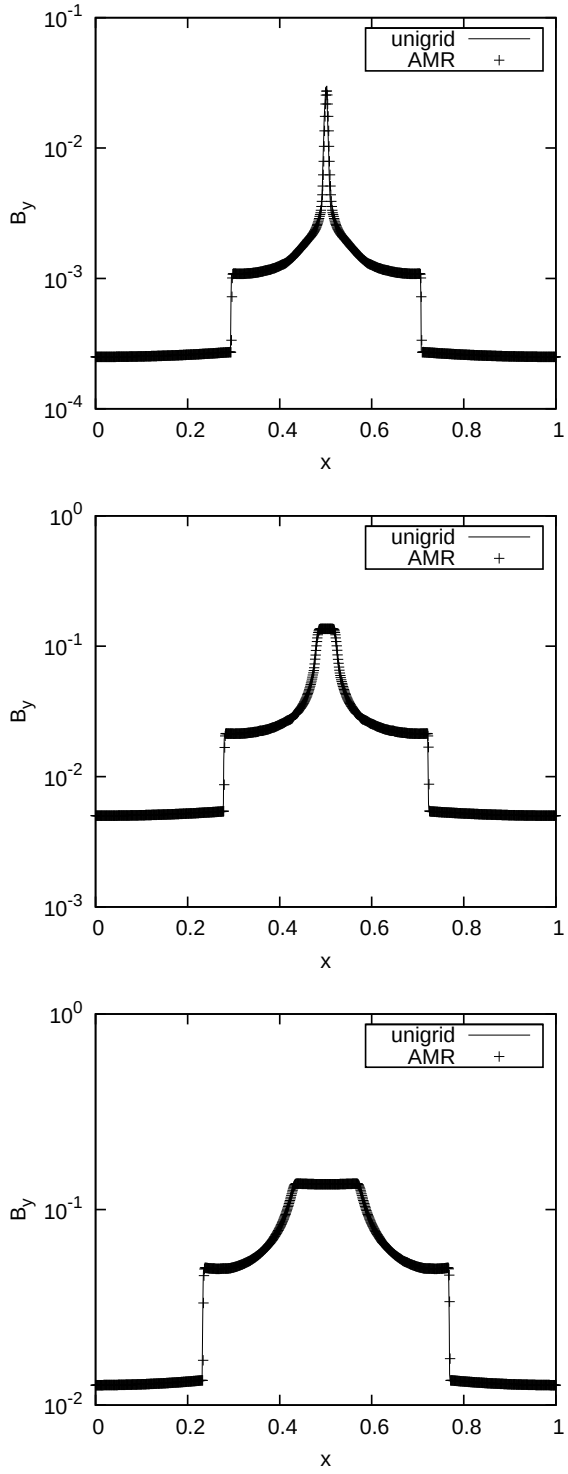

Figure 2.16: Comparison of B_y in the MHD Caustic tests, non-AMR vs AMR. Initial magnetic field of each panel from top to bottom is 0.001, 0.02 and 0.05.

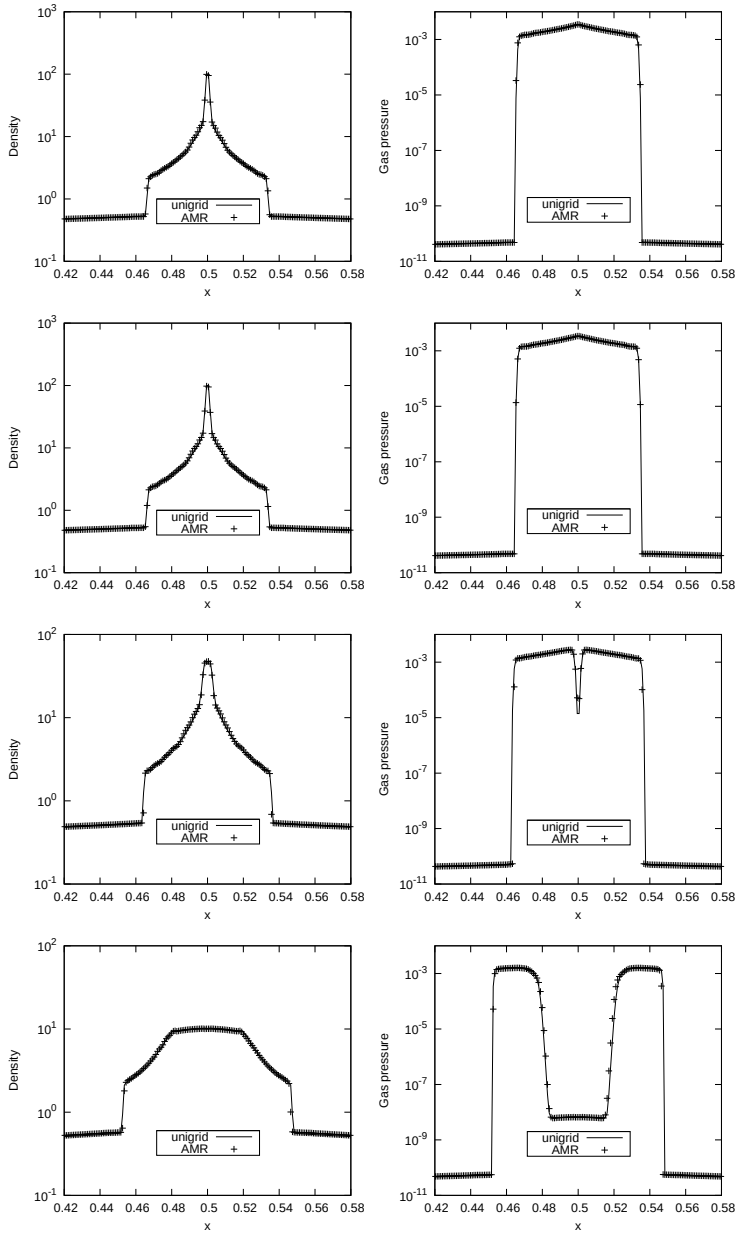

Figure 2.17: Comparisons of density and pressure in non-AMR and AMR runs of the Pancake test. The left column shows density and the right column shows gas pressure. Initial magnetic field of each row from top to bottom is 0, 1.3e-6G, 2e-5G and 1e-4G.

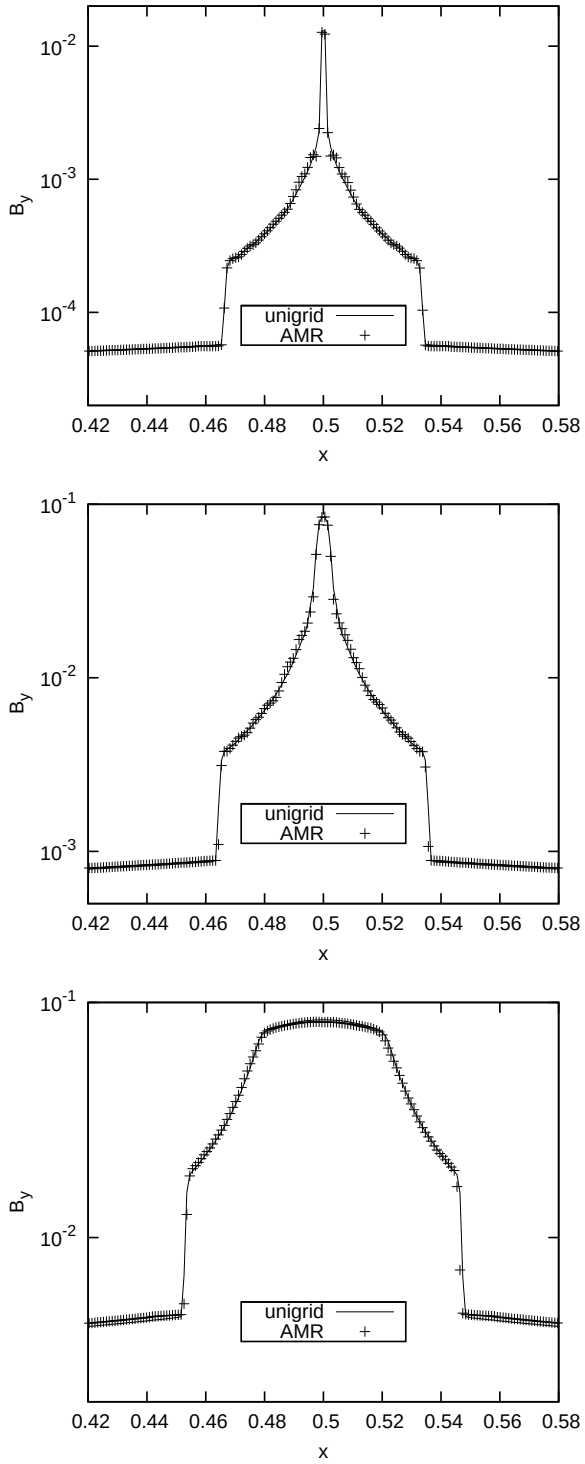

Figure 2.18: Comparisons of magnetic y component in non-AMR and AMR runs of the Pancake test. Initial magnetic field of each panel from top to bottom is 1.3e-6, 2e-5 and 1e-4G.

Chapter 3

Trial and Error: DaveThena and other solvers

The MHD solver presented in chapter 2 was not the first MHD method installed in EnzoMHD. There were three iterations before that one, each with their own strengths but ultimately irreconcilable weaknesses. In this chapter, we will describe the other solvers and their shortcomings. This will be done in chronological order of installation. First will be the method of Ryu & Jones (1995), in section 3.1. Then in section 3.2 will be a new method called DaveThena, designed to be a lightweight version of the Athena method of Gardiner & Stone (2005). Finally in section 3.6 we will describe in brief PPML, another new method, the lone physical instability that prevented us from continuing to use both it and DaveThena, and a brief summary of the potential resolution.

3.1 The Ryu and Jones method.

The first solver implemented in Enzo was the TVD method by Harten (1983), as extended to MHD by Ryu & Jones (1995). This method is a second order extension of the first order method described by Roe. It was later extended to 3d (Ryu et al., 1998), by way of directional splitting and a Constrained Transport type method for updating the induction equation. A brief summary of this method will be given here.

3.1.1 The method

Essentially this method is a combination of two first order methods in such a way that the first order methods cancel, and we're left with a second order method. The two methods are due to Harten and Roe, and are both Approximate Godunov type schemes. Both methods can be viewed as piecewise constant spatial reconstructions and approximate Riemann solvers. The First Order Harten method computes the interface flux F^* as a piecewise quadratic interpolation between $F(U_L)$ and $F(U_R)$. The Roe method computes the interface flux F^* by first linearizing 2.23 as

$$\frac{\partial \boldsymbol{Q}}{\partial t} + \boldsymbol{A}\frac{\partial \boldsymbol{Q}}{\partial x} = 0 \tag{3.1}$$

$$\boldsymbol{A} = \frac{\partial \boldsymbol{F}}{\partial \boldsymbol{Q}} \tag{3.2}$$

and then solving the piecewise-constant Riemann problem with U_L and U_R as initial data. In hydrodynamics, this has an analytic solution. In MHD, a linearized solution is usually used, due to the computational overhead of finding the exact solution.

The two are then combined using the minmod function, see equation 3.11. The first order terms cancel and leave us with a formally second order accurate scheme.

3.1.2 Turbulent Evolution: Ryu and Jones

The Ryu and Jones method was determined to be too diffusive to use for our star formation application. As discussed in 4.8, it is believed that the shape of the turbulent power spectrum determines the mass distribution of protostellar objects, and in turn the mass distribution of stars. Failure to resolve any part of the spectrum properly will cause incorrect statistics of cores. Unfortunately, the slope of the velocity power spectrum obtained for this method was extremely steep, and the statistics of cores found using this solver would be untrustworthy.

In standard Kolmogorov turbulence theory, which holds up quite well in practice, the transfer of energy from large scale to small scale is a conservative process, with dissipation only occurring at the smallest scale where microphysics

and inelastic collisions between molecules takes place. See section 1.3 In numerical simulations, this dissipation is happens at the grid scale by the effective numerical viscosity of the method. If the dissipation of the method is too large, this will cause destruction of structures at the scales larger than the dissipation scale, manifest itself as a steeper spectrum in the velocity.

Padoan et al. (2007) perform a set of simulations using the Stagger code (which has no method paper), the Zeus MHD code (Stone & Norman, 1992). They find slopes of -1.9 and -2.2, respectively. Padoan et al. (2006) measured the power spectrum in the molecular clouds, and got a value of 1.8 ± 0.1, which is shallower still than the other two results.

A driven turbulence simulation at Mach 5 with a weak magnetic field $\mathbf{B} = [0, 0, 0.1]$ was performed with the Ryu and Jones code. The driving was performed as in sections 2.2.1, 3.5, and 4.1 The slope of the power spectrum is measured to be -2.4, which is substantially steeper than that of the other two simulations and *much* steeper than the cloud we're trying to model. For this, the method was abandoned and a less dissipative method was sought. This led to the inclusion of the Li method in section 2.1.6, the development of the DaveThena method (section 3.2) and the inclusion of the PPML method (section 3.6).

3.2 DaveThena: the new Athena.

The basic patch solver for DaveThena is, like all numerical methods, and assembly of other parts. Essentially it is a higher order Godunov method with linear reconstruction, several choices for Riemann solver, several choices for CT, including both Balsara (Balsara & Spicer, 1999) and Gardiner & Stone (2005), and second order Runge Kutta time integration. Rather than directional splitting, which has been the standard method for turning one dimensional algorithms into three dimensional ones, we difference our fluxes in a completely unsplit manner.

The code is formulated as one integration step, which is applied twice as a predictor-corrector or 2^{nd} order Runge-Kutta integration. The basic integrator goes as follows:

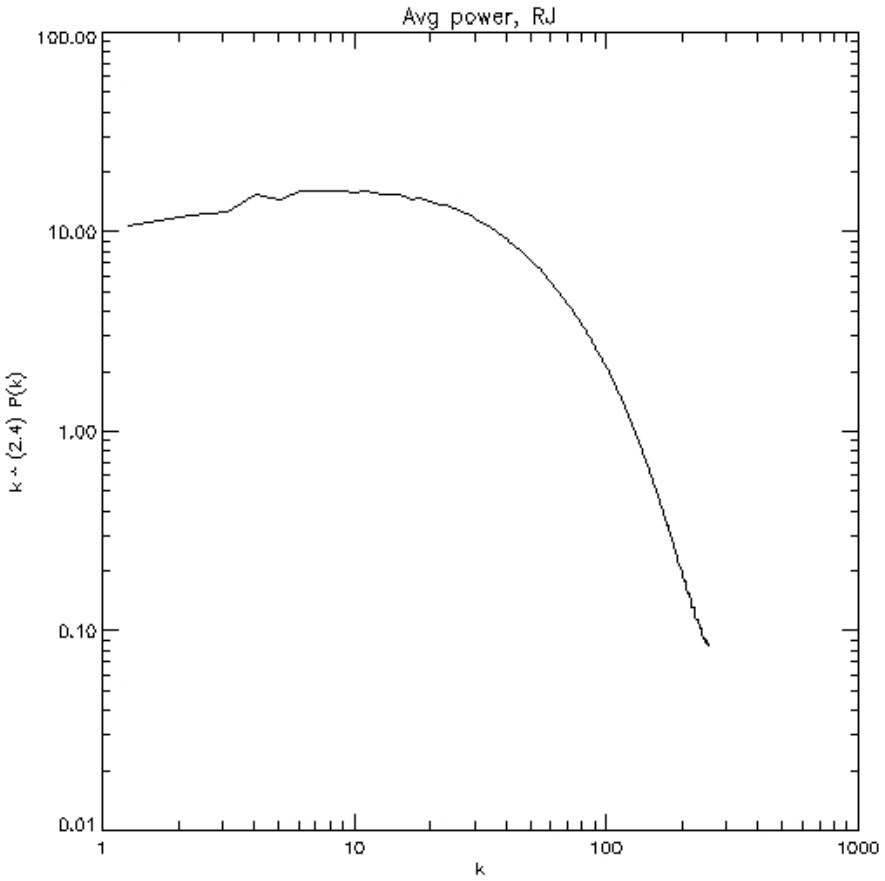

Figure 3.1: Velocity power spectrum for a Mach 5, β=100 simulation. The spectrum is fit to an index of -2.4, and plotted compensated so the inertial range is in the plot. This slope is much steeper than what has been seen in other simulations, demonstrating excessive dissipation in the numerical scheme.

1. **Spatial Reconstruction** Left and Right states are computed by one of several methods. Currently there are only two, piecewise constant or piecewise linear, but in principle any other method can be incorporated with relative ease. More will be said on this step in section 3.2.1

2. **Flux computation** Fluxes at each face are computed with, again, a variety of methods. These will be described in section 3.2.2

3. **Unsplit Flux Differencing** Fluxes are then differenced as in equation 2.48 in section 2.3.1.

4. **Constrained Transport** The electric field at the cell edges is computed using one of three options: Balsara & Spicer (1999), and the two major options from Gardiner & Stone (2005). More will be said in section 3.2.4

5. $\mathbf{B_f^{n+1}} = \mathbf{B_f^n} + \nabla \times \mathbf{E}$. That's kind of self explanatory. Central differences for $\mathbf{E}$ yield a divergence free update for $\mathbf{B_f}$

6. **Compute Cell Centered Field** The cell centered magnetic field is then computed from the Face Centered magnetic field. Simple direct average is used:
$$B_{x,i,j,k} = \frac{1}{2}(B_{x,i+\frac{1}{2},j,k} + B_{x,i-\frac{1}{2},j,k}) \tag{3.3}$$

This formulation is the applied in two steps, using 2^{nd} order Runge Kutta method. That is:

$$\begin{aligned} \hat{V}^{n+\frac{1}{2}} &= \hat{V}^n - \frac{\Delta t}{2}(\ \nabla \cdot \hat{F}(\hat{Q}^n)\ ) \\ \hat{V}^{n+1} &= \hat{V}^n - \Delta t(\ \nabla \cdot \hat{\hat{F}}(\hat{V}^{n+\frac{1}{2}})\ ) \end{aligned} \tag{3.4}$$

Some of the 6 steps described above have several options associated with it, which will be discussed in the next section, and the user is not tied to using the same option for both steps. For instance, the flux in the first step of equation 3.4, $\hat{F}$, can be computed using a lower order-accurate, and thus faster, formulation than the second step, $\hat{\hat{F}}$. For instance, a piecewise constant step and first order

flux approximation for the first step, with a piecewise linear reconstruction and HLLD solver for the second.

Every numerical method requires some number of ghost zones. These zones are used for interpolation of a given cell, and must be filled by some method. Details can be found in section 2.1.5. Due to the two step solution here, ghost zones must be considered for both steps. In principle, two options exist when it comes to filling the ghost zones used by the correct step. Either it can be saved as an extra layer of ghost zones, and updated by the predict step, or a communication step can be done between predict and correct steps. AMR makes this slightly more than just another instance of the age old speed vs. memory debate. The additional concern is the ghost zones of refined regions that need to get their ghost zones interpolated from parent grid cells. It seemed more consistent to the code authors to have as few interpolations from parent grids as possible, since this is a much coarser approximation to the solution than actually advancing the equations.

3.2.1 Reconstruction Options

The spatial reconstruction has several options. The order of the reconstruction can either be piecewise constant or piecewise linear. This can be selected independently for each sub-step. The linear reconstruction can be created with either the minmod or Van Leer slope limiters. The minmod tends to be a more severe slope limiter, so is used for quantities that self steepen, namely velocity, while Van Leer tends to be somewhat steeper, so is used for fields that don't naturally steepen on their own, namely density and magnetic field. This wisdom is from Balsara & Kim (2004). Lastly, it wasn't obvious from the literature whether primitive or conservative variables would give the best results, so for the "kinematic" quantities the user can switch between reconstructing velocity and momentum, while for "energetic" quantities the user can switch between total energy, gas pressure, total pressure (gas + magnetic), or enthalpy. It is recommended and demonstrated in 3.4.1 that Balsara was indeed correct, and vanLeer should be used on density and magnetic field, while minmod should be used on velocity and energy.

3.2.2 Flux options

There are several flux options available in EnzoMHD, as well. Current options are the linearized solver of Roe, as described by Cargo & Gallice (1997), the robust solver HLLE (Toro, 1999), the contact preserving MHD HLLC (Li, 2005) and HLLD (Miyoshi & Kusano, 2005). Because of the unsplit nature of the code, all fluxes for all fields are stored for the entire grid patch. This yields 21 fields per cell.

3.2.3 Finite Difference Equations with Sources

In gory detail, here is an update of the DaveThena method, including the gravitational and driving source terms.

For reference, we'll define the following, which map to the variables of the same name in Enzo.

U = BaryonField, MagneticField. Used for both full and half time step updates.

O = OldBaryonField, OldMagneticField.

$$U, O = \begin{pmatrix} \rho \\ (\rho v_x, \rho v_y, \rho v_z) \\ (B_x, B_y, B_z) \\ E \end{pmatrix} \tag{3.5}$$

Source Terms:

$$G = \begin{pmatrix} 0 \\ (\rho a_x, \rho a_y, \rho a_z) \\ (0,0,0) \\ \rho(a_x v_x + a_y v_y + a_z v_z) \end{pmatrix} (gravity) \tag{3.6}$$

$$D = \begin{pmatrix} 0 \\ (A\delta v_x, A\delta v_y, A\delta v_z) \\ (0,0,0) \\ \rho A\delta \boldsymbol{v} \cdot (\boldsymbol{v} + \frac{1}{2} A\delta \boldsymbol{v}) \end{pmatrix} (driving) \tag{3.7}$$

Pre-Step, ala Ryu et al. (1993):

$$U = U + \frac{\Delta t}{2} G \tag{3.8}$$

The Update: Linear Reconstruction

$$U_{L,i-\frac{1}{2},j,k} = U_{i-1,j,k} + \frac{1}{2}\Delta_x U_{i-1,j,k} \tag{3.9}$$

$$U_{R,i-\frac{1}{2},j,k} = U_{i,j,k} + \frac{1}{2}\Delta_x U_{i,j,k} \tag{3.10}$$

Limited slopes to reduce oscillation

$$\Delta_x U_{i,j,k} = minmod(U_{i+1} - U_i, U_i - U_{i-1}) \tag{3.11}$$

Compute flux. Choices include HLLE, HLLC, and Roe.

$$F_{x,Riemann} = ... \tag{3.12}$$

Add Artificial Viscosity. It has been found that the unsplit method of Saltzman (1994) is imperative if turbulence is to be done. This method is a fully 3 dimensional and fully unsplit viscosity method. It's basic formulation is the same as Colella & Woodward (1984), but the viscosity coefficient at the zone face $\nu_{i+\frac{1}{2},j,k}$ is formulated as the spatial average of the divergence at the corners. in short, ν is proportional to the divergence of v, $\nu = -min(\nabla \cdot \boldsymbol{v}, 0)$ For Colella & Woodward (1984), the divergence is as follows:

$$F_x(U_{L,i-\frac{1}{2}}, U_{R,i-\frac{1}{2}}) = F_{x,Riemann}(U_{L,i-\frac{1}{2}}, U_{R,i-\frac{1}{2}}) - \eta\nu_{x,i-\frac{1}{2}} * (U_i - U_{i-1}) \tag{3.13}$$

$$\eta = 0.01 - 0.1 \tag{3.14}$$

$$\begin{aligned}\nu_x = max(0, v_{x,L,i-\frac{1}{2}} - v_{x,R,i-\frac{1}{2}} + \frac{\Delta x}{4\ \Delta y}(&v_{y,i,j-1,k} - v_{y,i,j+1,k} \\ &+ v_{y,i-1,j-1,k} - v_{y,i-1,j+1,k}) \\ + \frac{\Delta x}{4\ \Delta z} + (&v_{z,i,j,k-1} - v_{z,i,j,k+1} \\ &+ v_{z,i-1,j,k-1} - v_{z,i-1,j,k+1})\ )\end{aligned}$$

For Saltzman (1994),

$$\nu_{x,i+\frac{1}{2},j,k} = -\eta\ min(0, 0.25 \sum_{\substack{j'=-1,0 \\ k'=-1,0}} C_{i+\frac{1}{2},j+\frac{1}{2}+j',k+\frac{1}{2}+k'}) \tag{3.15}$$

(so the average of the corners of the face) and

$$C_{i+\frac{1}{2},j+\frac{1}{2},k+\frac{1}{2}} = \frac{1}{4}(\frac{1}{\Delta x}\Delta_i(u + u_{j+1} + u_{k+1} + u_{j+1,k+1}) \tag{3.16}$$

$$\frac{1}{\Delta y}\Delta_j(v + v_{i+1} + v_{j+1} + v_{i+1,j+1}) \tag{3.17}$$

$$\frac{1}{\Delta z}\Delta_k(w + w_{j+1} + w_{k+1} + w_{j+1,k+1})) \tag{3.18}$$

(so the velocity divergence). In the last equation, u, v, w are the 3 velocity components, dropped subscripts refer to i, j, k where omitted, and $\Delta_i F = F_i - F_{i-1}$ is the difference of F in the i direction. Cyclically permute i, j and k as needed. Unsplit predictor flux difference:

$$U'_{i,j,k} = O_{i,j,k} - \frac{\Delta t}{2\Delta x}(F_x(U_{L,i+\frac{1}{2}}, U_{R,i+\frac{1}{2}}) - F_x(U_{L,i-\frac{1}{2}}, U_{R,i-\frac{1}{2}}) \tag{3.19}$$

$$- \frac{\Delta t}{2\Delta y}(F_y(U_{L,j+\frac{1}{2}}, U_{R,j+\frac{1}{2}}) - F_y(U_{L,j-\frac{1}{2}}, U_{R,j-\frac{1}{2}}) \tag{3.20}$$

$$- \frac{\Delta t}{2\Delta z}(F_z(U_{L,k+\frac{1}{2}}, U_{R,k+\frac{1}{2}}) - F_z(U_{L,k-\frac{1}{2}}, U_{R,k-\frac{1}{2}}) \tag{3.21}$$

$$+ \frac{\Delta t}{2}(\frac{1}{2}(G_{U'} + G_O)) \tag{3.22}$$

$$+ \frac{1}{2}D \tag{3.23}$$

By equation 3.22 we mean the "time centered ish" gravitational terms, ala Colella & Woodward (1984):

$$\frac{1}{2}(G_{U'} + G_O) = \begin{pmatrix} 0 \\ (\rho' + \rho)a_x, \\ ... \\ \frac{1}{2}a_x(\rho' v'_x + \rho v_x) + ... \end{pmatrix} \tag{3.24}$$

Unsplit corrector: Repeat steps 3.9 and 3.12, if desired also 3.13

$$U''_{i,j,k} = O_{i,j,k} - \frac{\Delta t}{\Delta x}(F_x(U'_{L,i+\frac{1}{2}}, U'_{R,i+\frac{1}{2}}) - F_x(U'_{L,i-\frac{1}{2}}, U'_{R,i-\frac{1}{2}}) \tag{3.25}$$

$$- \frac{\Delta t}{\Delta y}(F_y(U'_{L,j+\frac{1}{2}}, U'_{R,j+\frac{1}{2}}) - F_y(U'_{L,j-\frac{1}{2}}, U'_{R,j-\frac{1}{2}}) \tag{3.26}$$

$$- \frac{\Delta t}{\Delta z}(F_z(U'_{L,k+\frac{1}{2}}, U'_{R,k+\frac{1}{2}}) - F_z(U'_{L,k-\frac{1}{2}}, U'_{R,k-\frac{1}{2}}) \tag{3.27}$$

$$+ \Delta t(\frac{1}{2}(G_{U''} + G_O)) \tag{3.28}$$

$$+ D \tag{3.29}$$

In a slightly more compact form, letting H cover reconstruction, Riemann solver, and artificial viscosity; and ∇ defined as the unsplit finite difference operator, and $\tilde{G}$ as the "time centered(ish)" gravity, we can write:

$$\begin{aligned} U' &= U - \frac{\Delta t}{2}\nabla \cdot H(U) + \frac{dt}{2}\tilde{G} + \frac{1}{2}D \\ U'' &= U - \Delta t \nabla \cdot H(U') + \Delta t \tilde{G} + D \end{aligned} \tag{3.30}$$

Note that I've also tried fully splitting the driving out the way its done in Enzo, so the update is the following. No substantial difference was noticed.

$$\begin{aligned} U &= U + D \\ O &= U \\ U' &= O - \frac{\Delta t}{2}\nabla \cdot F(U) \\ U'' &= O - \Delta t \nabla \cdot F(U') \end{aligned} \tag{3.31}$$

3.2.4 CT options

DaveThena also has 3 CT options:

1. **Balsara** Electric Field is the direct average of the adjacent fluxes from the Riemann Solver

2. **Athena 1** Electric Field is computed using a Lax-Wendroff type integration, involving both fluxes at the interfaces and Magnetic Field and Velocity data at the cell center.

3. **Athena 2** Electric Field is computed with a much simpler linear reconstruction, selected bases on the fluid velocity direction.

3.3 Finite Difference Equations for CT

In this section we will outline the details of the Constrained Transport (CT) algorithms used in EnzoMHD. First we will present induction equation, which will motivate the use of the edge centered electric fields. Computation of the electric fields will be presented next. Figure 3.3 shows the centering of the electric and magnetic fields on a cube centered at (i, j, k). In section 3.3.1, we will demonstrate why CT works. In section 3.3.2 we will present the method of Balsara & Spicer (1999), in sections 3.3.3 and 3.3.4 we will present the Lax-Friedrichs and switched method of methods of Gardiner & Stone (2005), respectively.

3.3.1 CT and $\nabla \cdot \mathbf{B}$

The time derivative of the divergence of the magnetic field is identically zero because it is the divergence of the curl of a field:

$$\frac{\partial \mathbf{B}}{\partial t} = -\nabla \times \mathbf{E} \tag{3.32}$$

$$\frac{\partial \nabla \cdot \mathbf{B}}{\partial t} = -\nabla (\nabla \times \mathbf{E}) \tag{3.33}$$

$$= 0. \tag{3.34}$$

We mirror this numerically by updating the magnetic field with the curl of a field in such a way that the most obvious choice for its divergence is zero. It should be noted that the divergence operator can be defined a number of different ways, and in practice and principle satisfying $\nabla \cdot \mathbf{B} = 0$ in all possible operators is not possible. As mentioned in section 2.1.2, we store the magnetic field in the faces of

zones. See figure 3.3. The most natural divergence operator is then

$$\nabla \cdot \mathbf{B} \equiv \frac{1}{\Delta x}(B_{f,x,i+\frac{1}{2},j,k} - B_{f,x,i-\frac{1}{2},j,k}) \\ \frac{1}{\Delta y}(B_{f,y,i,j+\frac{1}{2},k} - B_{f,y,i,j-\frac{1}{2},k}) \quad (3.35)$$

$$\frac{1}{\Delta z}(B_{f,z,i,j,k+\frac{1}{2}} - B_{f,z,i,j,k-\frac{1}{2}}). \quad (3.36)$$

If we define the electric field on the edges of the zone, we can define the induction equation as

$$B^{n+1}_{f,x,i-\frac{1}{2},j,k} = B^{n}_{f,x,i-\frac{1}{2},j,k} - \Delta t(\frac{1}{\Delta y}(E_{z,i-\frac{1}{2},j+\frac{1}{2},k} - E_{z,i-\frac{1}{2},j-\frac{1}{2},k}) + \\ \frac{1}{\Delta z}(E_{y,i-\frac{1}{2},j,k+\frac{1}{2}} - E_{y,i-\frac{1}{2},j,k-\frac{1}{2}})) \quad (3.37)$$

$$B^{n+1}_{f,y,i,j-\frac{1}{2},k} = B^{n}_{f,y,j-\frac{1}{2},k} - \Delta t(\frac{1}{\Delta z}(E_{x,i,j-\frac{1}{2},k+\frac{1}{2}} - E_{x,i,j-\frac{1}{2},k+\frac{1}{2}}) + \\ \frac{1}{\Delta x}(E_{z,i+\frac{1}{2},j-\frac{1}{2},k} - E_{z,i-\frac{1}{2},j-\frac{1}{2},k})) \quad (3.38)$$

$$B^{n+1}_{f,z,i,j,k-\frac{1}{2}} = B^{n}_{x,i,j,k-\frac{1}{2}} - \Delta t(\frac{1}{\Delta x}(E_{y,i+\frac{1}{2},j,k-\frac{1}{2}} - E_{y,i-\frac{1}{2},j,k-\frac{1}{2}}) + \\ \frac{1}{\Delta y}(E_{x,i,j+\frac{1}{2},k-\frac{1}{2}} - E_{x,i,j-\frac{1}{2},k-\frac{1}{2}})). \quad (3.39)$$

Carefully plugging the magnetic field update from equation 3.38 into 3.35, one finds

$$\nabla \cdot \mathbf{B_f}^{n+1} = \nabla \cdot \mathbf{B_f}^{n} \quad (3.40)$$

so if $\nabla \cdot \mathbf{B} = 0$ at the initial conditions, it will be so for all time, to machine precision. The next step is computing the electric field.

3.3.2 Direct Average Electric Field

The first CT method implemented was that of Balsara & Spicer (1999). This can be viewd as a piecewise linear average of the electric field components that are returned by the Riemann solver at the centers of faces to the corner they share. We will follow the notation of Balsara & Spicer (1999) in defining the fields. Let the conservation law be given by

$$\frac{\partial \mathbf{V}}{\partial t} + \frac{\partial \mathbf{F}}{\partial x} + \frac{\partial \mathbf{G}}{\partial y} + \frac{\partial \mathbf{H}}{\partial z} = 0, \quad (3.41)$$

where state vector $\mathbf{V}$ and fluxes $\mathbf{F}, \mathbf{G}, \mathbf{H}$ are

$$\mathbf{V}_{6,7,8} = \begin{pmatrix} \cdots \\ B_x \\ B_y \\ B_z \end{pmatrix} \tag{3.42}$$

$$\mathbf{F}_{6,7,8} = \begin{pmatrix} \cdots \\ 0 \\ -E_z \\ E_y \end{pmatrix} \tag{3.43}$$

$$\mathbf{G}_{6,7,8} = \begin{pmatrix} \cdots \\ E_z \\ 0 \\ -E_x \end{pmatrix} \tag{3.44}$$

$$\mathbf{H}_{6,7,8} = \begin{pmatrix} \cdots \\ -E_y \\ E_x \\ 0 \end{pmatrix}. \tag{3.45}$$

We have suppressed the hydrodynamic arguments $\rho, \mathbf{v}, E$ and their fluxes for simplicity. The electric fields a the cell edges is the average of the electric fields in the faces that touch it. So the electric field at $(i, j+\frac{1}{2}, k+\frac{1}{2})$ is the average of all the relevant quantities at $(i, j+\frac{1}{2}, k), (i, j+\frac{1}{2}, k+1), (i, j, k+\frac{1}{2})$, and $(i, j+1, k+\frac{1}{2})$. Following the electric components from the fluxes, we find

$$E_{x,i,j+\frac{1}{2},k+\frac{1}{2}} = \frac{1}{4} \begin{pmatrix} H_{7,i,j,k+\frac{1}{2}} + H_{7,j+1,k+\frac{1}{2}} \\ -G_{8,i,j+\frac{1}{2},k} - G_{8,i,j+\frac{1}{2},k+1} \end{pmatrix} \tag{3.46}$$

$$E_{y,i+\frac{1}{2},j,k+\frac{1}{2}} = \frac{1}{4} \begin{pmatrix} F_{8,i+\frac{1}{2},j,k} + F_{8,i+\frac{1}{2},j,k+1} \\ -H_{6,i,j,k+\frac{1}{2}} - H_{6,i+1,j,k+\frac{1}{2}} \end{pmatrix} \tag{3.47}$$

$$E_{z,i+\frac{1}{2},j+\frac{1}{2},k} = \frac{1}{4} \begin{pmatrix} G_{6,i,j+\frac{1}{2},k} + G_{6,j+1,j+\frac{1}{2},k} \\ -F_{7,i+\frac{1}{2},j,k} - F_{7,i+\frac{1}{2},j+1,k} \end{pmatrix} \tag{3.48}$$

3.3.3 Lax-Friedrichs Electric Field

The previous method can be seen as a piecewise constant interpolation of each flux at the face center, eg. $(i, j, k+\frac{1}{2})$, to the edge, eg. $(i, j+\frac{1}{2}, k+\frac{1}{2})$. The Athena method of Gardiner & Stone (2005) is a linear interpolation:

$$E_{z,i+\frac{1}{2},j+\frac{1}{2}-\epsilon,k} = E_{z,i+\frac{1}{2},j,k} + \frac{\Delta y}{2}\left(\frac{\partial(E_z)}{\partial y}\right)_{i+\frac{1}{2},j+\frac{1}{4},k} \tag{3.49}$$

that is, the z component of the electric field at $(i+\frac{1}{2}, j+\frac{1}{2}, k)$, approached from below along y. There are four such components, from below and above, along x and and along y. The full computation is then

$$\begin{aligned} E_{z,i+\frac{1}{2},j+\frac{1}{2},k} = \frac{1}{4}&\left(E_{z,i+\frac{1}{2},j,k} + E_{z,i+\frac{1}{2},j+1,k} + E_{x,i,j+\frac{1}{2},k} + E_{x,i+1,j+\frac{1}{2},k}\right) \\ &+\frac{\Delta y}{8}\left(\left(\frac{\partial E_z}{\partial y}\right)_{i+\frac{1}{2},j+\frac{1}{4},k} - \left(\frac{\partial E_z}{\partial y}\right)_{i+\frac{1}{2},j+\frac{3}{4},k}\right) \\ &+\frac{\Delta x}{8}\left(\left(\frac{\partial E_z}{\partial x}\right)_{i+\frac{1}{4},j+\frac{1}{2},k} - \left(\frac{\partial E_z}{\partial x}\right)_{i+\frac{3}{4},j+\frac{1}{2},k}\right). \end{aligned} \tag{3.50}$$

This section and the next concern the computation of the derivatives of the electric field.

In the first method, the standard numerical integration scheme of Lax and Friedrichs (Lax, 1954) is used to compute the derivatives at $(i+\frac{1}{2}, j+\frac{1}{4})$, $(i+\frac{1}{2}, j+\frac{3}{4})$, $(i+\frac{1}{4}, j+\frac{1}{2})$ and $(i+\frac{3}{4}, j+\frac{1}{2})$. Where not included, the z index is assumed to be k.

We will begin our discussion with a description of the LF method for a linearized conservation law, and then apply it to the derivative of the electric field. Begin with a linearized conservation law of the form

$$\frac{\partial u}{\partial t} + \frac{\partial f}{\partial x} = 0, \tag{3.51}$$

This can be discretized in a number of ways. The LF method is a Forward Time Center Space (FTCS) method, with the initial time taken as the arithmetic mean of u_{i+1} and u_{i-1}. See the excellent book by Laney (1998) for a full description of discretization methods. Equation 3.51 is discretized as

$$\frac{u^{n+1} - \frac{1}{2}(u^n_{i+1} + u^n_{i-1})}{\Delta t} + \frac{f(u^n_{i+1}) + f(u^n_{i-1})}{2\Delta x} = 0. \tag{3.52}$$

Rearranging, one arrives at

$$u_i^{n+1} = u_i^n - \frac{1}{\lambda}(\hat{f}_{i+\frac{1}{2}} - \hat{f}_{i-\frac{1}{2}}) \tag{3.53}$$

$$\hat{f}_{i+\frac{1}{2}} = \frac{1}{2}\left(f(u_{i+1}^n) + f(u_i^n)\right) - \frac{\lambda}{2}(u_{i+1}^n - u_i^n) \tag{3.54}$$

where $\lambda = \Delta x/\Delta t$ is the wave speed.

We derive an estimate for $(\partial E_z/\partial x)_{i+\frac{1}{4},j+\frac{1}{2}}$ by deriving the flux from applying equation 3.54 to the x derivative of the induction equation:

$$\frac{\partial}{\partial t}\left(\frac{\partial B_x}{\partial x}\right) + \frac{\partial}{\partial y}\left(\frac{\partial E_z}{\partial x}\right) = 0. \tag{3.55}$$

We will compute the analog of the centered-space flux from equation 3.54 at $(i + \frac{1}{4}, j + \frac{1}{2})$ by computing the flux for 3.55 along the y axis at $i + \frac{1}{4}$. This requires us to define

$$\left(\frac{\partial B_x}{\partial x}\right)_{i+\frac{1}{4},j} = \frac{2}{\Delta x}\left(B_{f,x,i+\frac{1}{2},j} - B_{c,x,i,j}\right) \tag{3.56}$$

$$\left(\frac{\partial E_z}{\partial x}\right)_{i+\frac{1}{4},j} = \frac{2}{\Delta x}\left(E_{z,i+\frac{1}{2},j} - E_{z,i,j}\right) \tag{3.57}$$

where $B_{f,x,i+\frac{1}{2},j}$ is the face centered magnetic field, $B_{c,x,i,j}$ is the cell centered magnetic field gotten from the averaging of B_f, $E_{z,i+\frac{1}{2},j}$ is computed from the flux from the Riemann solver at the same point, and $E_{z,i,j} = v_x B_{c,y} - v_y B_{c,x}$ is the cell centered electric field. Plugging this into the LF scheme, treating equation 3.56 as u and equation 3.57 as f, we get

$$\begin{aligned}\left(\frac{\partial E_z}{\partial x}\right)_{i+\frac{1}{4},j+\frac{1}{2}} =& \frac{1}{\Delta x}\left(E_{z,i+\frac{1}{2},j} - E_{z,i,j} + E_{z,i+\frac{1}{2},j+1} - E_{z,i,j+1}\right) \\ &+ \frac{\lambda}{\Delta x}\left(B_{f,x,i+\frac{1}{2},j} - B_{c,x,i,j} + B_{f,x,i+\frac{1}{2},j+1} + B_{c,x,i,j+1}\right)\end{aligned} \tag{3.58}$$

After repeating this argument for all necessary components, and putting the answer

in 3.50, we arrive at

$$\begin{aligned} E_{z,i+\frac{1}{2},j+\frac{1}{2}} =& \frac{1}{2}(E_{z,i,j+\frac{1}{2}} + E_{z,i+1,j+\frac{1}{2}} + E_{z,i+\frac{1}{2},j} + E_{z,i+\frac{1}{2},j+1}) \\ & - \frac{1}{4}(E_{z,i,j} + E_{z,i+1,j} + E_{z,i,j+1} + E_{z,i+1,j+1}) \\ & + \frac{\lambda}{8}(B_{f,x,i+\frac{1}{2},j} - B_{c,x,i,j} - B_{f,x,i+\frac{1}{2},j+1} + B_{c,x,i,j+1}) \\ & + \frac{\lambda}{8}(B_{f,x,i+\frac{1}{2},j} - B_{c,x,i+1,j} - B_{f,i+\frac{1}{2},j+1} + B_{c,x,i+1,j+1} \\ & + \frac{\lambda}{8}(B_{f,y,i+1,j+\frac{1}{2}} - B_{c,y,i+1,j} - B_{f,y,i,j+\frac{1}{2}} + B_{c,y,i,j}) \\ & + \frac{\lambda}{8}(B_{f,y,i+1,j+\frac{1}{2}} - B_{c,y,i+1,j+1} - B_{f,y,i,j+\frac{1}{2}} + B_{y,i,j+1}) \end{aligned} \tag{3.59}$$

It should be noted that by itself, LF is somewhat prone to even-odd instabilities, though the method is globally stable. See Laney (1998), chapter 17 for more details

3.3.4 Velocity Switched Electric Field

The other scheme is essentially an upwinded version of equation 3.59 with $\lambda = 0$. Simply setting $\lambda = 0$ will result in an unstable method. However, we can improve the method with upwinding, by switching the electric field direction based on the fluid velocity:

$$\left(\frac{\partial E_z}{\partial y}\right)_{i+\frac{1}{2},j+\frac{1}{4}} \begin{cases} \left(\frac{\partial E_z}{\partial y}\right)_{i,j+\frac{1}{4}} & \text{for } v_{x,i+\frac{1}{2},j} > 0 \\ \left(\frac{\partial E_z}{\partial y}\right)_{i+1,j+\frac{1}{4}} & \text{for } v_{x,i+\frac{1}{2},j} < 0 \\ \frac{1}{2}\left(\left(\frac{\partial E_z}{\partial y}\right)_{i,j+\frac{1}{4}} + \left(\frac{\partial E_z}{\partial y}\right)_{i+1,j+\frac{1}{4}}\right) & \text{otherwise.} \end{cases} \tag{3.60}$$

Equation 3.60 is then used in equation 3.50. It has been found in turbulence tests not presented here that this method is preferred, as it is suppresses the small oscillations seen in the previous method.

3.4 Tests

3.4.1 One Dimension

Brio and Wu shock tube

As discussed in 2.2.1, the shock tube defined by Brio & Wu (1988) is a standard test of any MHD solver. It displays a number of the important MHD waves, including a compound wave. Compound waves are not a property of pure hydrodynamics, because the system is convex. However, due do the more complex nature of the MHD equations, certain initial conditions can cause flows in which at one point the shock speed in a given family is higher than the wave speed for that family, causing a shock, but lower in the post shock region, causing a rarefaction immediately following the shock.

The initial conditions are $(\rho = 1, v_x = 0, v_y = 0, v_z = 0, B_y = 1, B_z = 0, P = 1)$ on the left, $(\rho = 0.125, v_x = 0, v_y = 0, v_z = 0, B_y = -1, B_z = 0, P = 1)$ on the right. $B_x = 0.75$, and $\gamma = 1.4$

The test shows, from right to left, a fast rarefaction, slow compound (shock + rarefaction), contact, slow shock, and fast rarefaction.

This was the primary test of the various switches in the method. This test was run combining a huge variety of the solver switches available to DaveThena. Only 4 are shown here, due to the fact that this solver is not likely to see the light of day once I graduate. These have been saved, and interested readers can contact me if you're actually going to be using the solver.

Figure 3.4 shows the least expensive and least accurate method, with piecewise constant for both predict and correct step. It is completely non-oscillatory, but also quite diffusive. Figure 3.5 shows the minmod slope limiter, which is the more diffusive limiter, on all fields, and primitive variables. It's less diffusive than the constant reconstruction, as expected. Figure 3.6 shows what happens if one uses the vanLeer limiter, the more compressive limiter, on the conservative fields. One can see that certain options in this code can cause catastrophic results. Figure 3.7 is done with the "recommended" set, using vanLeer on density and magnetic field, and minmod on velocity and total energy. For ease of reference, figure 3.8 shows an

enlargement of the density for the constant, minmod, and "recommended" setups.

Kim Isothermal

In order to verify correct behavior in the isothermal solver, we have also performed the first one dimensional shock tube of Kim et al. (1999). The initial conditions are $(\rho = 1, v_x = 0, v_y = 0, v_z = 0, B_y = 5/(4\pi)^{\frac{1}{2}}, B_z = 0)$ $(\rho = 0.1, v_x = 0, v_y = 0, v_z = 0, B_y = 2/(4\pi)^{\frac{1}{2}}, B_z = 0)$ on the left. $B_x = 3/(4\pi)^{1/2}$. It shows fast and slow rarefactions to the left, and fast and slow shocks to the right. Because this is an isothermal run, there is no contact discontinuity. We ran this with both the isothermal solver and the adiabatic solver, with $\gamma = 1.001$. The adiabatic solver shows one small overshoot and oscillation in the density, immediately after the slow shock. Other than that, the two solvers behave almost identically. Figure 3.9 shows the non-constant fluid quantities after a time of 0.1, solved on a computational grid of 512 zones.

3.4.2 Two Dimensions

The Orszag-Tang Vortex was originally developed by Orszag & Tang (1979) to demonstrate that small scale structure can be generated by the nonlinearities in the MHD equations. It initially starts with a single large scale rotating velocity structure and two circular magnetic structures. From these simple large scale initial conditions, substantial small scale structure is formed. It now serves as a standard test problem to demonstrate the accuracy and diffusivity of MHD codes.

The initial conditions are on a 2 dimensional periodic box, 256 zones on a side. $\mathbf{v} = v_0(-sin(2\pi y)\hat{x} + sin(2\pi x)\hat{y}, \mathbf{B} = B_0(-sin(2\pi y)\hat{x} + sin(4\pi x)\hat{y}), v_0 = 1, B_0 = 1/\sqrt{4\pi}, \rho_0 = 25/(36\pi), p_0 = 5/(12\pi)$, and $\gamma = 5/3$ which gives a peak Mach number of 1 and peak $\beta = p_0/(B_0^2/2) = 10/3$. Figure 3.10 shows the density at $t = 0.48$ for both the Ryu and Jones method (top) and the DaveThena method (bottom), both at 256^2 resolution. One can see immediately that the DaveThena solver has substantially more structure resolved, indicating less diffusion in the solver. This is exactly what we wanted from the development of this solver.

Loop Advection

In Gardiner & Stone (2005), they describe a test specifically designed to break the CT method of Balsara-Spicer. It consists of a loop of magnetic field contained within a radius R, no field outside, and is advected obliquely to the grid. Specifically, the domain is $-1 \leq x \leq 1$ by $-0.5 \leq y \leq 0.5$. Results shown here use $128x64$ zones. Density $\rho = 1$ and pressure $P = 1$, velocity $\mathbf{v} = v0[2/\sqrt{5}, 1/\sqrt{5}]$, where $v0 = 1/\sqrt{5}$. The magnetic field is initialized from a vector potential $\mathbf{A} = [0, 0, A_z]$, where

$$A_z = \begin{cases} A_0(R - r) & for\ r \leq R \\ 0 & for\ r > R \end{cases} \tag{3.61}$$

3.5 Comparison of Turbulent Evolution: Enzo Options

As discussed in sections 2.2.1 and 3.1.2, turbulence is an excellent measure of the dissipation of a method. In order to quantify the performance of a code, specifically the numerical diffusion of the method. We did a Mach 5, zero-field simulation with 256^3 zones using DaveThena, PPML, PPM, and the Li method, and the results of the power spectrum can be seen in figure 3.12. Unfortunately, on this test DaveThena doesn't perform as well as one would have liked. The power falls off quite rapidly. The fit to this spectrum is $P(k) \propto k^{-2.2}$, which while not as bad as the Ryu and Jones method, not as good as the other options available in EnzoMHD. In principle I would like to have compared the Ryu and Jones method directly in the comparison, but it was not deemed worth the resources at the time. The small scale turn up of the PPML spectrum is not understood, and it is not believed to be present in other runs.

3.6 PPML

A fourth method for MHD was introduced and showed great promise before an uncorrected error unsplit MHD was found. This bug will be discussed in section 3.7

PPM on a Local Stencil (PPML) (Ustyugov & Popov, 2008) is an extension of the PPM method of Colella & Woodward (1984). In regular PPM, a parabolic reconstruction of the data in a given cell V_i is obtained by using the data points V_{i-2} through V_{i+2}. This parabola is used to reconstruct the interface states at the zone faces at $V_{L,i+\frac{1}{2}}$ and $V_{R,i-\frac{1}{2}}$. (Here, L and R refer to which side of the interface the state is on.) This gives regular PPM a 5 point stencil. The Riemann problem is then solved with an approximate solver using $V_{L,i-\frac{1}{2}}$ and $V_{R,i-\frac{1}{2}}$, which gives a flux that updates the interface.

In order to reduce the numerical diffusion in the code, Ustyugov & Popov (2008) reduce the stencil to (almost) a single point. They do this by actually storing $V_{L,i+\frac{1}{2}}$ and $V_{R,i-\frac{1}{2}}$ for the entire simulation, and evolving them using a second call to the Riemann problem. This effectively doubles the resolution, but more than halves the numerical dissipation, as the stencil is reduced by two zones on either side.

This is done in an unsplit manner, much like what is done in Gardiner & Stone (2005). It was seen that this code and DaveThena are both subject to the instability described in the next section. This has been rectified in a different version of PPML, but not in DaveThena.

3.7 One Shortcoming of Unsplit Methods: Catastrophic Instability

Both DaveThena and PPML pass the regimen of standard of test problems quite well. However, in the standard regimen there are no strongly supersonic turbulence simulations, which it turns out is quite good at exposing numerical instabilities. Figure 3.13 demonstrates this problem. Both panels in the figure

show the density field in Mach 3 driven turbulence. The left panel has no magnetic field, the panel at right has $B = [0, 0, \sqrt{2}]$. Peak density in the left panel is 33 times the mean, in the right panel the peak density is 100 times the mean, and grows in a few timesteps to 3e4 times the mean. This is extremely unphysical. This instability is seen in both DaveThena and PPML.

Recently, it has been reported that this bug has been fixed in PPML by incorporating the divergence constraint in the reconstruction of the fields. However, this fix came after we began using the Li solver discussed in chapter 2, so was not incorporated into Enzo in either solver.

3.8 Other necessary Enzo fixes

Keeping the divergence of the magnetic field below 1×10^{-10} is quite a challenge, and is an extremely strong test of the subtle details of an AMR code. Miniscule errors that were previously unknown become glaring errors when the divergence goes from 1×10^{-14} to 1×10^{-6} in a single time step. This can be caused by an error in the other data as small as 1×10^{-8} that is, in any realistic simulation, insignificant and expected. This brings us to several modifications that needed to be made to Enzo before this work could be produced. Data consistency is the common thread in all the modified subsystems. None of these modifications have shown to make any significant impact on other works done with Enzo. While these modifications are of interest primarily to the Enzo developer, it is important to have them documented here.

3.8.1 Gravity Mod

Enzo's gravity solver returns an acceleration field that is given to the patch solver. The patch solver then adds the acceleration to the velocity and energy in the appropriate manner. See section 2.1.8 for more details. Since the Poisson problem is solved on each grid patch independently, it was found that the accelerations in the ghost zone of a given grid were often different than the active zones in the grid they neighbored. This difference was frequently not more than 1 part in 10^6, but

would quickly and efficiently ramp $\nabla \cdot \mathbf{B}$ from it's machine noise value of 1×10^{-14} to much larger values. This comes from the fact that slightly different values of the velocity would be entering the Riemann problem in the ghost zones, and would yield slightly different results for the electric field on the boundary of the grid. This destroys the underpinnings of why CT keeps $\nabla \cdot \mathbf{B} = 0$.

To fix this, EnzoMHD installs an additional boundary condition call on the acceleration field. While this is a bandage on the underlying problem, it allows MHD simulations to be run without the quality of the solution being compromised.

3.8.2 SibSUB mod and Boundary Correction

The hierarchy structure used in Enzo is a strictly nested one, in which subgrids belong to exactly one parent. The flux correction step was done in a loop over children of a given parent. However, no treatment was done on grids that shared a boundary with a fine grid that wasn't its own child. Such a situation can arise when two coarse grids share a face, and one coarse grid has a child along that same face. If the other parent has no child along that same face, the flux correction was not performed in those zones. This is an extremely rare occurrence, as a fine grid on one coarse boundary usually is tracking a physical structure that spans both coarse grids, in which case the 'other' coarse grid also has a child grid to project its solution into the parent. However, as mentioned in 2.1.3, *any* discrepancy in flow will lead to divergence in the field, so this was corrected.

The correction is a fairly brute force one. For each grid on a given level, it first scans for neighbors on that level that share a face. It then looks for subgrids of those grids that also share a face. This list is then passed along to the flux correction routine, which had to have its logic expanded to take care of the additional work. It has been noted that this correction does not work with the Fast Sibling locator. This will be rectified in the future.

3.8.3 Boundary Conditions

Initially, Enzo had no boundary condition call between the routines that update a coarse grid from a fine one and the rebuilding of the hierarchy. This also lead to discrepancies, as parent grids with subgrids along their boundaries inevitably use the ghost zones for interpolation. If the active zones that those ghost zones coincided with were updated from their own fine grids, that change needs to be the ghost zones, or discrepancies will occur between the subgrids that share that face, again causing divergence.

3.8.4 Cosmology and Flux Correction

In its initial formulation, Enzo did not take into account the time variability of the cell width due to the expansion during the fine grid subcycle when saving fluxes for the flux correction routine. This again lead to conservation loss and discrepancies, since the flux that was used to correct the parent grid used the cell width at the time of correction, neglecting any change during the subcycle integration. This was corrected. See sections 2.3.1 and 2.3 for more details.

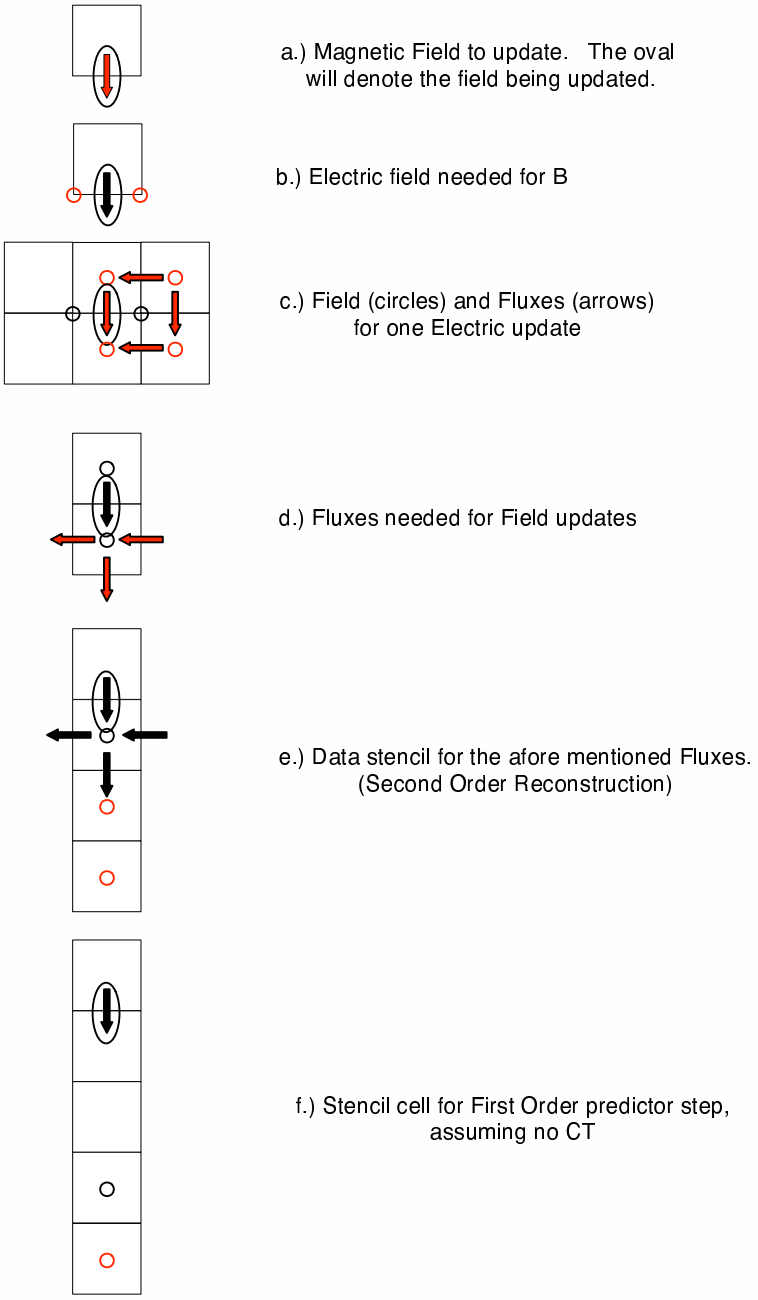

Figure 3.2: The complete stencil for 2^{nd} order time step integration, where the first (predictor) step has no CT and piecewise constant reconstruction, and the second (corrector) step uses CT and piecewise linear reconstruction.

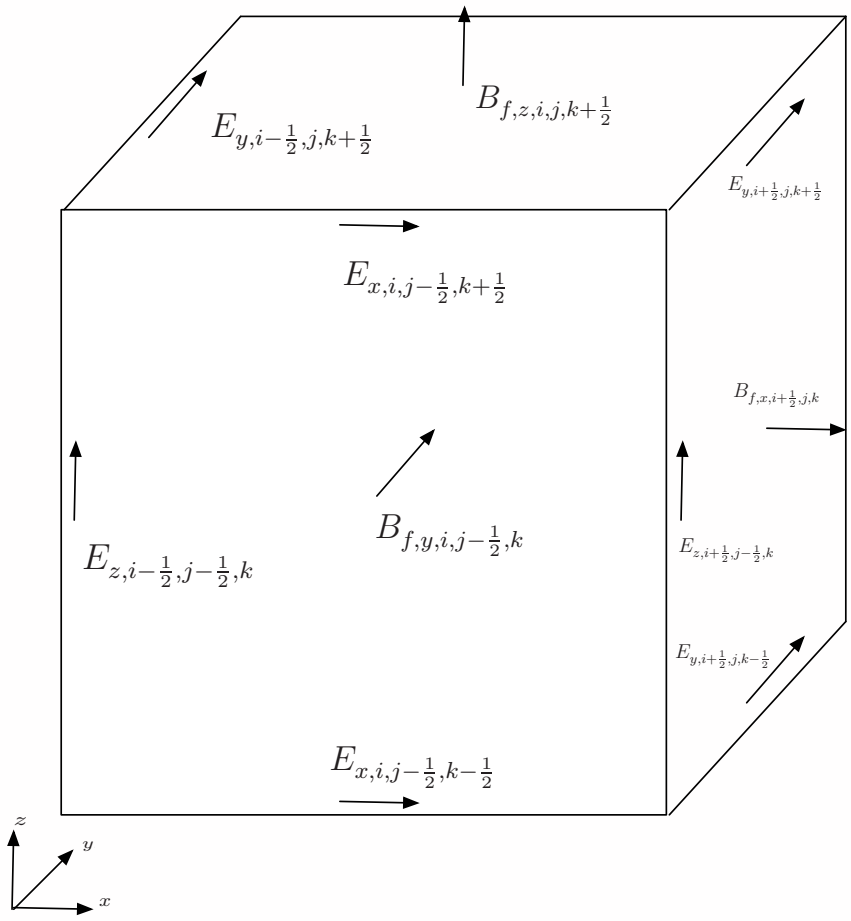

Figure 3.3: The data structure for the electric field **E** and face centered magnetic field $\mathbf{B_f}$

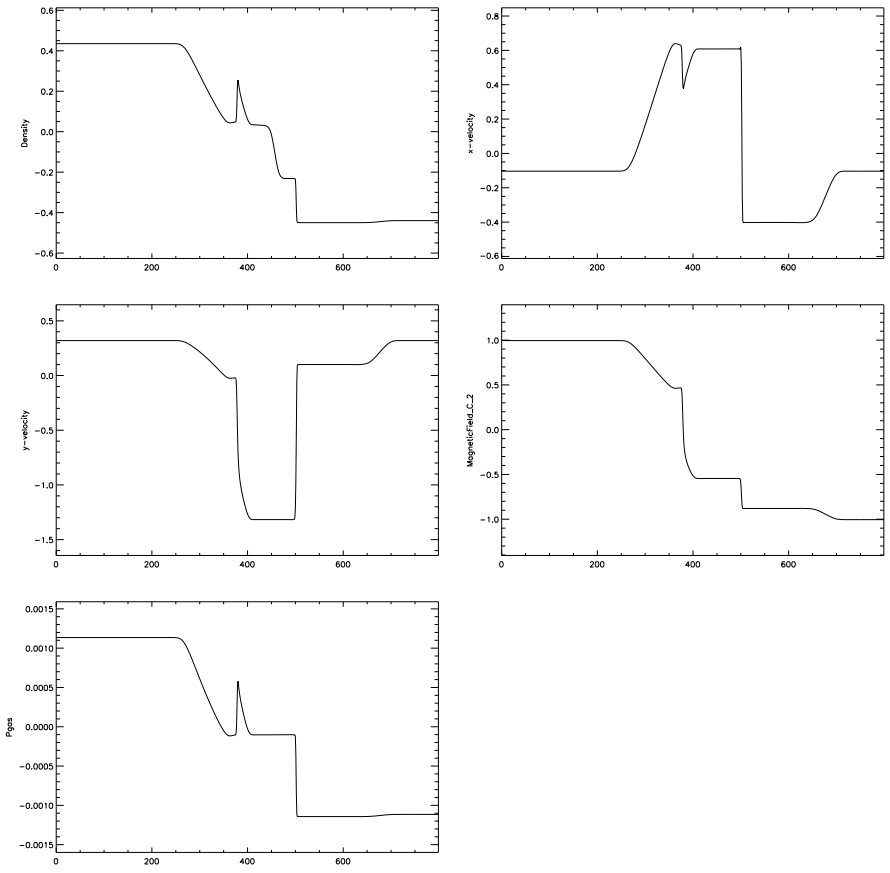

Figure 3.4: Piecewise Constant reconstruction for the Brio-Wu shock tube.

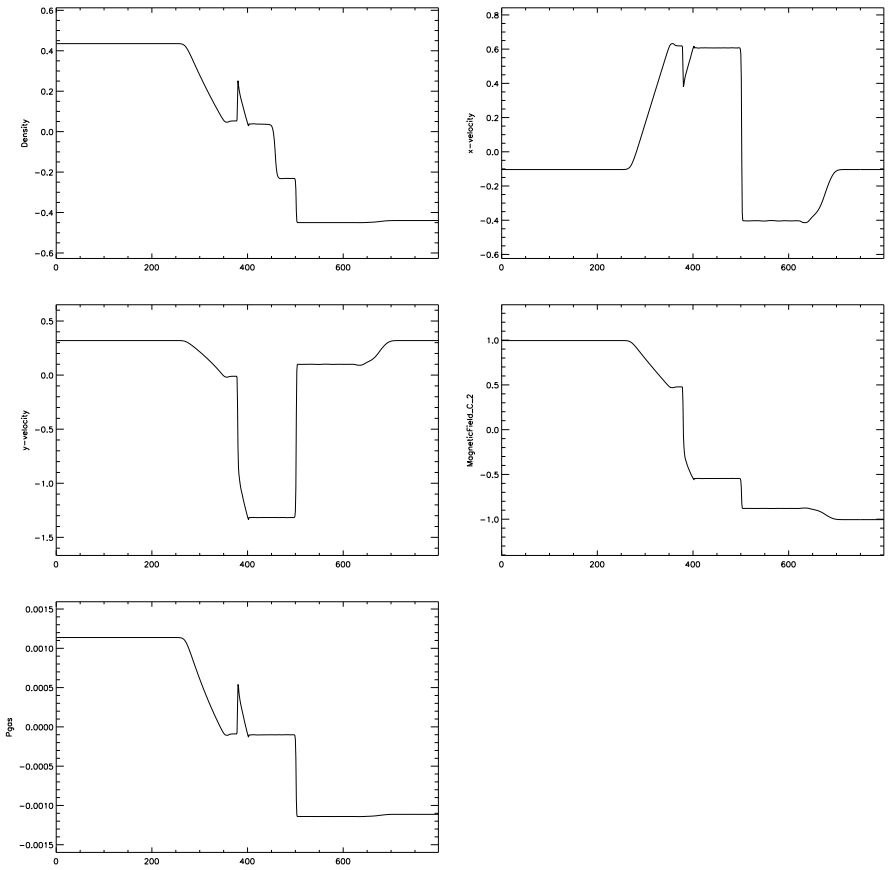

Figure 3.5: Brio-Wu shock tube with minmod slope limiter on the correct step for all fields, using primitive variables (pressure and velocity)

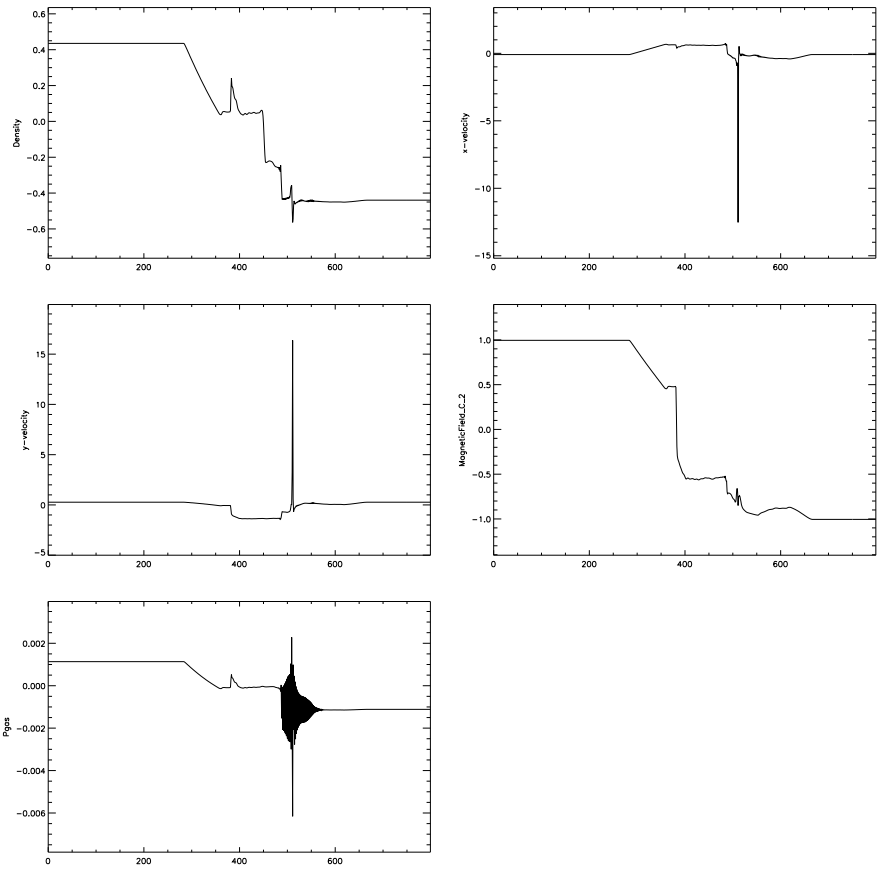

Figure 3.6: The Brio-Wu Shock Tube with vanLeer limiter on the conserved quantities. Note the sever numerical oscillations between the slow shock and fast rarefaction.

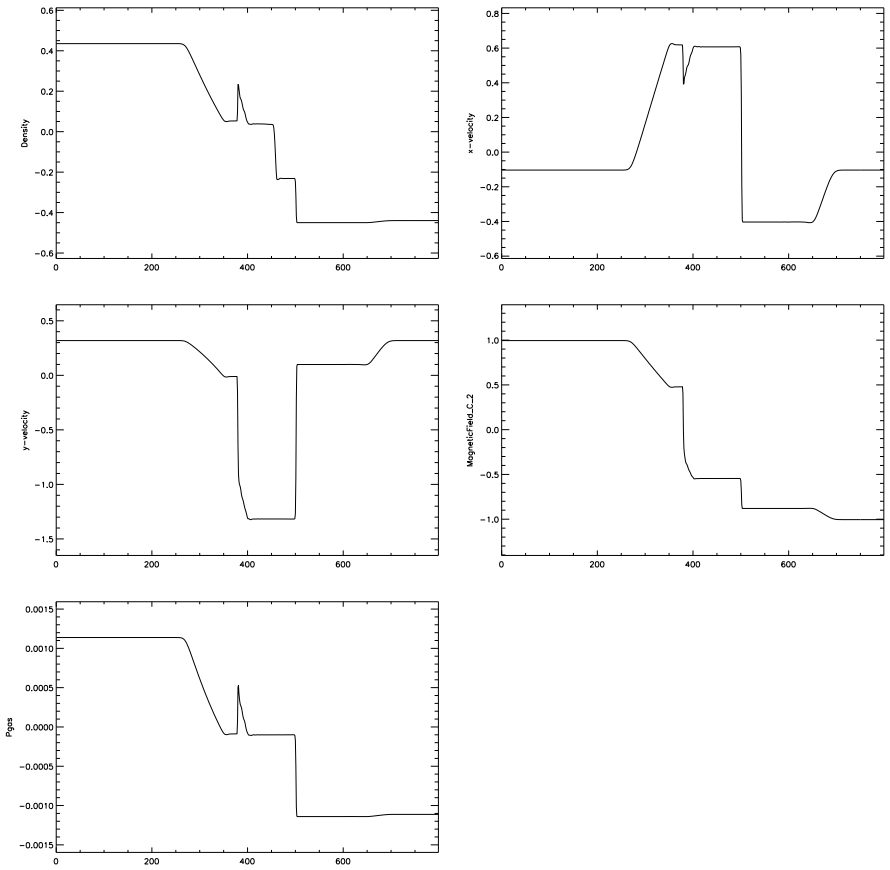

Figure 3.7: The Brio-Wu shock tube with the "recommended" set, using vanLeer on density and magnetic field, and minmod on velocity and total energy.

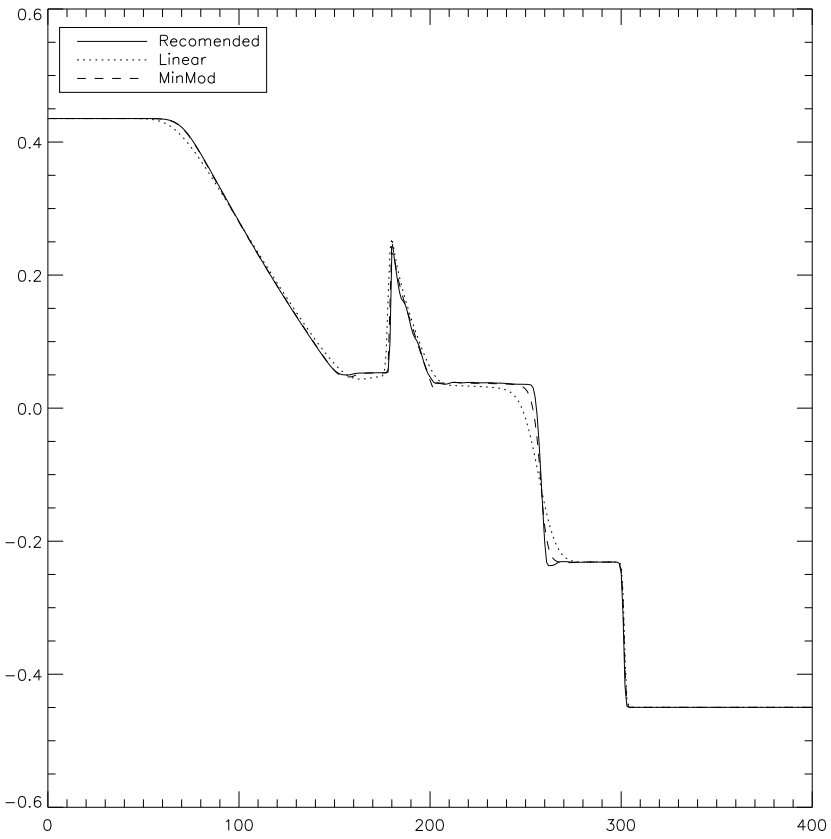

Figure 3.8: Density from the Brio-Wu shock tube showing the "recommended" set of switches (solid line), a single piecewise linear reconstruction (dotted) and the minmod slope limiter on all fields.

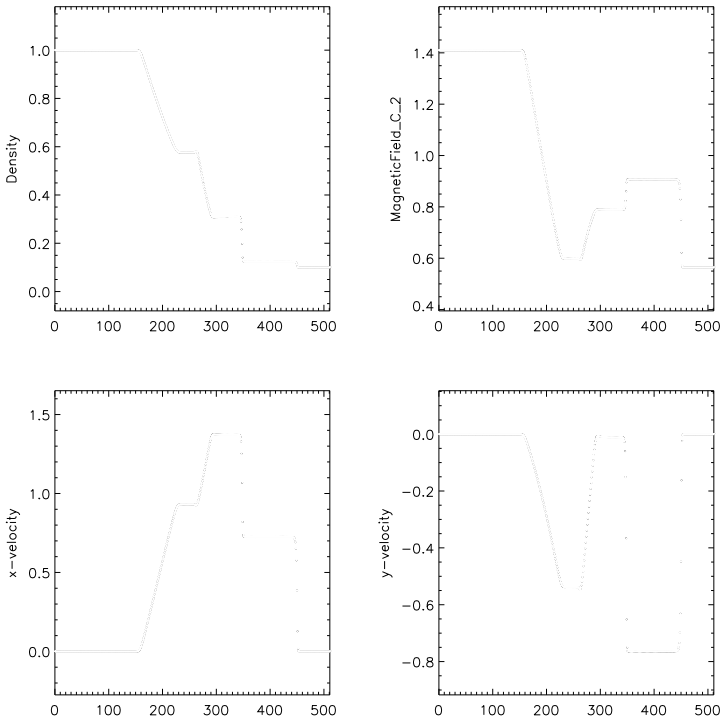

Figure 3.9: The Kim Isothermal Test using the “recommended” set of switches.

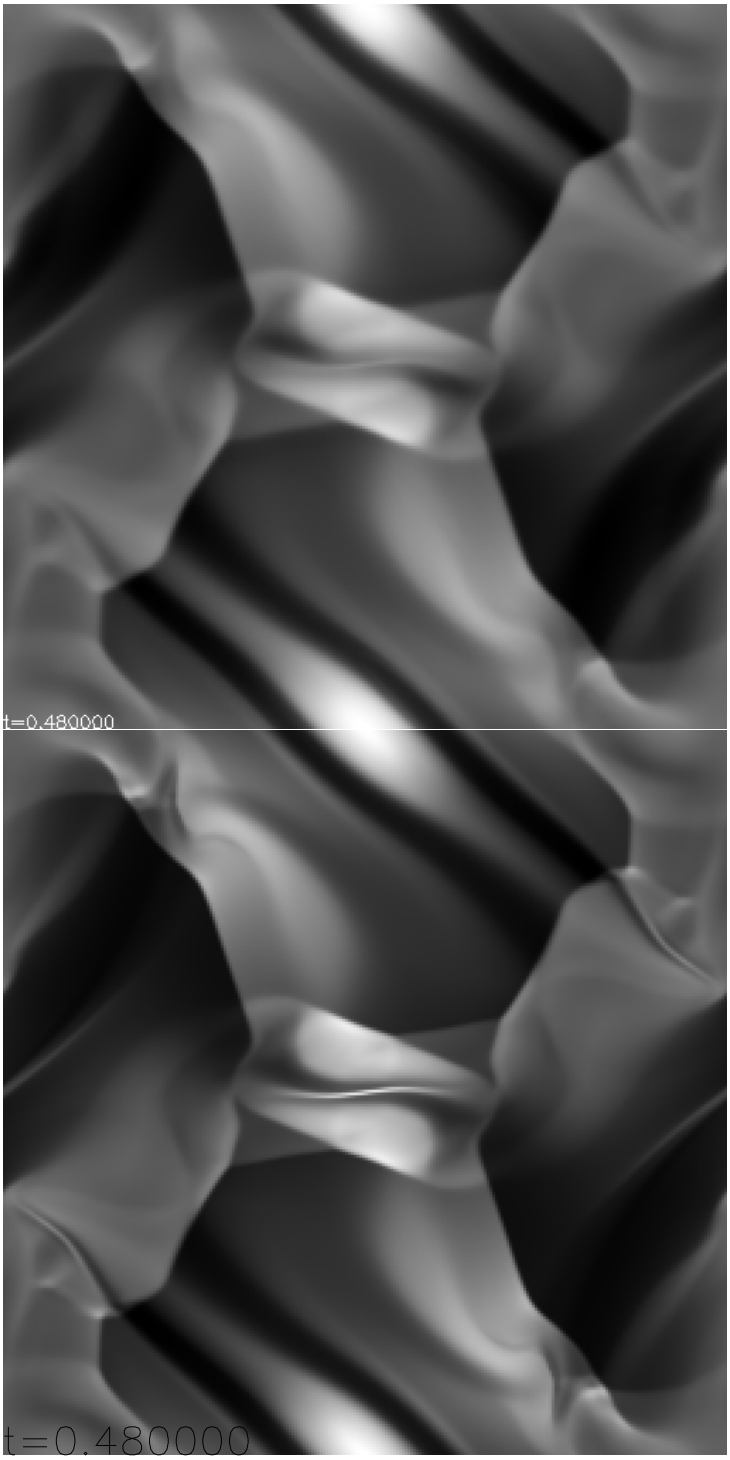

Figure 3.10: The Orszag Tang vortex problem for both the Ryu and Jones (top) and DaveThena method (bottom) This shows the significant decrease in numerical diffusion in the second method.

and $A_0 = 10^{-3}, R = 0.3, r = \sqrt{x^2 + y^2}$. This is then advected back to its starting point. The results from this test can be seen in figure 3.11. The top panel shows a single integration step with piecewise constant reconstruction and the Balsara Spicer CT method. For reasons that are lost to a beer haze several years old, this run was done with $v_y = 0$. The bottom panel shows a result from a run with piecewise constant reconstruction for the predict step and piecewise linear for the correct, wind-switched Athena CT, and is quite similar to the result in (Gardiner & Stone, 2005). It is claimed that omitting the higher order terms that make the Athena CT different from the Balsara-Spicer CT cause the loop to disintegrate, but this is not seen here. However, the result shown here is terrible.

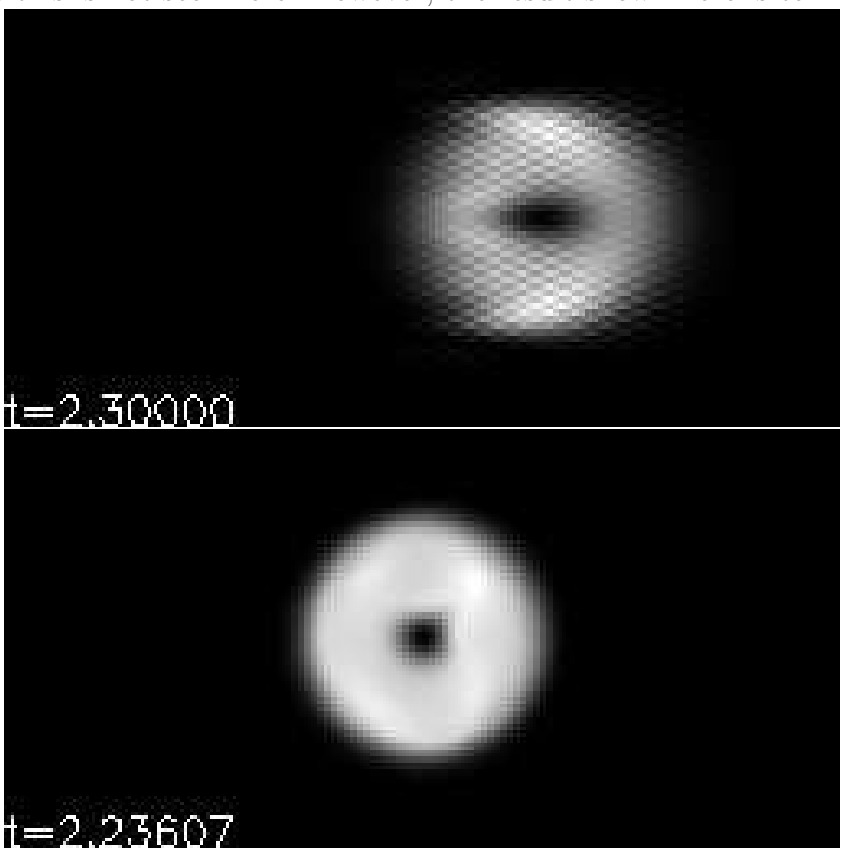

Figure 3.11: The magnetic energy from the magnetic loop advection test of Gardiner & Stone (2005), done poorly (top panel) and properly (bottom panel). The top panel uses a single integration step and the Balsara-Spicer CT method, the bottom uses piecewise constant reconstruction for the predict step and piecewise linear for the correct, wind-switched Athena CT

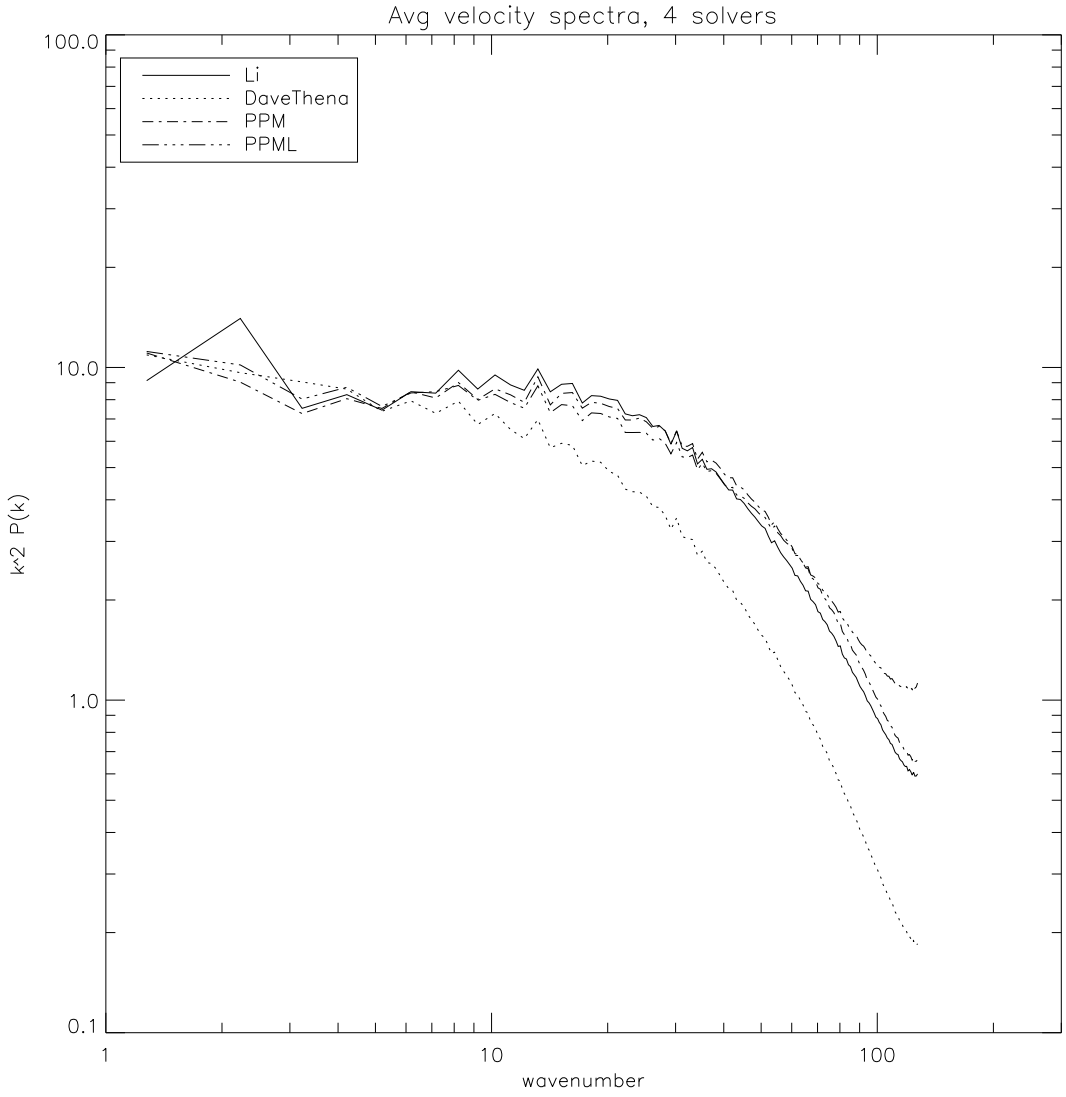

Figure 3.12: The compensated velocity power spectrum for 4 solvers on Mach 5 unmagnetized turbulence.

Figure 3.13: A demonstration of an instability that is believed to be caused by improper reconstruction of the electric field in an unsplit method. Both panels show density in driven turbulence at Mach 3. The left panel has no magnetic field, the panel at right has $B = [0, 0, \sqrt{2}]$. The spike in the right is an unavoidable explosion.

Chapter 4

Star Formation

4.1 Numerical Experiments

4.1.1 Suite of runs

Simulations performed for this work are initialized in a manner similar to those in sections 2.2.1 and 3.1.2. The cubic domain is initially uniform in density with an initial plasma $\beta = 8\pi p/(B^2) = 22$. A divergence free, Gaussian, random velocity field with power only at the large scale ($1 <= k <= 2$) is added to the velocity field at each time step in such a way that that energy input $\dot{E}$ is constant (Mac Low, 1999). Driving is maintained for several dynamical times $\tau_{dyn} = L_{box}/v_{rms}$ to statistically decouple the initial conditions from the field that we wish to measure. This initial driving is done without gravity. This initial cube is identical to the cube used for the Santa Barbara Turbulence comparison project (Kritsuk, 2009), currently under way. At $t = 0$, gravity is switched on. For some runs presented in this work the driving is continued after $t = 0$, others it is stopped and the turbulence is allowed to decay.

A series of ten simulations were done using the Kraken Cray XT4 at the National Institute for Computational Science. Each of these simulations had a root grid of 128^3; nine of these used 4 levels of refinement, one used 6. This gives an effective resolution of 2048^3 for the 4 level runs, and 8192^3 for the 6 level run. Refinement was triggered by the Truelove condition (Truelove et al., 1997). If at

any point in time the local Jeans length

$$\lambda_J = \sqrt{\pi c_s^2 / G\rho} \tag{4.1}$$

was shorter than 4 zones, the area was refined. This defines the Truelove density

$$\rho_T = \frac{pic_s^2}{G(4\Delta x)^2} \tag{4.2}$$

where Δx is resolution on a given level. Zones in which $\rho > \rho_T$ are flagged for refinement.

For the finest level, some fraction of zones will eventually violate the Truelove condition. Cores discussed in this work will frequently have the fraction of their mass that has violated this condition indicated. This will be denoted M_V/M. This serves as an indicator of the level of collapse the core has experienced.

Four of these runs allowed the turbulence to decay after the gravity was switched on, the rest continued the driving.

The primary parameter change among the runs was the virial parameter, α_{vir}. The virial parameter gives a ratio of the kinetic energy (ke) to the gravitational energy (ge): $\alpha = |2ke/ge|$. A sphere with $\alpha = 1$ is in virial equilibrium, while $\alpha > 1$ is understood to be unbound. Typically, the value for a uniform sphere is used;

$$\alpha_{sphere} = \frac{5\sigma_{1d}^2 R}{GM} \tag{4.3}$$

where $\sigma_{1d} = \sigma_{3d}/\sqrt{3}$ is the velocity dispersion, R is the object radius, G is the gravitational constant, and M is the total mass in the box (Bertoldi & McKee, 1992). However, since our box is a cube, we instead use the gravitational potential energy for a cube:

$$\alpha_{vir} = \frac{18\sigma_{1d}^2 R}{\pi GM} \tag{4.4}$$

This yields a slight discrepancy with the quoted value of α_{vir} for other simulators, as the increased gravitational energy of a cube decreases α_{vir}. This lowers the quoted value for α_{vir} as compared with other simulations.

The simulation values of density, sound speed (thus pressure), and box length are set to unity. In the simulation, different values of α_{vir} are obtained by

altering the value of the gravitational constant G_{code}. In the analysis, simulations are all normalized to a size of 10 pc and a sound speed of $0.2kms^{-1}$, the sound speed for gas at $10K$. The value of the mean density is changed proportional to the gravitational constant such that $G \propto \rho t^2$. However, since G only constrains one of the free dimensional parameters, we are free to re-scale units with the following conditions:

$$L \propto T^{1/2}\rho^{-1/2} \tag{4.5}$$

$$M \propto T^{3/2}\rho^{-1/2} \tag{4.6}$$

$$c_s \propto T^{1/2} \tag{4.7}$$

$$t_{ff} \propto n^{-1/2}. \tag{4.8}$$

Table 4.1 shows the range of parameters. The first column shows the value of α_{vir}; the second column indicates whether the driving was continued after $t = 0$, or if it was allowed to decay; the third column indicates whether or not driving was continued past $t = 0$. The last column gives the name of the simulation. The name relates to the labels put on the simulations as they were run in the order they were performed, and serve only as a reference to the archived data.

Most of the analysis will be done on the $\alpha_{vir} = 0.52$ run. This is equivalent to $\alpha_{vir} \approx 1$ for the spherical definition. Four of these simulations ($ok5$, $ok6$, $ok7$ and $ok10$) will be ignored entirely in this analysis due to time constraints, and appear on this table only for reference to the archived data.

4.1.2 Core Selection and Images

We used the `yt` analysis package ((Turk, 2008)) for most of the data analysis presented here. `yt` is a highly extensible tool designed to visualize and analyze AMR datasets, written in the Python programming language. Cores were selected using `yt`'s Clump module. Clump and its *find_clumps* tool finds connected sets of zones with nearest neighbors having values of density ρ_i and $\rho_{i+1} = \delta\rho_i$ for levels spanning some minimum density ρ_0 through the maximum found in the dataset. This technique is similar to CLUMPFIND (Williams et al., 1994). For our analysis, we set $\rho_0 = 10\times < \rho >$ to be 10 time the mean, and with levels spaced every 12%

Table 4.1: Parameters for the suite of simulations done for this study.

α_{vir}	Driven	N Levels	Name
0.52	Y	4	$ok04$
0.91	Y	4	$ok03$
1.3	Y	4	$ok02$
1.6	Y	4	$ok09$
2.3	Y	4	$ok06$
3.1	Y	4	$ok07$
1.3	N	4	$ok01$
1.3	N	6	$ok08$
0.52	N	4	$ok05$
5.1	N	4	$ok10$

above the previous level ($\delta = 1.12$). We define a "core" as any object returned from $find\_clumps$ that a.) does not have more than one child and b.) who's parent does have more than one child. This technique is common in in both observational studies (Johnstone et al., 2000)) and numerical studies (Lunttila et al., 2008). In figure 4.1 we indicate a schematic of this process: the grey circles indicate clumps that will be defined as cores

It has been argued by Rosolowsky et al. (2008) that selecting objects in this fashion makes the object population too sensitive to the details of the minimum density and level spacing. This will be taken into account in future work.

A representative selection of cores from the $\alpha_{vir} = 0.52$ run at $t = 0.75t_{ff}$ can be seen in figure 4.2. This selection gives an overview of the different types of objects that can be considered cores. The object on the bottom right also shows a potential defect with clumpfind type algorithms, as one can clearly see that a slightly different selection of ρ_0 and δ could potentially bifurcate this into two objects.

Section 4.3 shows a close up of a selection of cores. This shows how clustered the objects are in the simulation, and how the filamentary nature of the turbulence is preserved in the core arrangement. This has been seen in nature in a number of observations, such as Motte et al. (1998) in Ophiuchus.

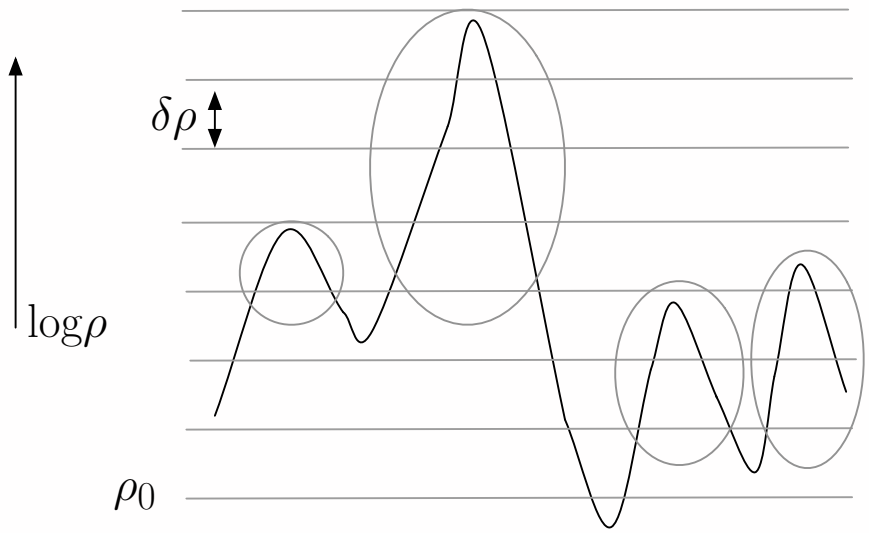

Figure 4.1: A schematic of clump selection. Lines indicate levels of constant density. Connected sets at constant density are selected, and isolated objects are selected as cores. Circles indicate objects that would be selected as cores in this schematic

4.2 Mass vs Size

We first show the mass and size of cores in order to get a preliminary picture of what we will be examining. Figure 4.4 shows core mass M vs size S in zones for cores in 4 snapshots in our primary run, the $\alpha_{vir} = 0.52$ driven simulation. Cores in this plot were selected to have $\alpha < 2.0$, which is an indicator of boundedness, though neither necessary nor sufficient one, as discussed in section 4.4. S is defined as the radius R in pc divided by the smallest zone width in the dataset, also in pc. R is defined as half of the geometric mean of the width of the core along each of the coordinate axes Δx, Δy, Δz:

$$R = (\Delta x \times \Delta y \times \Delta z)^{1/3}/2. \tag{4.9}$$

$$S = R/dx \tag{4.10}$$

For spherical objects this is identically the radius. Times are $0.208t_{ff}, 0.388t_{ff}, 0.468t_{ff}$, and $0.743t_{ff}$. The color of each point represents the fraction of mass above the Truelove density. This is an indicator of how collapsed each core is. "Red" cores

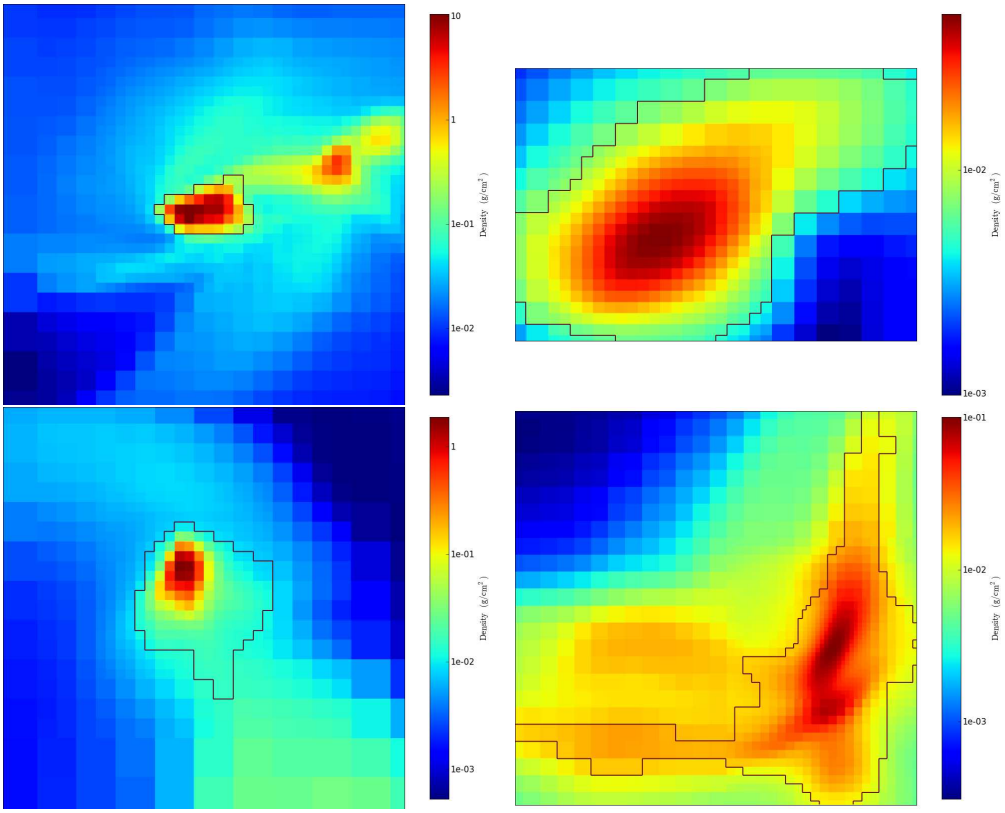

Figure 4.2: A representative selection of cores from the $\alpha_{vir} = 0.52$ run at $t = 0.75t_{ff}$. This selection gives an overview of the different types of objects that can be considered cores by the the algorithm defined in section 4.1.2. The width of each plot is $0.2pc$

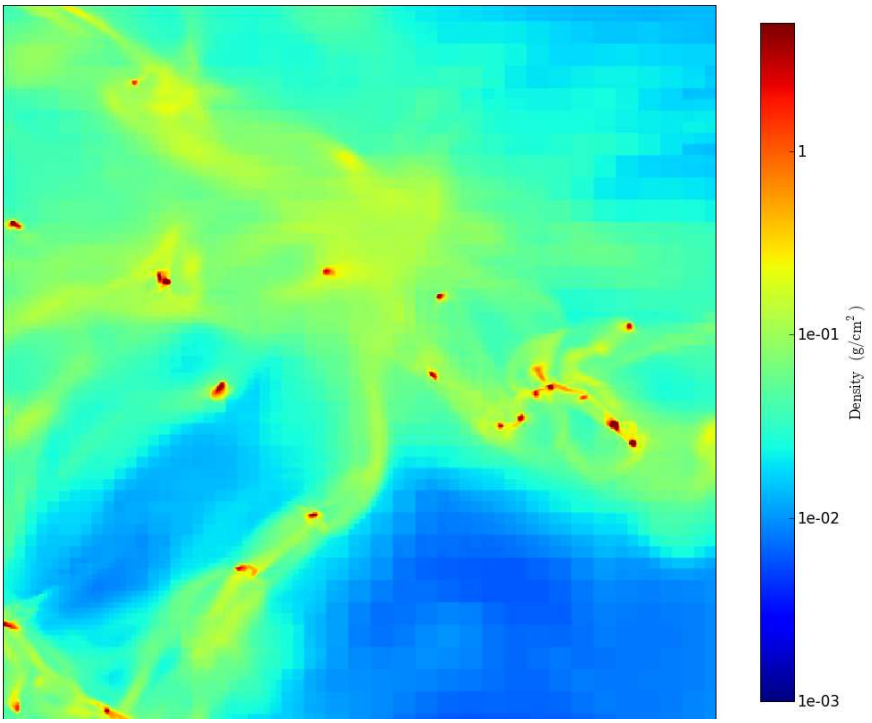

Figure 4.3: A close up of a selection of cores. Image is 2.5pc on a side.

have completely violated the Truelove condition and are entirely at the finest resolution. As time progresses, these cores get smaller and smaller, until they occupy only a few zones. Even at early times, though, "Red" cores can be seen at all masses up to a few hundred solar masses and a few hundred zones. We will be using the Truelove density as an indicator of collapse in cores. We believe that cores with with high fraction above Truelove are in general quite bound and remain so, though this will need to be investigated in the future.

While Truelove et al. (1997) saw artificial fragmentation for their spherical collapse. However, we believe that the size of these objects is not due to artificial fragmentation. As will be discussed in section 4.5, increasing the resolution in fact increases the number of cores, while artificial fragmentation from lack of resolution would tend to decrease it.

Also plotted are fits to $M = S^{\gamma}$. Kritsuk et al. (2007) measured a similar quantity for boxes in their turbulent hydrodynamic runs, and found that $\gamma = 2.0$ for small boxes (less than 30 zones) and $\gamma = 2.4$ for larger boxes. In our case of self gravitating MHD turbulence, we find much shallower fits that decreases with time. Fit exponents are, as time progresses, $1.65, 1.40, 1.00, 0.95$. This suggests that objects are in transition from the somewhat larger than 2 dimensional structures generated in the turbulence to much more filamentary structures.

4.3 Density PDF

One of the most prominent consequences of turbulence in molecular clouds is the log-normal distribution of densities (Vazquez-Semadeni, 1994; Padoan et al., 1997a,b; Scalo et al., 1998; Passot & Vázquez-Semadeni, 1998; Nordlund & Padoan, 1999; Klessen, 2000; Padoan & Nordlund, 2002). This has been used to predict both the Initial Mass Function of stars (IMF) (Padoan & Nordlund, 2002; Padoan et al., 2007), brown dwarf frequency (Padoan & Nordlund, 2004) and the star formation rate (Krumholz & McKee, 2005). The IMF and star formation rate will be discussed further in sections 4.8 and 4.9 respectively. Here we will discuss the PDFs one expects to see from isothermal turbulence, and what has been seen in

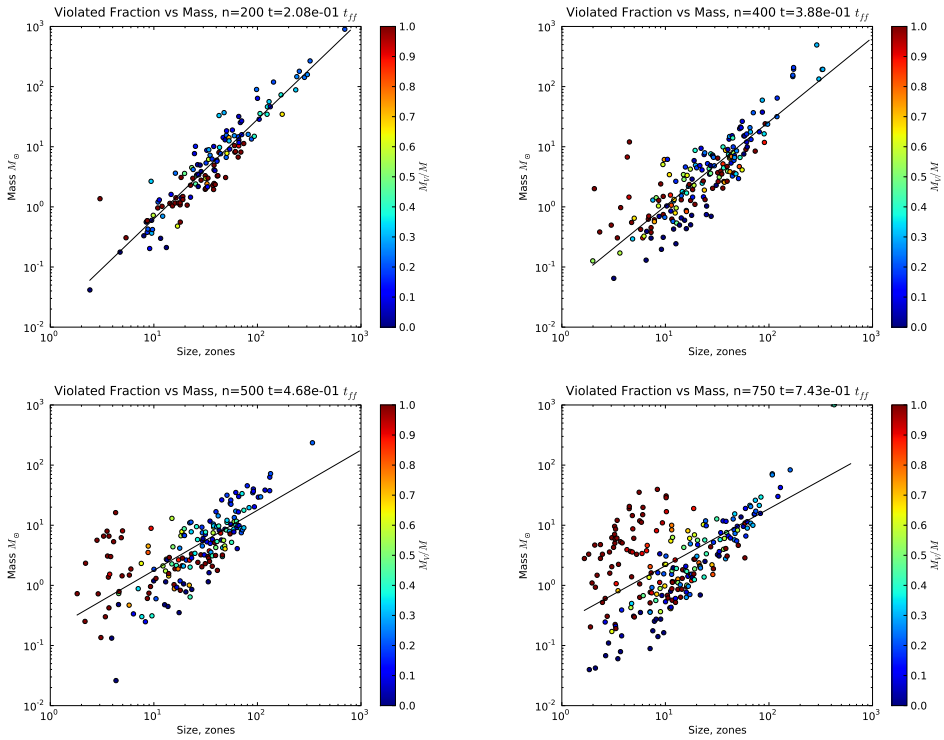

Figure 4.4: Mass vs. Size for 4 timesteps in the $\alpha_{vir} = 0.52$ driven run. Color indicates fraction of mass above the Truelove density. Size is in zones on the finest level. Times and fits to the $M = S^\gamma$ power law are $(0.208t_{ff}, 1.65)$, $(0.388t_{ff}, 1.40)$, $(0.468t_{ff}, 1.00)$ and $(0.743t_{ff}, 0.95)$. For reference, 1 zone is 4.8×10^{-3} pc, and 1000 zones is 4.8 pc.

our simulations.

The central limit theorem states that the sum of a sufficiently large number of uncorrelated events will form a Normal, or Gaussian, distribution. The corollary of this is a sufficiently large number of random *multiplicative* events will form a lognormal distribution. This distribution has been experimentally verified in a large number of different simulations, both pure hydro (Vazquez-Semadeni, 1994; Padoan et al., 1997c) and MHD (Li et al., 2004; Lemaster & Stone, 2008)

The log-normal distribution is given by

$$P(x)d\ln x = \frac{1}{\sqrt{2\pi\sigma^2}}\ exp\left[\frac{(\ln x - \mu)^2}{2\sigma^2}\right] dx \tag{4.11}$$

where $x = \rho/\rho_0$, is the over density, and $|\mu| = \sigma^2/2$ is the mean of $\ln x$. For pure hydrodynamical turbulence,

$$\sigma = \sqrt{\ln(1+\gamma^2\mathcal{M}^2)} \approx \gamma\mathcal{M} \tag{4.12}$$

where $\gamma \approx 0.5$ has been determined from numerical experiment. For driven MHD turbulence, Lemaster & Stone (2008) find that

$$\sigma = \sqrt{|-0.72\ln\left[1+0.5\mathcal{M}^2\right]+0.20|} \tag{4.13}$$

When turbulence simulations are performed in the presence of self gravity, several authors (Klessen, 2000; Slyz et al., 2005; Vázquez-Semadeni et al., 2008) find that the log-normal PDF underestimates the high density tail of the measured PDF. Two of these can be seen in figure 4.5. Slyz et al. (2005) fit the high density tail to a power law with index of -1.5. Klessen (2000) does not show a power law, but his simulations are poorly resolved, and Vázquez-Semadeni et al. (2008) only mention the power law in passing. Our work is the first reported case in an MHD simulation.

Figure 4.6 shows snapshots of the density PDF for our fiducial run at $t = 0$ and at $t = 0.75t_{ff}$, with fits to log normals. Fit parameters are in table 4.3. The shifts in μ and σ as the gas collapses are not surprising, as the mean shifts to lower density and the breadth becomes somewhat broader. The shift to lower density comes because this is a volume weighted density; more mass at high density implies

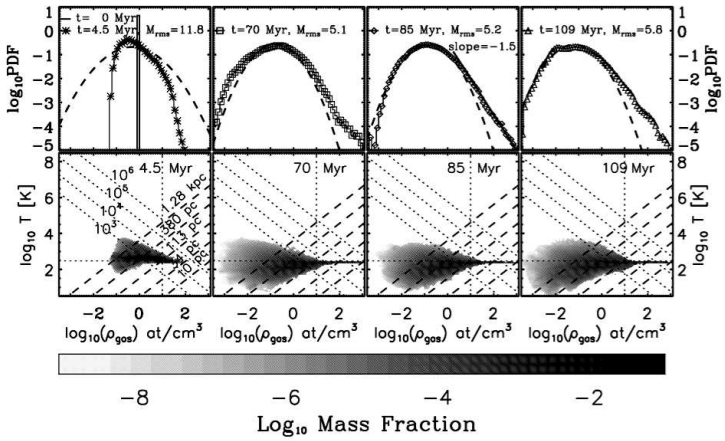

Figure 11. Time evolution of the density PDF (top row) and phase diagrams (bottom row) for run B2 (128^3 run with star formation and self-gravity but no feedback). The thick dashed line overplotted on the measured PDFs (symbols) is the log-normal PDF predicted by Padoan et al. (1997). The solid line with a slope of -1.5 plotted at $t = 85$ Myr is a fit to the high-density end of the PDF. In the phase diagrams, the dotted vertical (horizontal) line marks the critical density, $\rho_{\rm crit}$ (temperature, $T_{\rm crit}$), for star formation. Dotted diagonal lines mark lines of constant pressure, and are labelled for the $t = 0$ Myr frame: $P = 10^6$, 10^5, 10^4 and 10^3 $k_{\rm B}$ cm^{-3} K.

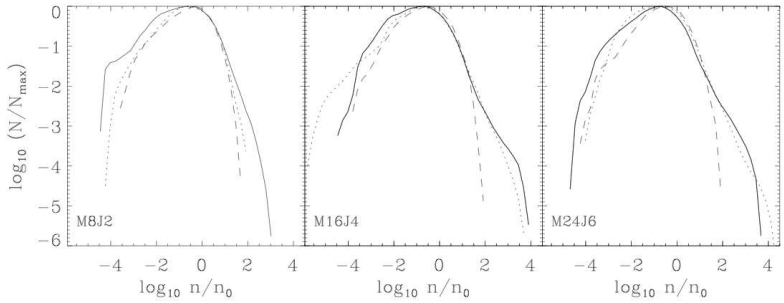

Figure 3. Probability density function (PDF) of the density field in the three runs at times $t = 0$ $t_{\rm ff}$ (*dashed line*), 1 $t_{\rm ff}$ (*dotted line*), and 3 $t_{\rm ff}$ (*solid line*) after gravity was turned on, where $t_{\rm ff}$ is the global free-fall time of each simulation (cf. Table 2). The vertical axis is normalized to the number of grid cells at the maximum, $N_{\rm max}$.

Figure 4.5: Top: Density PDF from the self gravitating simulation of Slyz et al. (2005). This set of simulations were not isothermal, but nearly so due to the rapid cooling. Bottom: The same, from Vázquez-Semadeni et al. (2008).

Table 4.2: Fit parameters.

t/t_{ff}	μ	σ	χ^2
0	-0.80	1.35	4.6×10^{-6}
0.75	-1.86	1.74	1.6×10^{-6}

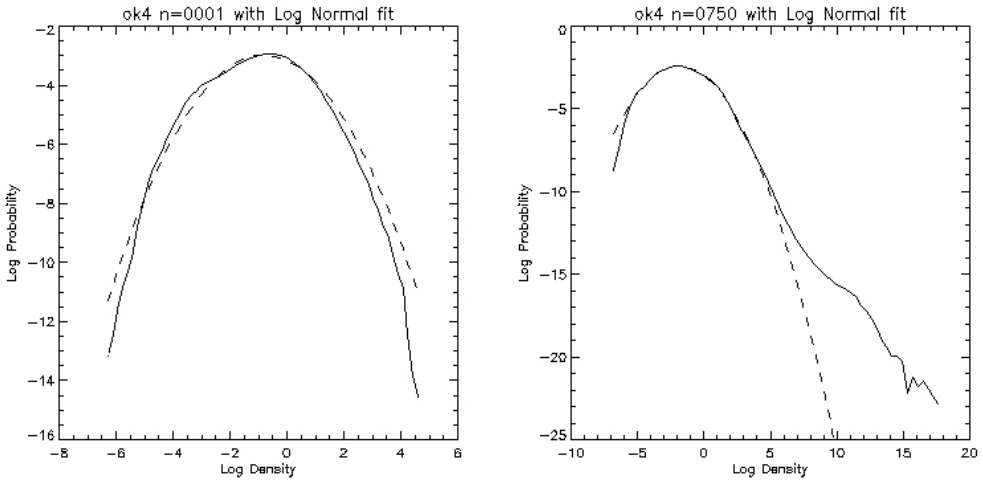

Figure 4.6: Density PDFs of the initial conditions (left) and after $t = 0.75t_{ff}$. (right) Both are fit to lognormal distributions.

lower overall volume average. The broadening of the fit reflects the fact that more mass is at higher densities at later times. It is interesting to note that the quality of the fit as measured by χ^2 actually improves by a factor of 4 in the gravitating case.

The right panel of Figure 4.7 shows an average of 10 timesteps for run *ok*4 between $t = 0.5\ t_{ff}$ and $t = 0.75\ t_{ff}$. This corresponds to star formation efficiencies of $SFE = 0.07$ and $SFE = 0.15$. In this range, all simulations have roughly constant star formation rate. We will use this range to compare star formation rates with different values of α_{vir}. This is discussed further in section 4.9. Also plotted is a power law fit between $\rho/\rho_0 = 10, 1000$. The fit exponent is -1.6, similar to the value -1.5 seen by Slyz et al. (2005). The left panel shows each timestep over plotted individually. The power law is remarkably stable over both time and, consequently, violation fraction. Also shown in the left plot are the Truelove density discussed in section 4.1 and the critical density discussed in

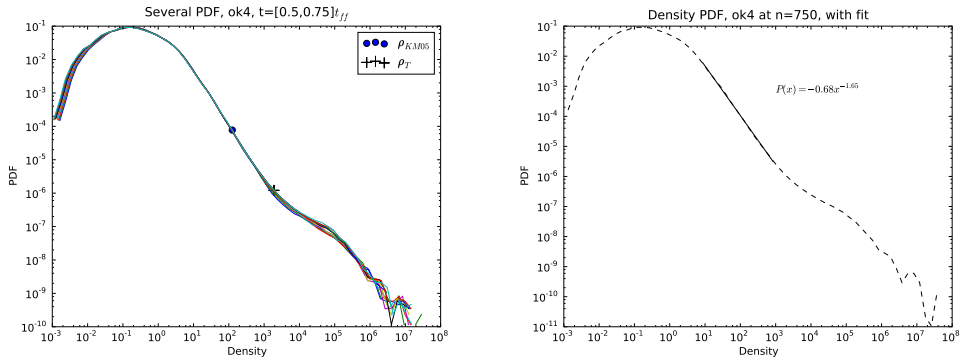

Figure 4.7: PDF of 10 steps between $t = 0.5t_{ff}$ and $t = 0.75t_{ff}$ of the $\alpha = 0.52$ (ok4) run. Left: All steps over plotted. Right averaged and fit with a power law $P(x) = -0.68x^{-1.65}$ between $\rho/\rho_0 = 10, 1000$. The powerlaw is stable over time. Also shown in the left plot are the Truelove Density and the critical density of Krumholz & McKee (2005) discussed in section 4.9

section 4.9.

Figure 4.8 shows the robustness of the power law against virial parameter α_{vir}. Plotted are PDFs for each of the 4 driven runs with $\alpha_{vir} < 2$. These plots are averaged over times corresponding to star formation efficiencies between $SFR = 0.07$ and $SFR = 0.15$, as in the previous run. This serves to normalize each run to the same physical conditions.

Figure 4.9 shows the PDF for 3 runs with $\alpha_{vir} = 1.3$; a driven (green) and decaying (blue) run with 4 levels of resolution, and a decaying run with 6 levels (red). More will be said about this later in section 4.5, here we will simply note that the power law slope is additionally not a function of Mach number, as the runs marked "undriven" have $\mathcal{M} = 5.5$ at this time, nor resolution, as one of the graphs has 6 levels.

4.4 α_{vir} vs Energy Ratios

The parameter α_{sphere} (eqn. 4.3) is the typical parameter used in the literature to indicate whether or not an object is collapsing. We would like to address the validity of using this as an indicator of whether or not a core or other clump

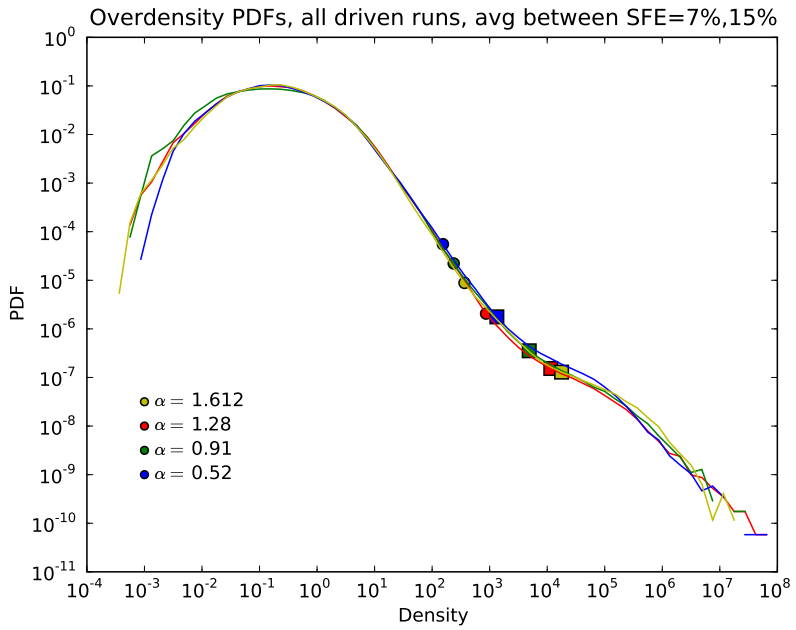

Figure 4.8: Density PDF for multiple values of α_{vir}. The squares show the Truelove density and circles show the critical density of Krumholz & McKee (2005) (see section 4.9

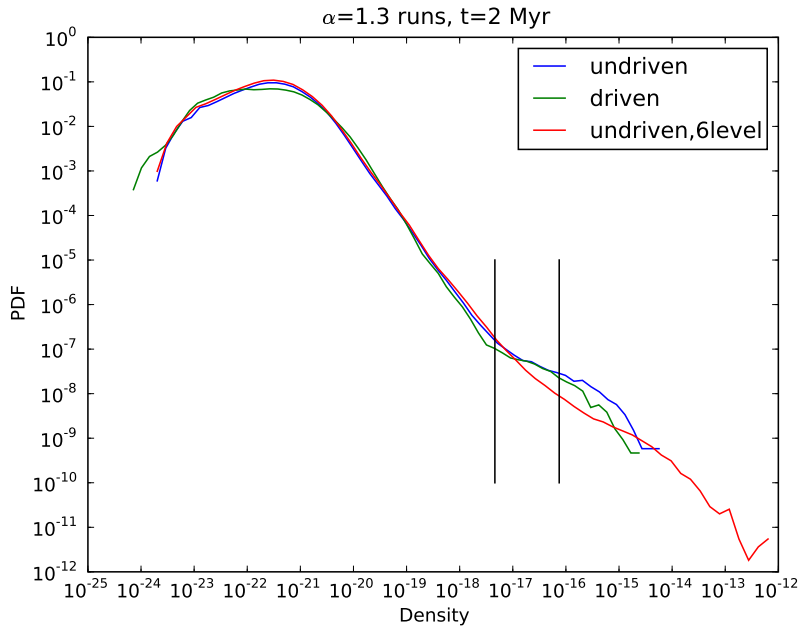

Figure 4.9: Density PDF for three runs with $\alpha_{vir} = 1.3$: driven with 4 levels of refinement (green), decaying with 4 levels of refinement (blue) and decaying with 6 levels of refinement

of gas is collapsing by comparing

The derivation of $\alpha_{sphere} = 5\sigma^2 R/GM$ comes from a simplification of the Virial Theorem, which states that for any clump of gas

$$\frac{1}{2}\ddot{I} = 2(\mathcal{T} - \mathcal{T}_s) + \mathcal{B} + \mathcal{W} \tag{4.14}$$

where I is proportional to the inertia tensor; $\mathcal{T}$ is the kinetic energy and thermal energy in the clump; $\mathcal{T}_s$ is the surface pressure; $\mathcal{B}$ is the magnetic term, which contains both isotropic pressure and curvature terms; and $\mathcal{W}$ is the gravitational energy. By ignoring surface and magnetic terms and assuming a sphere of constant density, one can define a term

$$\alpha_{sphere} \equiv -\frac{2\mathcal{T}}{\mathcal{W}} = \frac{5\sigma^2 R}{GM} \tag{4.15}$$

which, indirectly, indicates the sign of $\ddot{I}$ which is in turn treated as a tracer of expansion or collapse.

Since both simulated and observed cores are typically not spherical nor uniform in density, and also include magnetic fields, we thought it would be beneficial to examine how the estimated Virial ratio α compares to ratios of combinations of kinetic (ke), thermal (te), and magnetic (be) energies to gravitational energy (ge) in cores. Additionally, σ_{1d} (eqns. 4.3, 4.4) is sometimes computed in the computational literature using only the fluid velocity, neglecting the thermal component. However, the observational literature typically doesn't deconvolve contributions to the line width from velocity and thermal motions. We will not treat the validity of ignoring the surface term here. Both Dib et al. (2007) and Ballesteros-Paredes (2006) study that in detail.

In figure 4.10, we show six figures comparing both computations of α_{vir}, purely fluid velocity in the left column and fluid + thermal in the right. The top row shows α vs. $\mathcal{R}$ = ke/ge, the second is (te+ke)/ge, the third is (be+te+ke)/ge. Also plotted are lines at 0.2, 2.0, and 20.0. Additionally, as with most plots in this work, the color of each point shows the fraction of mass in the object above the Truelove density. Ideally, all points would cluster along the line $\alpha = 2ke/ge$.

In the top line, we treat only kinetic energy. The points here cluster basically around 2, with some outliers, most notably on population of collapsing objects

around $ke/ge = 0.3$ The left plot indicates that α_{vir} somewhat undershoots the expected, while the inclusion of the thermal energy in the definition of α_{vir} serves to shift the points up somewhat. The spread is not changed much.

The second row shows the inclusion of the thermal energy in the energy ratio. The left plot shows α_{vir} without the thermal component, and the spread is quite large. However, with the thermal component included, the spread narrows substantially. This shows that when ignoring magnetic effects, it's important to include the thermal energy in computation of α_{vir}, or one will substantially under estimate the value.

The third row shows compares α_{vir} to the full energy available to an object, which is usually ignored in both observations and numerical work. These plots show that α_{vir} computed for a uniform non-magnetized sphere is not a good indicator of gravitational boundedness.

Somewhat more telling is figure 4.11. This is the same plot as 4.10 with the plot range restricted to $\alpha < 10$ and $ratio/ge < 10$ (where $ratio$ is one of the energy ratio combinations plotted). Also shown are the lines $ratio = 1$ and $\alpha = 2$, which are the cuts above which traditional wisdom would say the objects should not collapse. Three things are interesting about these plots, and the same is true for all except the top row.

The first is the collection of "orange" objects with $ratio < 1$ and $\alpha > 2$. The nature of these objects is still under investigation. The orange color indicates objects that are in the process of collapse, as non-collapsing objects are unable to reach such densities. These are likely highly non-spherical objects, or objects where the core definitions are not sampling the gas that one would naively expect to be collapsing.

The second is the collection of objects that exist in the bottom two rows that have $\alpha < 2$ but $ratio > 1$. Energetic arguments would forbid these objects from collapsing, but α arguments would pick them up as bound. Further studies will track these objects in time to determine if they do in fact collapse.

The third population is the collection of "red" objects that have fully violated the Truelove condition. They're concentrated in the quadrant that one would

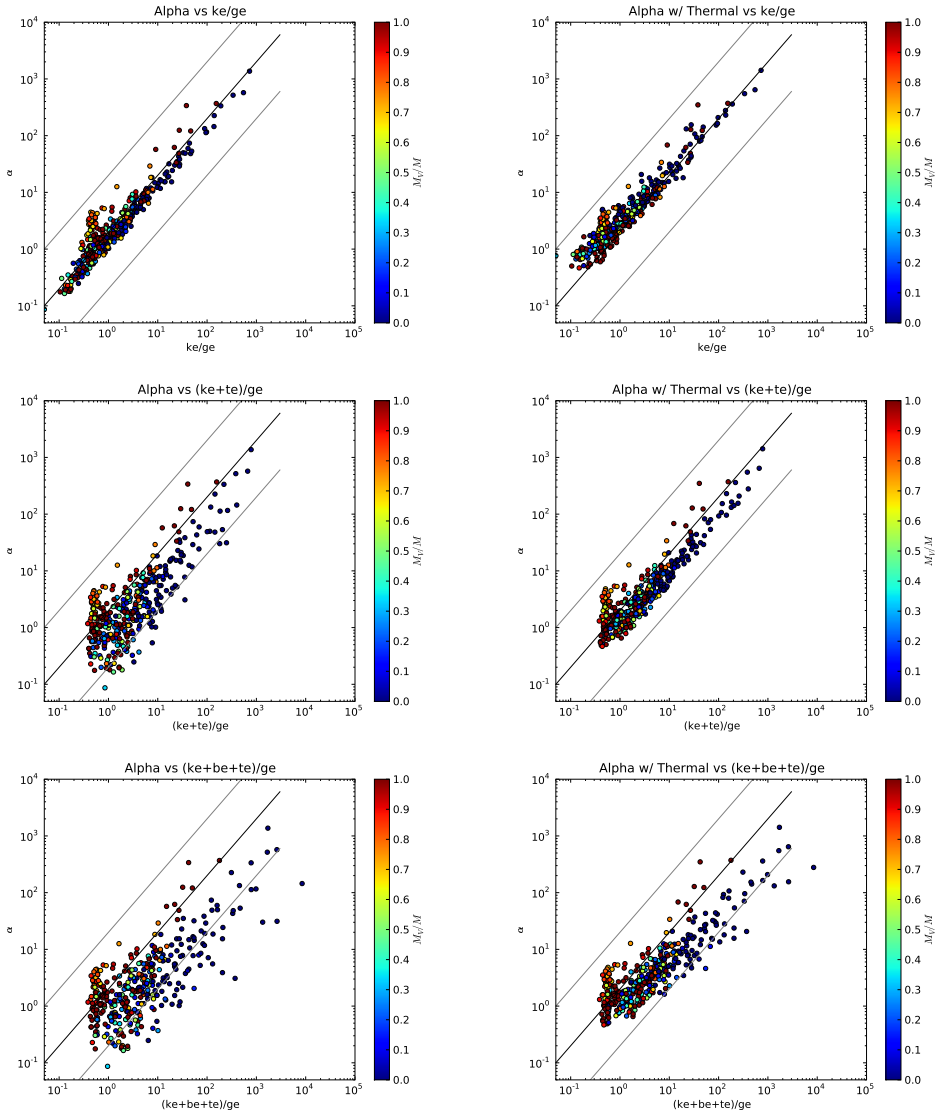

Figure 4.10: A comparison of $\alpha = 5\sigma^2 r/(GM)$ with ratios of Kinetic (ke), Thermal (te) and Magnetic (be) energies to Gravitational Energy (ge). Color bar denotes fraction of core above the Truelove Density. Top: ke/ge; Middle: (ke+te)/ge; Bottom: (ke+te+be)/ge. σ is the velocity of the object: in the left column, σ includes only the fluid velocity; the right column combines both fluid and thermal.

expect, $\alpha < 2$ and $ratio < 1$, but more interestingly is how uniformly they're spread throughout the distribution. The exact nature of the cores with $ratio >> 1$ and $\alpha >> 2$ has not been fully investigated, but indicates that these criteria may not be necessary *or* sufficient to indicate collapse.

Plots 4.10 and 4.11 show that approximating cores as uniform density spheres is not unreasonable, but is neither necessary nor sufficient in determining the collapse future of a given core.

Dib et al. (2007) analyzed a series of simulations from Vázquez-Semadeni et al. (2005) in an attempt to answer the same question, namely what physical quantities are correlated with collapsing objects. They analyze all the surface terms in the Virial Theorem in detail, α_{vir} as defined by equation 4.3, the number of Jeans masses in a core, and the mass-to-magnetic-flux ratio. They find no one-to-one correspondence between any of these tracers and gravitational boundedness, which is consistent with what we find here, though their simulations are significantly lower resolution than the ones presented in this thesis. Additionally, they show that the surface terms from the Virial Theorem are on the same order as the volume terms, further calling into question the validity of using α_{sphere} from equation 4.3 as a tracer. Ballesteros-Paredes (2006) attacks a number of assumptions about the Virial Theorem that go into using α_{sphere} in specific, and the Virial Theorem in general, as a tracer of collapse. He finds a number of conclusions that further validate the point made here; first, that the compressive/expansive and vortical components of the velocity of a core (or really, any object) must be treated separately since compressive motions aid collapse, while the other two prevent collapse; second, that the surface terms cannot be neglected; third, that the gravitational energy in the Virial Theorem is not only the self gravity of the object, but contains additions from the surrounding gas, so not exclusively a term that aids in collapse. These arguments further call the use of α_{sphere} into question when the issue of whether a clump of gas will collapse.

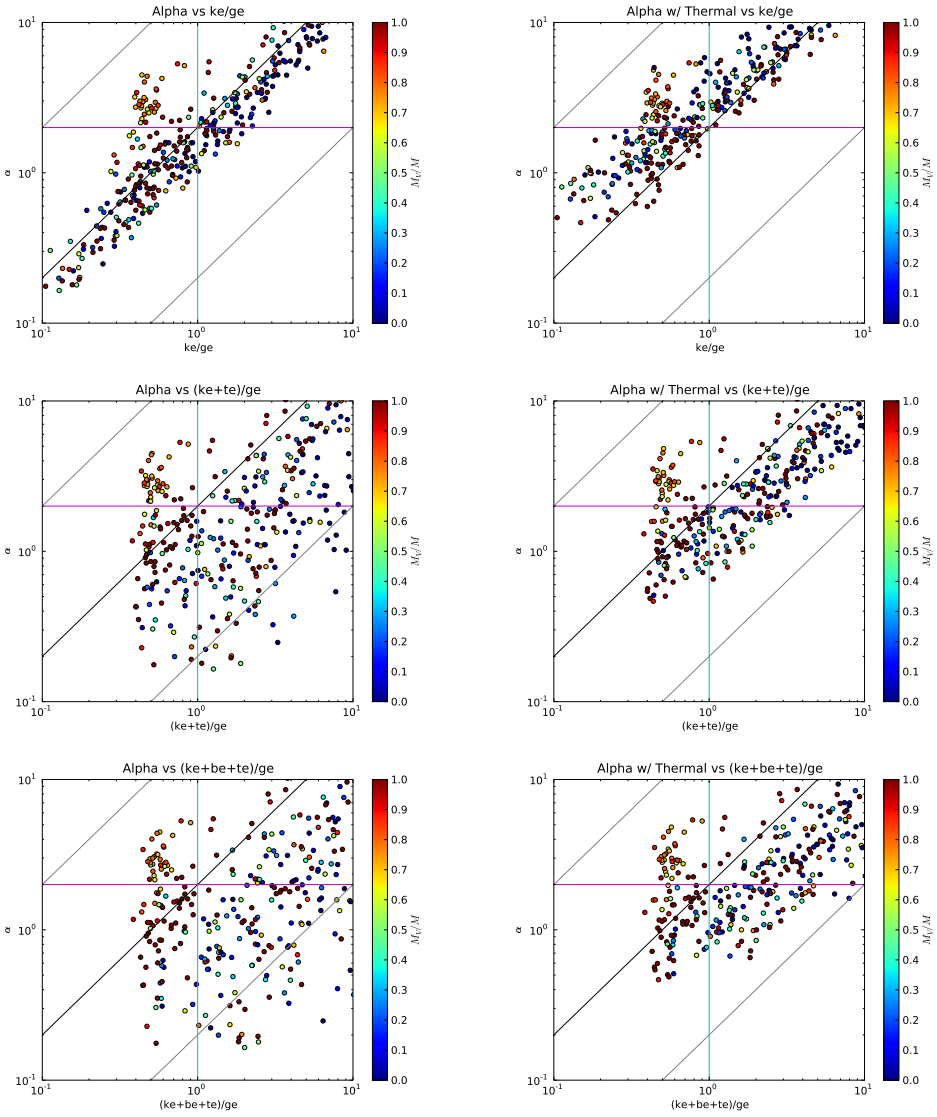

Figure 4.11: Same plot as 4.10, but only showing $\alpha < 10$ and $ratio < 10$. Also shown are the lines $ratio = 1$ and $\alpha = 2$, which are the cuts above which traditional wisdom would say the objects should not collapse. (here $ratio$ is the given ration on the x axis)

4.5 Resolution Study

Here we present a resolution study in which we examine the effects of increasing the maximum of refinement by a factor of 4, from 4 levels to 6. Future studies will examine this further, as well as examine the effects of increasing root grid resolution.

The decaying run $ok1$, with $\alpha_{vir} = 1.30$ was repeated with an additional two levels of refinement, for a total effective resolution of 8192^3. The 6 level run ($ok8$) took approximately twice as long to run and used approximately 50% more memory than the 4 level run. This is a substantial savings over increasing the total box size by a factor of 4, which would increase the CPU time by a factor of 256 and memory by a factor of 64.

It was demonstrated by Truelove et al. (1997) that if the Jeans Length $\lambda_J = \sqrt{\pi c_s^2/G\rho}$ is not resolved by at least 4 zones, a Gaussian sphere would artificially fragment into smaller structures that were not present in more highly refined simulations. This has become the standard minimum resolution for self gravitating simulations. By their reasoning, we could anticipate artificial fragmentation as our cores violate the Truelove condition. This would manifest itself as a higher number of small cores in the lower resolution run relative to the higher one, as fragmentation would break large cores into smaller ones and increasing the resolution would halt that process. This is not seen.

Figure 4.12 shows four projections at roughly 2 Myr for both the 4 level simulation (top row) and the 6 level (bottom row). The left column shows the entire box, and the right column images are restricted to the central 25% of each simulation. The left column images show that the basic large structures are nearly identical in both simulations. The right column images show that some cores in the 4 level run are broken into smaller cores that then dynamically interact with each other and their environments.

Figure 4.13 shows the density PDF for the three runs with $\alpha = 1.3$. The blue line is the driven run, the green line is the undriven run (both 4 level) and the red line is the undriven run with 6 levels. It is interesting to note that the width of the PDF does not change between the three runs, demonstrating first that

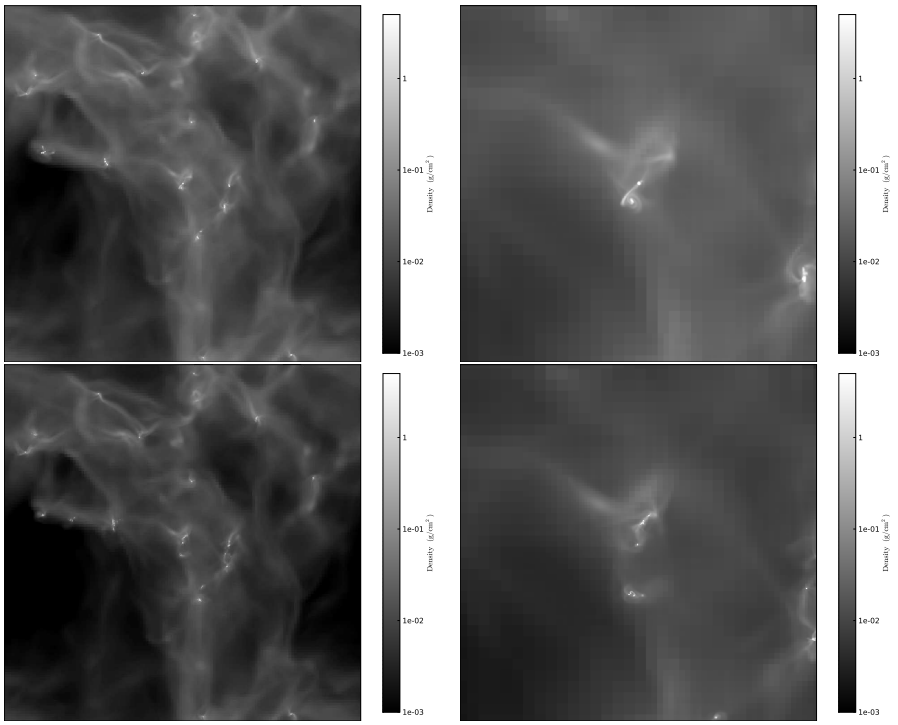

Figure 4.12: Density projections for resolution study. Top: 4 levels. Bottom: 6 levels. Right column is a zoom in of the central 25% for each. In general, the two runs are quite similar, but zooming in reveals more small scale detail in the higher resolution run.

resolution doesn't change the bulk of the material, and second that a single free fall time is not enough time to redistribute the mass away from the initial PDF. The rms Mach number for the driven run is still 9, while the other two runs have decayed to 5.

The second feature is the power law between $\rho = 5 \times 10^{-21}$ and 1×10^{-18} g/cm^{-3}. As mentioned in 4.3, this power law is reported in other simulations of gravoturbulent fragmentation. We also see that the slope of the power law is unchanged with resolution.

The final feature is the very high density deviation from the power law. The 4 level runs deviate from a power law at roughly 1×10^{-18} g/cm^{-3}, while the power law in the 6 level run extends for another factor of 15, roughly the increase in resolution. The vertical lines mark the Truelove density for each of the runs. While the Truelove density coincides with the knee, figure 4.8 shows that it is in fact due only to linear spatial resolution.

These PDFs further demonstrate that the large scale features of these simulations are robust against changes to the refinement, while the small scale details are altered somewhat.

Figure 4.14 shows the mass distribution for cores with $\alpha_{vir} < 2$ One can see that the peak of this distribution is around $1M_{\odot}$, consistent with observations by Chabrier (2003) (section 4.8.1), but the higher resolution run peaks at slightly lower density and has significantly more small mass cores. Unfortunately, this demonstrates that the mass distribution is unconverged, and higher resolution will be needed in the future to obtain converged mass distribution.

Figure 4.15 serves to further illustrate the changes to the cores with increasing resolution. Both figures show the non-thermal velocity dispersion σ in units of the sound speed vs. the size of the core R. The 4 level run is on top, the 6 level run on bottom. As with other plots, the color of each point is the fraction of mass in the core above the Truelove density, which serves to indicate how collapsed the core is. Two regions in each plot are clearly distinguished. The first is the collection of larger cores around $10^{-1}pc$. These are nearly identical in both simulations, in both slope and violation parameter, indicating that cores on

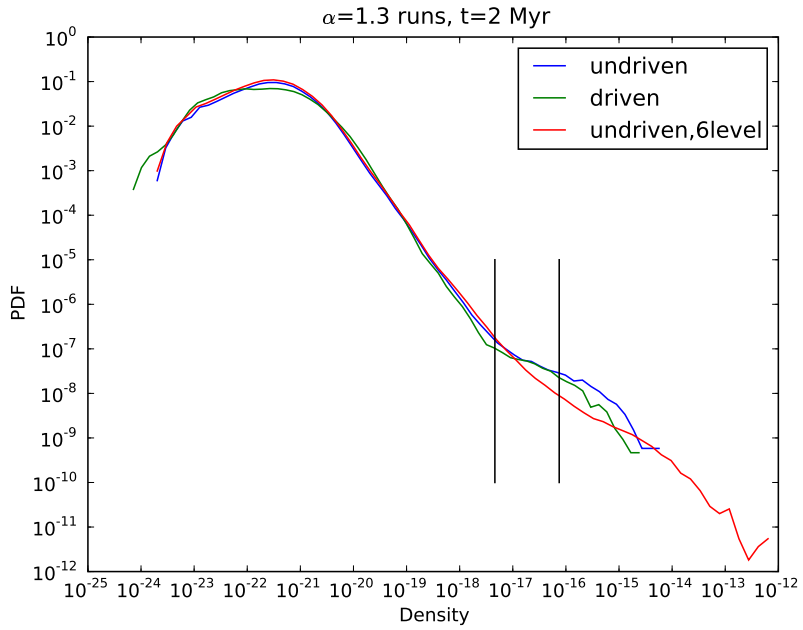

Figure 4.13: Density PDF for 4 and 6 levels. One can see that the power-law tail goes out further before flattening. This shows better mass resolution. The vertical lines mark the Truelove density for both resolutions, with the higher density bar being for the higher resolution run.

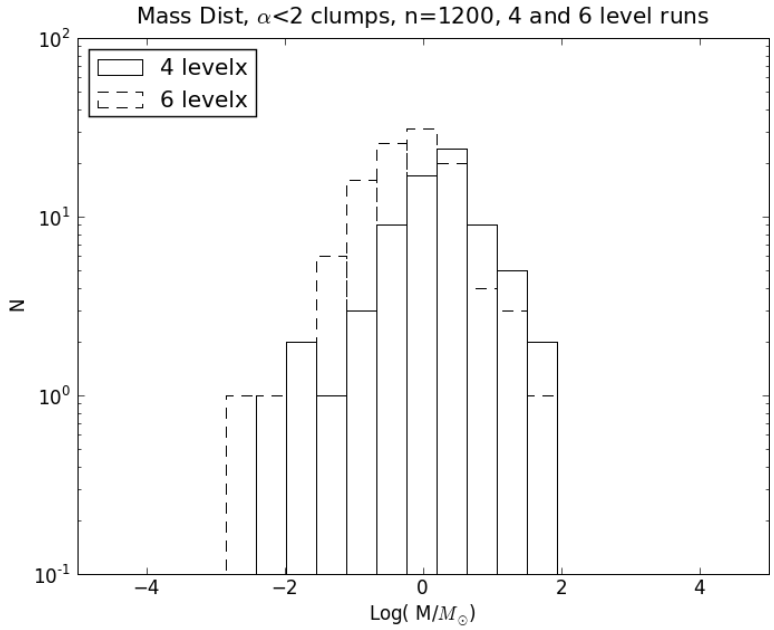

Figure 4.14: Mass distributions for $\alpha < 2$ cores in the 4 level (solid) and 6 level (dashed). One can see that the two distributions are similar, but higher resolution causes significantly more small scale cores. This indicates that our lower resolution runs are not subject to the artificial fragmentation predicted by Truelove et al. (1997)

this scale are not altered by increasing refinement. The second population is the collection of small cores around 10^{-2}. As the resolution is increased, this population shifts to smaller sizes and becomes more numerous. The small objects have fully collapsed, as indicated by the amount of gas above the Truelove density, and will likely continue collapsing as far as the resolution will allow. The larger objects are in earlier states of collapse, indicated by the lower fraction of mass above the Truelove density.

These simulations were normalized to an outer scale of $6pc$, giving resolution elements of $2.9 \times 10^{-3} pc$ for the 4 level run and $7.3 \times 10^{-4} pc$ for the 6 level run. The resolution element can be clearly seen as the strong lower bound on the distribution of cores.

4.6 Magnetic Field vs Column Density

In this section we will discuss the nature of the relationship between mass and magnetic fields in these simulations. First we will discuss the relationship between total magnetic field strength B and volume density n in the entire volume. Second we will compare the line of sight magnetic field strength B_{los} and column density N relationship to cores observed in Zeeman splitting.

In ideal MHD, the infinite conductivity causes the field to be dragged along with the plasma exactly. Given a spherically collapsing region, density will increase as

$$\rho \propto R^{-3}. \tag{4.16}$$

Since the material can only contract the field perpendicular to the field,

$$B \propto R^{-2}. \tag{4.17}$$

This yields $B \propto \rho^{2/3}$. However, the material may flow preferentially along the field lines, which would cause the magnetic field to grow even more slowly with density. The geometry of the collapse will be determined by an array of factors, including relative mass to magnetic flux of each point in space and the turbulent environment.

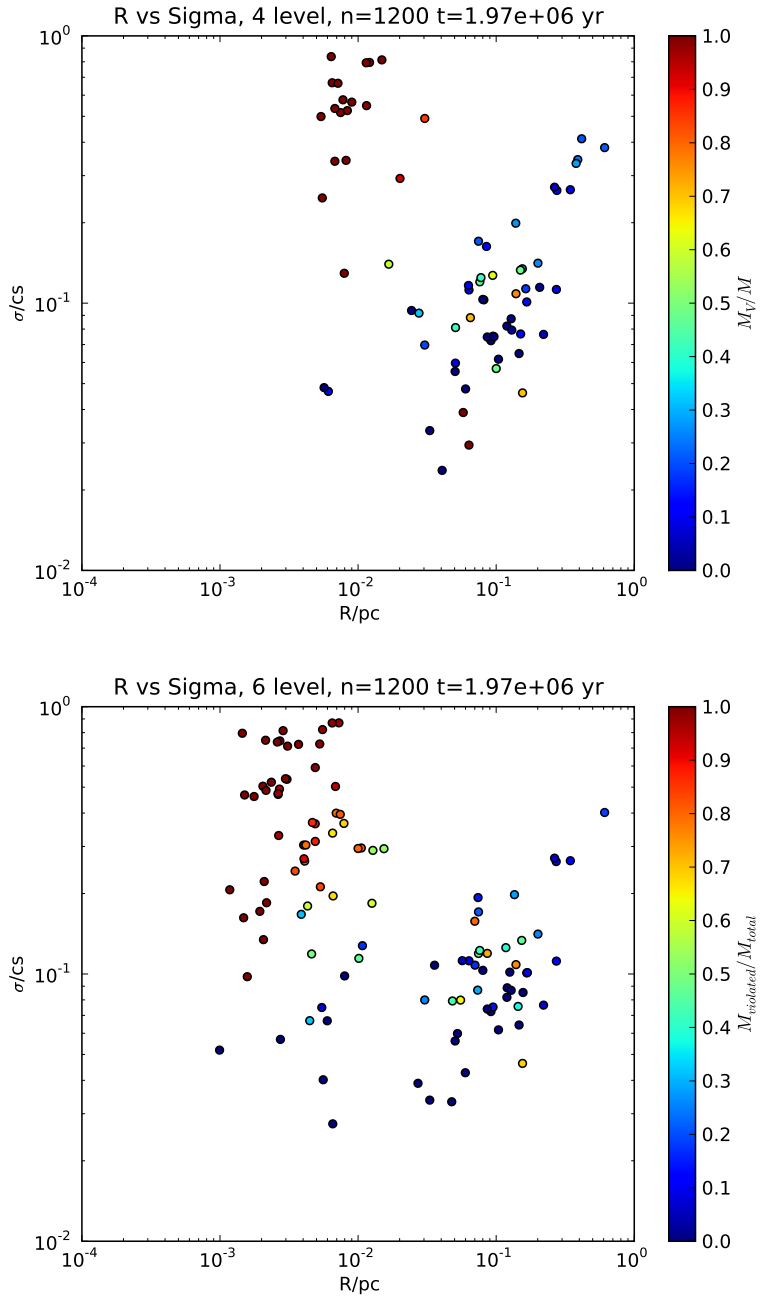

Figure 4.15: Linewidth Size relation for 4 level (top) and 6 level (bottom) simulations. Large cores remain relatively unchanged, but small cores get smaller, and there are more of them.

When comparing with the column density N and line-of-sight magnetic field B_{los}, the exponent on the relation $B_{los} \propto N^{\gamma}$ will be somewhat larger: to first approximation, $N = \rho R$, which will serve to increase the exponent in equation 4.16 by one. The power on the magnetic field scaling in equation 4.17, on the other hand, will remain unchanged, since the frequency shift between the left and right polarization states due to the Zeeman splitting is unchanged by the column depth. Thus we expect the $B - N$ relation to be somewhat steeper than the $B - \rho$ relation.

Padoan & Nordlund (1999) collect data from several observations and fit the upper envelope with $B \propto \rho^{0.4}$. Their result is reproduced in figure 4.16. This is somewhat more shallow than the naive spherical collapse approximation, indicating some level of flow along the field. Lunttila et al. (2008) and Troland & Crutcher (2008) find $B_{los} \propto N^{2/3}$, which is somewhat steeper than the volume density relation, as anticipated. This result, along with recent observational data from Troland & Crutcher (2008), are shown in figure 4.17.

Figure 4.18 shows the $B - \rho$ relation taken from the four driven $\alpha_{vir} < 2$ simulations at a time when the star formation efficiency $SFE = 0.15$. This time is different for each of the four simulations due to differences in their star formation rate, and serves as a reference state for the level of collapse experienced by each simulation. Also plotted is a powerlaw, $B \propto \rho^0.5$. The higher resolution simulation, in the bottom right, shows a somewhat different relationship than the other three, indicating that some of the behavior of the highest and lowest density gas, and highest and lowest field strengths are resolution dependent. There is a general trend for the upper envelope where the magnetic field strength is almost completely independent of density. This is not yet understood. Higher resolution simulations need to be run to establish the resolution dependence of the outer envelope, and better statistical measurements of the $B - n$ relationship need to be established in the future.

Figure 4.19 shows data from one of our simulations along with data from two different Zeeman splitting surveys. Cores with $\alpha_{sphere} < 2$ from the $\alpha_{vir} = 0.52$ run at $t = 0.75\ t_{ff}$ are the colored points; data from the OH Zeeman splitting

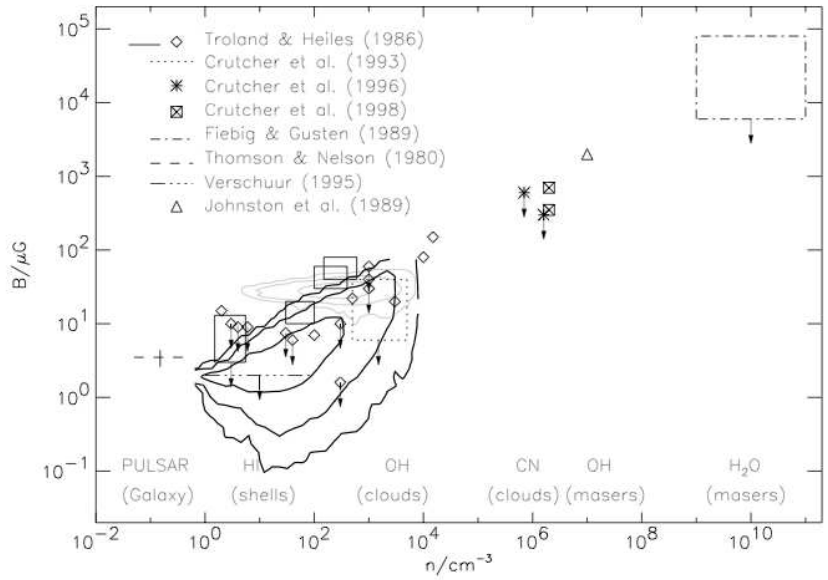

FIG. 7.—The *B-n* relation: observations and theoretical models. The thick contour lines are from the super-Alfvénic model Ad2 and the thin contour lines are from the equipartition model Bd1. Symbols are as follows: *diamonds*, Troland & Heiles (1986); *dotted line*, Crutcher et al. (1993); *asterisks*, Crutcher et al. (1996); *boxed X*, Crutcher et al. (1999); *dot-dashed line*, Fiebig & Güsten (1989); *dashed line*,Thomson & Nelson (1980); *triple-dot–dashed line*, Verschuur (1995); and *triangles*, Johnston et al. (1989).

Figure 4.16: Synthesis of multiple observations of magnetic field strength and volume density, taken from Padoan & Nordlund (1999).

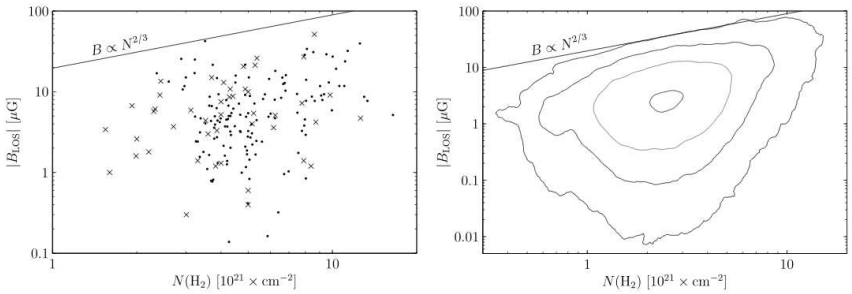

FIG. 2.— *Left:* Estimated line-of-sight magnetic field strength as a function of hydrogen column density. The dots show the results from our simulated observations. The crosses show the results from observations listed in Troland & Crutcher (2008) and Crutcher (1999). *Right:* The distribution function for $\langle N, B \rangle$ from the simulations, using all the points in the three synthetic Zeeman splitting maps. The contours are at levels 0.01, 0.1, 0.4, and 1.5 $(\log_{10}\langle N \rangle \log_{10}\langle B \rangle)^{-1}$.

Figure 4.17: This figure from Lunttila et al. (2008) shows observed $B - N$ relation from Troland & Crutcher (2008) (left) and the same relation from the simulation.

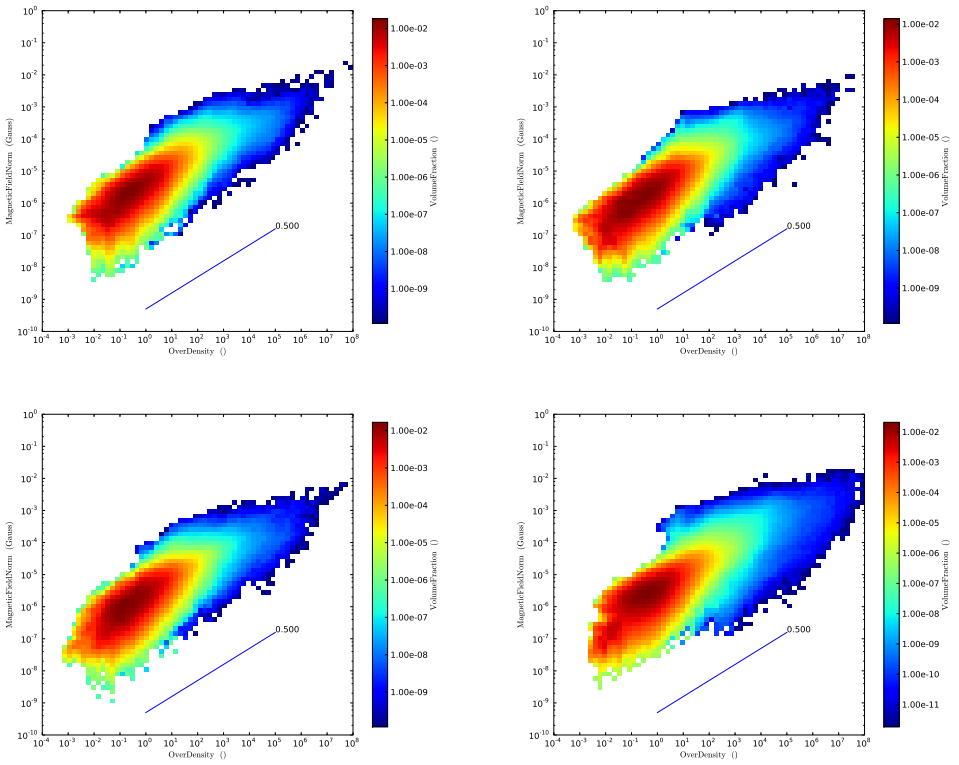

Figure 4.18: $B - \rho$ phase plot for four driven $\alpha_{vir} < 2$ runs. Clockwise from top left: $\alpha_{vir} = 0.52$; $\alpha_{vir} = 0.91$; $\alpha_{vir} = 1.30$, 6 levels; $\alpha_{vir} = 1.30$

measurements of Troland & Crutcher (2008) are the black points; and data from the CN Zeeman measurements of Falgarone et al. (2008) grey points. The trend for cores looks somewhat like $B_{los} \propto N^{2/3}$, though again a better statistical diagnostic should be developed. Color denotes fraction of the core above the Truelove density, which serves as a tracer of the level of collapse experienced by each core. This plot demonstrates several key things. First, our code successfully reproduces the magnitude and relation between B_{los} and column density for two independent measurement using two different molecules. This demonstrates that the turbulent fragmentation picture can accurately reproduce the relationship between density and magnetic field seen in nature. This includes the quite high magnetic field strengths seen in cores, as high as 1 mG, despite weak initial field strength of ~ 0.5 μG in both observations and simulations. This is a great victory for the turbulent fragmentation model. Second, since M_V/M traces the amount of very dense gas in an object, it serves as a tracer for how "collapsed" and object is. Since CN measured in Falgarone et al. (2008) (grey points) traces higher density material than OH, it is a likely indicator that the objects of Falgarone et al. (2008) are more collapsed than those in Troland & Crutcher (2008), likely indicating different phases of collapse.

4.7 Linewidth Size

One of the key indicators of the existence of turbulence in star formation is the linewidth-size relation noticed by Larson (1981). Here we compare our results to the cores in the Zeeman splitting measurements in section 4.6. In figure 4.20 we plot velocity dispersion σ vs. size as defined in section 4.5 for cores found in the $\alpha_{vir} = 0.52$ run at $t = 0.75t_{ff}$ (colored points). Also plotted are the CN measurements from Falgarone et al. (2008) (grey points) and the OH measurements from Troland & Crutcher (2008).

Figure 4.20 shows the velocity vs. size for three populations of cores: cores from the OH Zeeman splitting survey of Troland & Crutcher (2008) in black; cores from the CN Zeeman splitting survey of Falgarone et al. (2008) in grey; and cores

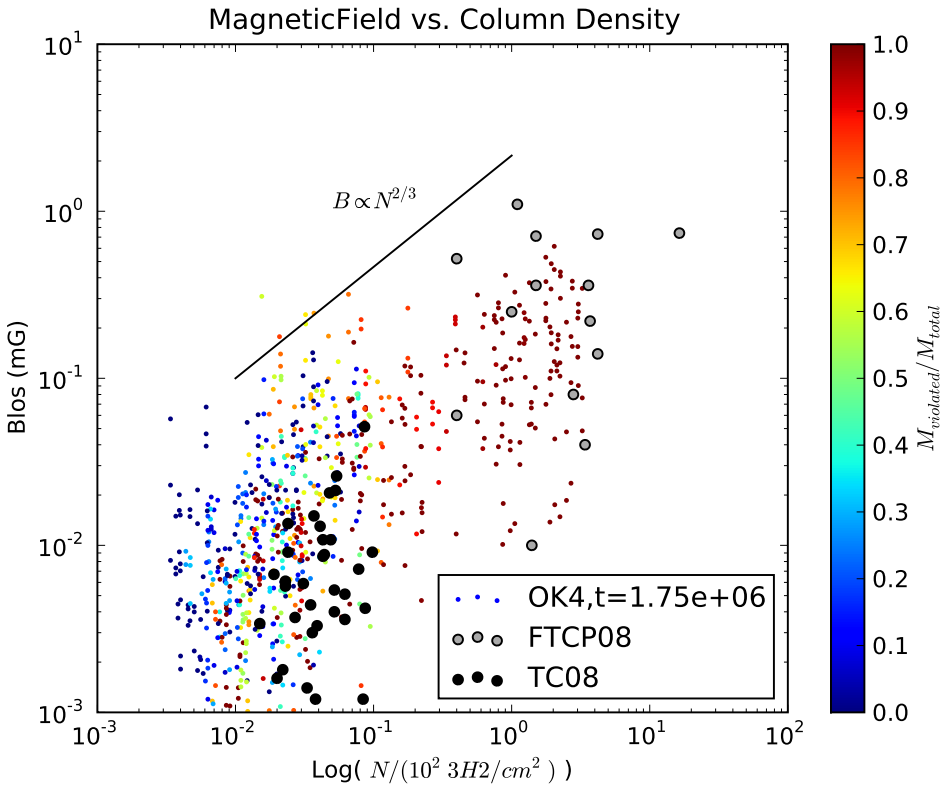

Figure 4.19: Magnetic Field vs Column Density for $\alpha_{vir} < 2$ cores in simulation *ok4* at n=750 (colored points), data from Troland & Crutcher (2008) (black points) and Falgarone et al. (2008) (grey points). The trend for cores looks somewhat like $B_{los} \propto N^{2/3}$. Color denotes fraction of the core above the Truelove density

from the $\alpha_{vir} = 0.52$ simulation at $t = 0.75t_{ff}$ with $\alpha_{sphere} < 10$ for each core, again colors show the fraction of mass above the Truelove density. Also plotted is the observed linewidth size relation $\sigma = (R/\mathrm{pc})^{0.5}$. One can see that the cores in our simulation match the observed powerlaw from Larson (1981) and the observed cores from the two Zeeman splitting surveys. When simulated cores broken into color segments, or equivalently segments of degree of collapse, one sees that each color band matches the observed power law well, with increasingly contracted objects moving to smaller sizes and higher velocity dispersions.

One feature of figure 4.20 is the general shift of simulated cores to the left along the powerlaw. This is due to observational sensitivity and resolution, as well as core selection in our simulation. Figure 4.21 shows all clumps found without selecting them to be without children. The range of values in the $\sigma - R$ relation populated by the observed points are now fully populated by simulated points, and the bands of constant M_V/M are more clearly seen to have similar slopes to the two populations of observed data.

4.8 Mass distribution

4.8.1 Stellar Initial Mass Function

One of the open questions in star formation is the origin of the stellar initial mass function (IMF). Salpeter (1955) first measured this and fit it to a power law,

$$dN = 0.03(\frac{M}{\mathrm{M}_\odot})^{-1.35} d\ln M. \tag{4.18}$$

This fit between was done between 1 and 10 $\mathrm{M}_\odot$ More recent studies have been done by Chabrier (2003) and Kroupa (2001). Chabrier (2003) found the stellar IMF fits a power law above $1\mathrm{M}_\odot$, and a lognormal below. Kroupa (2001) argues that the IMF is universal, indicating that a general underlying physical mechanism is responsible for star formation everywhere. These can be seen in figure 4.22.

Padoan & Nordlund (2002) predict the IMF by modeling it with supersonic, superalfvenic isothermal turbulence. By using the shock jump conditions from

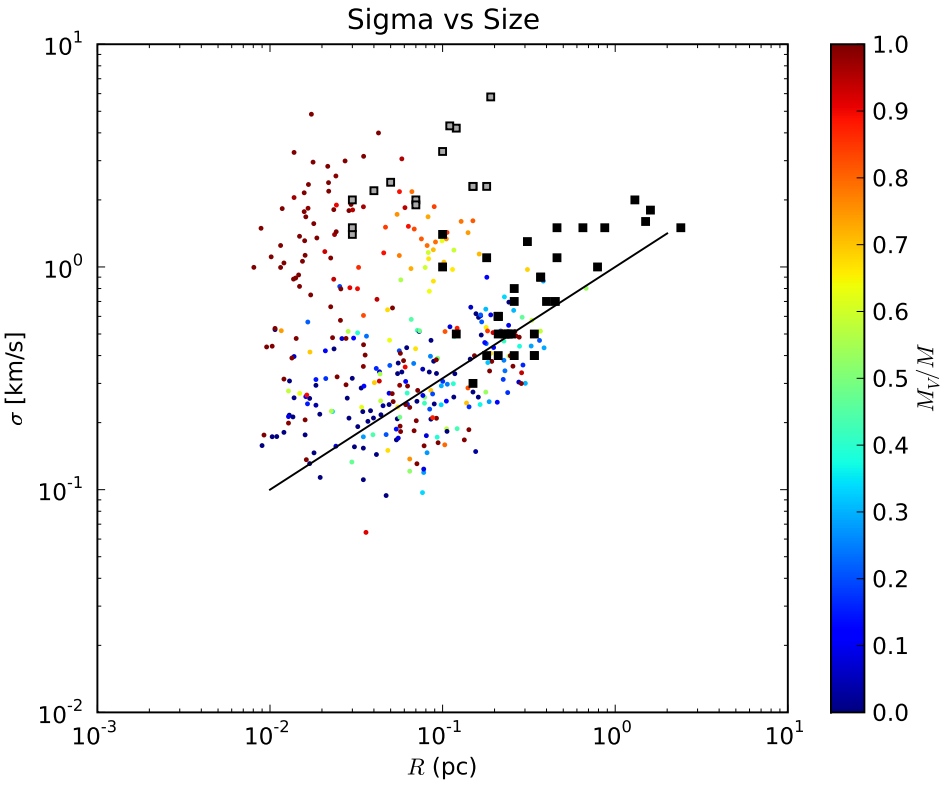

Figure 4.20: Line width Size Relation. Cores selected here are for $\alpha_{sphere} < 10$, and are from the $\alpha_{vir} = 0.52$ simulation at $t = 0.75 t_{ff}$. Grey squares are from Falgarone et al. (2008) CN Zeeman measurements, and the black squares are from Troland & Crutcher (2008) OH Zeeman measurements.

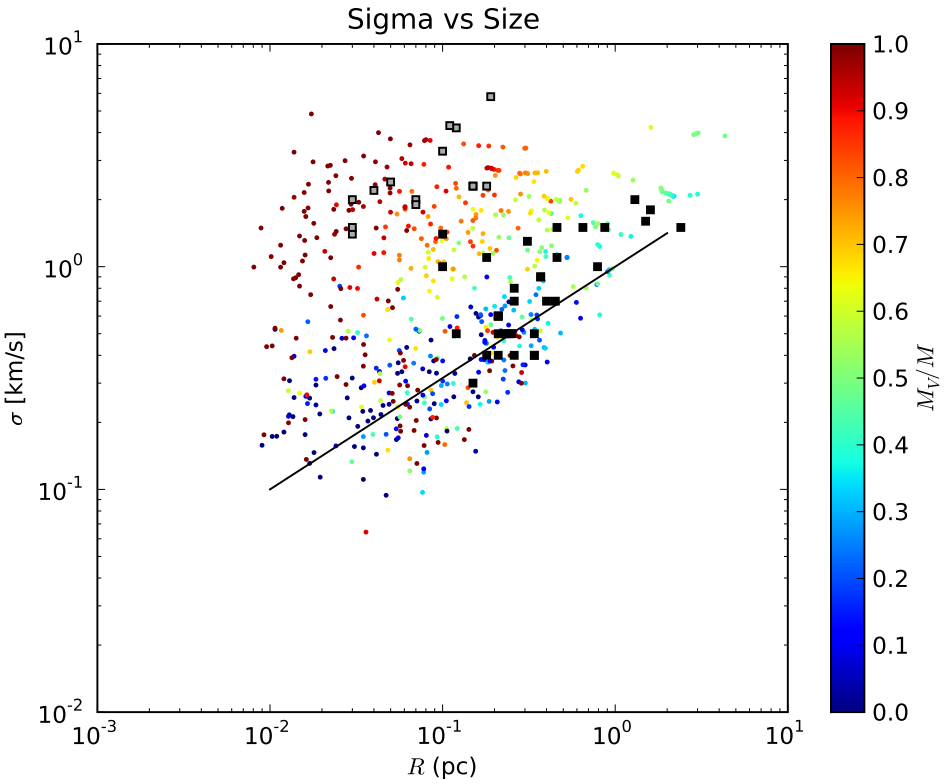

Figure 4.21: Line width Size Relation. Cores have no imposed cuts on number of children, but $\alpha_{sphere} < 10$. Grey squares are from Falgarone et al. (2008) CN Zeeman measurements, and the black squares are from Troland & Crutcher (2008) OH Zeeman measurements. Color indicates fraction of clump mass at densities above the Truelove density

MHD

$$\rho_1 \approx \ \rho_0 \mathcal{M}_A, \tag{4.19}$$

$$\lambda \approx \ L\mathcal{M}_A^{-1}, \tag{4.20}$$

$$B_1 \approx \ B_0 \mathcal{M}_A, \tag{4.21}$$

the lognormal density PDF of isothermal turbulence,

$$P(x)d\ln x = \frac{1}{\sqrt{2\pi\sigma^2}}\ exp\left[\frac{(\ln x - \mu)^2}{2\sigma^2}\right] dy, \tag{4.22}$$

and using the spectral energy index β, where

$$E(k) \propto k^{-\beta},$$

they arrive at the following mass distribution:

$$dN \propto m^x d\ln m. \tag{4.23}$$

$$x = -3/(4-\beta) \tag{4.24}$$

Given $\beta = 1.74$, as found in Boldyrev et al. (2002), they find and exponent of $x = -1.33$, remarkably close to (Salpeter, 1955). For the measured slope from a suite of compressible $\mathcal{M} = 10$ turbulence runs, Padoan et al. (2007) find $\beta = 1.9$, which gives a slope $x = -1.4$ For our simulations, $\beta = 2.2$ so this would predict $x = -1.7$

Using the hydrodynamic jump conditions instead of the MHD conditions,

$$\rho_1 \approx \rho_0 \mathcal{M}^2 \tag{4.25}$$

$$\lambda \approx L\mathcal{M}^{-2} \tag{4.26}$$

Padoan et al. (2007) find a much steeper power law

$$x = -\ 3/(5-2\beta) \tag{4.27}$$

$$dN \propto m^x I(m) d\ln m \tag{4.28}$$

which for the same $\beta = 1.9$ gives a slope $x = -2.5$. This is a substantial difference between hydro and MHD, and gives a result that is inconsistent with observations. This indicates that magnetic fields may play a vital role in determining the properties of stellar distributions.

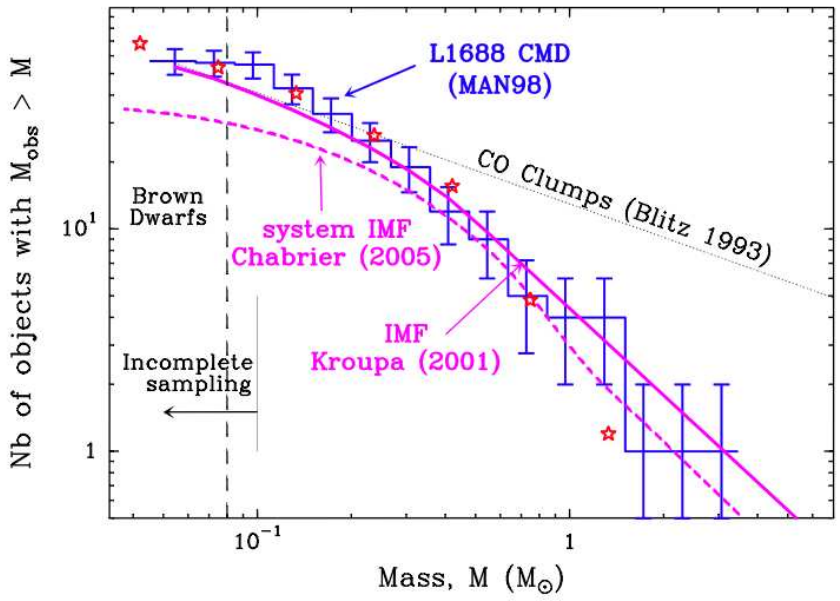

Figure 4.22: Cumulative mass distributions for stars and cores, taken from André et al. (2007). The pink curves show the stellar IMFs from Chabrier (2003) and Kroupa (2001), and the blue points show the data from Motte et al. (1998)

Padoan & Nordlund (2002) then extend the core distribution in equation 4.23 to the bound object distribution by multiplying 4.23 by the probability that the mass is above the Jeans mass, taken from the PDF in equation 4.22, to get

$$dN \propto m^{-3/(4-\beta)} \left[\int_0^m P(m_J) dm_j \right] d\ln m. \tag{4.29}$$

This successfully fits both the slope at high mass and the low mass turnover $M < 1\mathrm{M}_\odot$.

4.8.2 Core Mass Distribution

The next challenge is to connect stellar IMF observations with the above model by way of the core mass distribution, and finally to the numerical models presented here.

The first step in the chain is connecting core observations with the stellar IMF. A number of authors have been fairly successful with this recently. Figure 4.22 shows the core mass distribution found from Motte et al. (1998). These cores

are found from a millimeter continuum map of the ρ Ophuchi cloud. They overlap the stellar mass distribution extremely well, suggesting that this population of cores will become stars in a nearly 1-1 fashion.

This has been taken as a strong evidence that cores form directly from the turbulence. It has been argued (Clark et al., 2007) that the lifetime of these condensations depends strongly on the mass of the core, so the core mass function that matches the IMF so well might evolve away from a decent match due to differential collapse rates, and then evolve back through accretion. André et al. (2007) accounted for this by weighting the core mass distribution by the inverse free fall time, which would give the initial core distribution. However, since higher mass objects are basically uncorrelated with their density, this served only to increase the peak of the distribution slightly, without changing the slope of the power law end.

Other surveys do not match the observations as well as Motte et al. (1998). Enoch et al. (2007a) compare a combined survey of Perseus, Serpens and Ophiuchus and found that the peak of their distribution roughly 4 times larger than the peak of the stellar IMF peak. Figure 4.23 shows the CMF they obtain overplotted with the Chabrier (2003) and Kroupa (2001) mass functions results, and is shifted to the right noticeably. This shift in peak is likely due to incomplete sampling at the low mass range. Enoch et al. (2007a) mention that it may be indicate that only 1/4 to 1/3 of the core mass will go into stellar mass.

Figure 4.24 shows the normalized cumulative mass distribution of three populations: Data from our $\alpha_{vir} = 0.52$ simulation at $t = 0.75 t_{ff}$, with cores selected using total energy ratio as discussed in section 4.4 (blue line); Combined class 0 and class I sources from the Perseus and Serpens star forming region combined, as measured by Enoch et al. (2007a) (green line); and data from the combined class 0 and class I sources from the Ophiuchs cloud, also from Enoch et al. (2007a). The Perseus and Serpens cores have nearly identical distributions, so are combined here. In this plot, the length scale in simulated data has been re-scaled to 1.6 pc, in order to get the peak mass to line up (see section 4.1 for scaling arguments.) Two things are apparent from this figure. First is the stark difference between

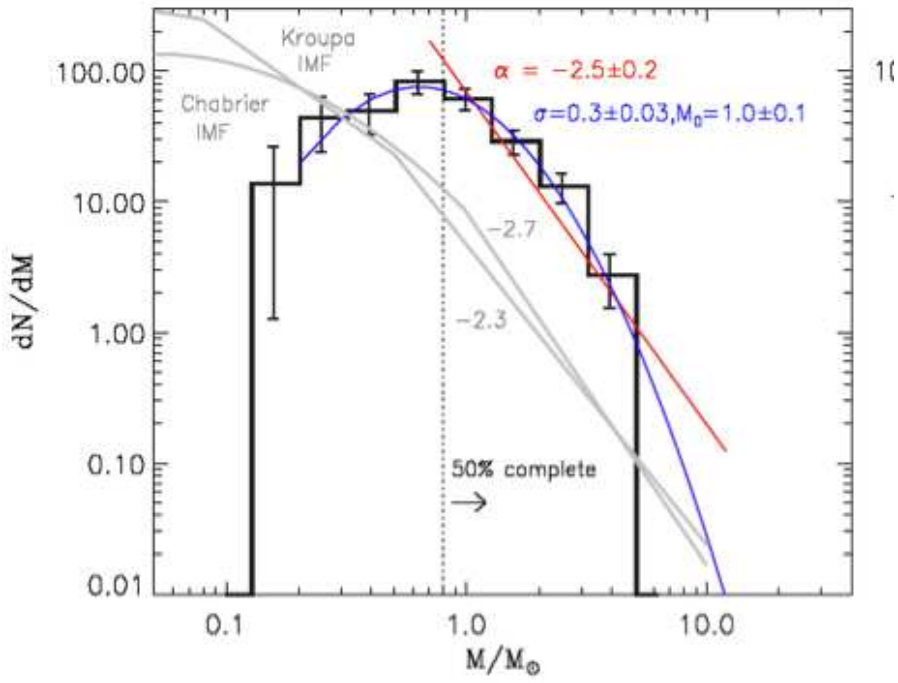

Figure 4.23: Core mass distribution from Enoch et al. (2007a)

the Ophiuchus region and the Serpens and Perseus regions (who's distributions are extremely similar). The Ophiuchus cores are typically lower mass and their distribution forms a power law, while the Perseus and Serpens data have a much more gradual decline. This suggests that star formation may not be as universal as pronounced by Kroupa (2001). The second is similarity in shape between the Serpens/Perseus data and our simulated data. It is not likely that data selection technique plays a large part in the difference in figure 4.24 since all three clouds were selected with an identical technique ((Young et al., 2006; Enoch et al., 2006, 2007b)). Differences may arise from differences in the sensitivity or resolution to each of the clouds, but such a comparison is beyond the scope of this work.

4.9 Star Formation Rate

One of the biggest unanswered questions in astrophysics is the rate at which molecular clouds turn into stars. The Milky Way contains $\sim 10^9 M_\odot$ of molecular

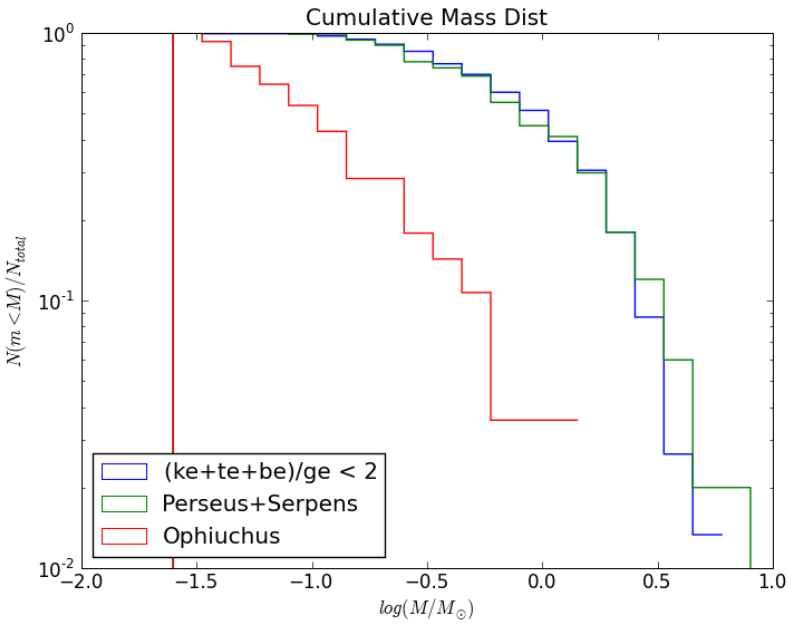

Figure 4.24: Cumulative Mass Distribution: simulated objects selected by energy ratio (blue line), Serpens and Perseus cores (green line) from Enoch et al. (2007a) and Ophiuchus cores (red line) from Enoch et al. (2007a)

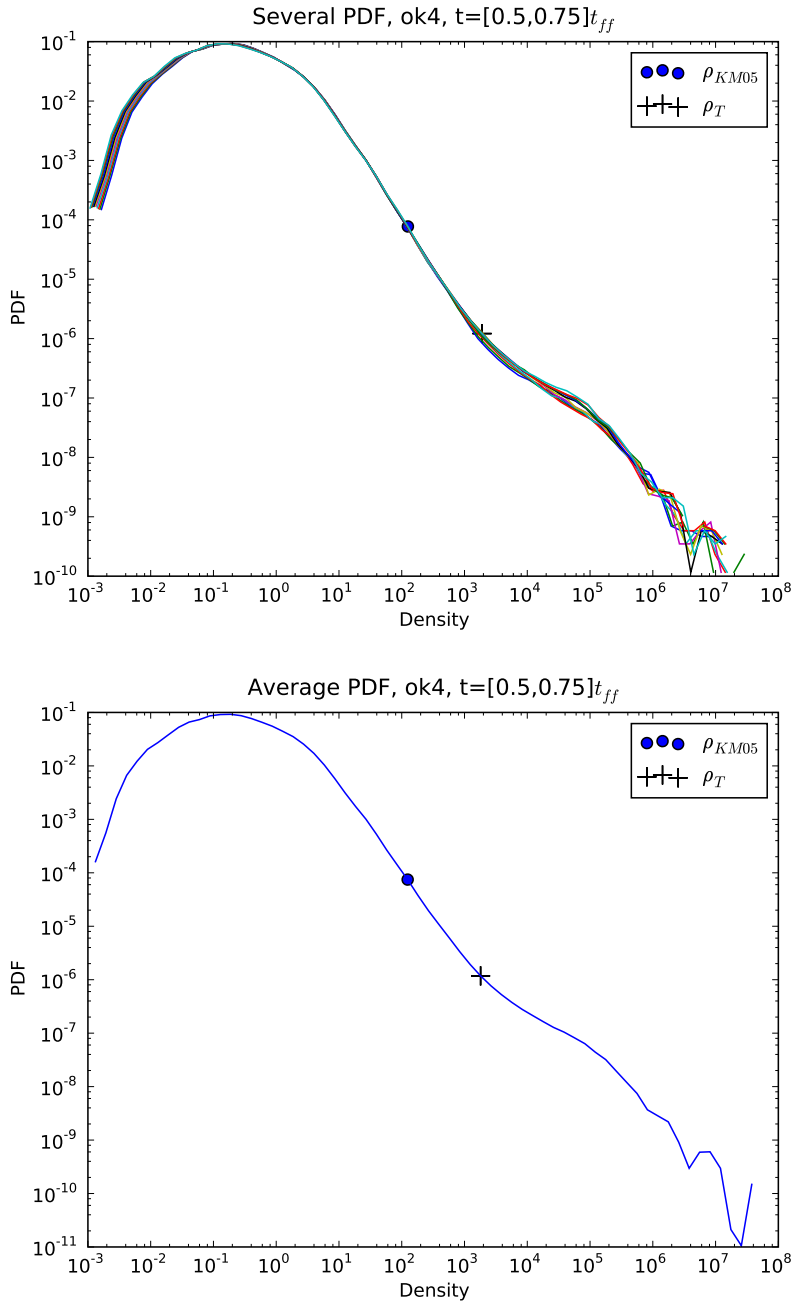

Figure 4.25: Average PDF of 10 steps between $t = 0.5t_{ff}$ and $t = 0.75t_{ff}$ of the $\alpha = 0.52$ (ok4) run. Top: All steps over plotted. Bottom: averaged. The circle indicates the critical density predicted by Krumholz & McKee (2005), and the plus indicates the Truelove density.

gas (Williams & McKee, 1997) with an average free fall time of $t_{ff} \sim 4$ Myr. If all the gas were collapsing in free fall, this would give a star formation rate of $250 M_{\odot}/yr$. This is two orders of magnitude larger than the observed star formation rate of $\sim 3 M_{\odot} yr^{-1}$ (McKee & Williams, 1997). Until quite recently, the prominent support mechanism proposed was magnetic fields (Mouschovias, 1987a,b). However, recent observations have all but eliminated this possibility (Crutcher et al., 2009).

4.9.1 Predicting Star Formation Rate

Krumholz & McKee (2005) suggested the first comprehensive prediction of the star formation rate that works on a broad range of galactic star formation environments. Their work builds on the idea of Padoan (1995) wherein the log-normal density PDF is used to predict the star formation efficiency in a cloud. Below a certain length scale λ_s, the velocity fluctuation across an eddy is lower than its sound speed. Eddies of this size will not have support against gravitational collapse from their internal turbulent motions.

This can be translated into a density scale by examining the Jeans length

$$\lambda_J(\rho) = \sqrt{\frac{\pi c_s^2}{G\rho}}, \tag{4.30}$$

the length at which cores become gravitationally unstable, and the density at which the local Jeans length is less than the sonic length. Empirically (Larson, 1981; Solomon et al., 1987) the relationship between velocity and size follows a power law

$$\sigma_\lambda = (0.72 \pm 0.07)(\lambda/pc)^{0.5\pm0.05} kms^{-1}. \tag{4.31}$$

Given a sound speed of $0.2 kms^{-1}$ appropriate for $10K$ gas, we have

$$\lambda_s = (\frac{c_s}{0.72})^2 pc = 0.07pc. \tag{4.32}$$

Thus the over density at which the Jeans length is larger than the sonic length is the critical fraction

$$x_c = \left(\phi_x \frac{\lambda_J(\rho_0)}{\lambda_s} \right)^2, \tag{4.33}$$

where $\phi_x = 1.12$ is a numerical fudge factor determined by fits to simulations.

To generalize the star formation rate across different environments, Krumholz & McKee (2005) suggest using the star formation rate per free fall time, SFR_{ff}, which is defined as the fraction of a cloud's gas that can be converted into stars in a free fall time. Under their model, the mass that can collapse is the total mass above the critical over density, and that mass can collapse in a time scale $\tau = \phi_t t_{ff}$. Thus,

$$SFR_{ff} = \frac{\epsilon_{core}}{\phi_t} \int_{x_c}^{\infty} xP(x)dx, \tag{4.34}$$

where $P(x)$ is the density PDF (see section 4.3); $\epsilon_{core} \approx 0.5$ is the fraction of a core gas that does not reach the star due to ejection from stellar outflows, and is determined observationally (Matzner & McKee, 2000); and $\phi_t \approx 1.9$ is an adjustment for the actual timescale, determined by fits to numerical experiments.

The free parameters in hydrodynamic self gravitating turbulence can be viewed as the virial parameter α and the Mach number $\mathcal{M}$, since these show the relative importance of turbulence to gravity and turbulence to thermal pressure. Krumholz & McKee (2005) also provide a numerical fit to eqn. 4.34 as a dual power law in both parameters:

$$SFR_{ff} \approx 0.014 (\frac{\alpha_{vir}}{1.3})^{-0.68} (\frac{\mathcal{M}}{100})^{-0.32}. \tag{4.35}$$

Figure 4.26 shows the fraction of mass above the Truelove density vs. t_{ff} for the 4 driven runs with $\alpha_{vir} < 2$. There are two salient features of these runs: an initially exponential growth at low star formation rate, followed by a linear growth phase. The initial low growth is due to the simulation readjusting the the sudden presence of gravity.

The plot indicates the region fit for the SFR_{ff} with the grey bar. The region was selected in order to have an estimate of SFR_{ff} independent of the artificial simulation effects of the sudden introduction of gravity or the finite box size. This was determined by the abrupt changes in curvature seen most notably in the $\alpha_{vir} = 1.30$ run, where the exponential stops at $t \approx 0.75 t_{ff}$ and the slope changes again at $t \approx 1.5 t_{ff}$ when the slope increases again when a large fraction of

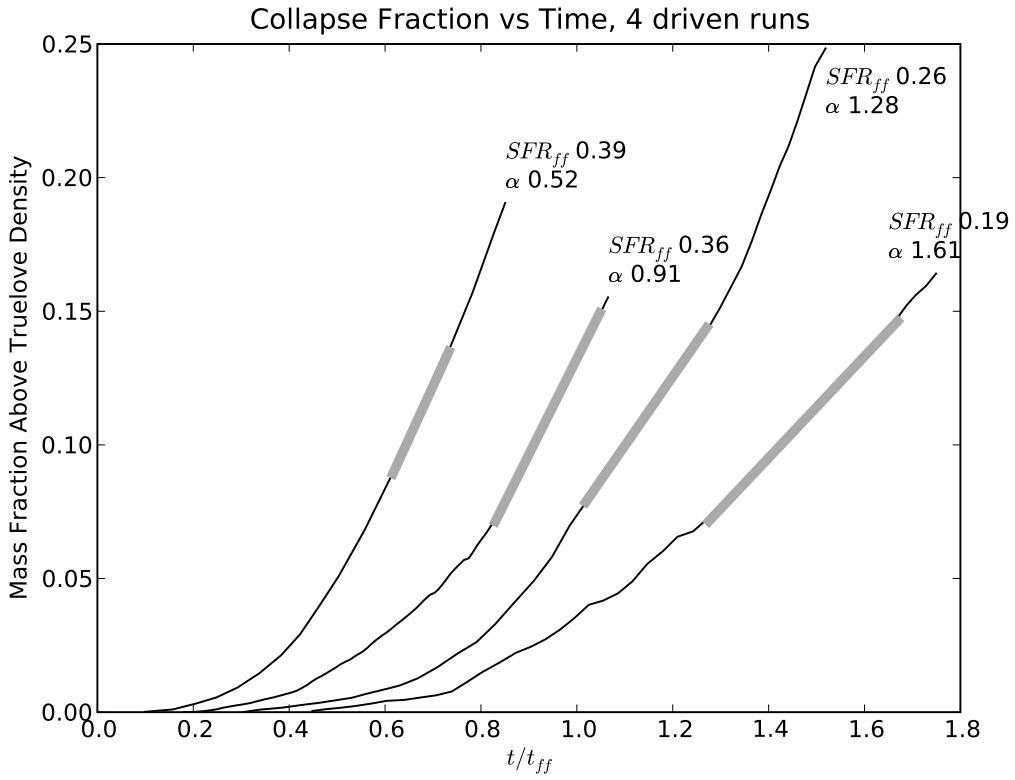

Figure 4.26: Fraction of mass above the Truelove density, $M_{violated}$ vs. free fall time. Fits are between $M_{violated}$=0.7% and 0.15%, where the Violation Rate is roughly linear.

the gas that was present in the turbulent phase preventing collapse has not been accreted into the dense stellar phase.

In figure 4.27, we plot the violation rate against 3 interpretations of equation 4.34. "KM05 analytic" is the literal interpretation of 4.34; "KM05 fit" is the value obtained from equation 4.35; and "KM05 simulated" is the same integral as in 4.34, but with the lognormal form of $P(x)$, replaced by the measured fraction of simulated density above x_c. One can plainly see a factor of $3 - 10$ discrepancy between the computed violation rate and the predicted values.

There are several possible reasons for this discrepancy. The first is that using the Truelove density as a proxy for SFR_{ff} is incorrect. However, Vázquez-Semadeni et al. (2008) performed a similar experiment and changed the density cut-

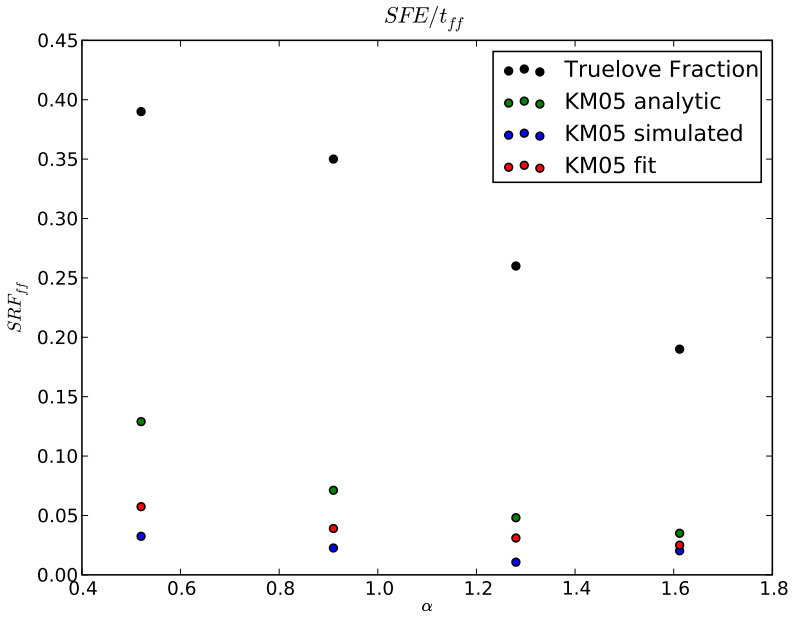

Figure 4.27: Star formation rates. Black points show the rate of growth of the fraction of mass above the Truelove density for each simulation. Green points show the analytic prediction of equation 4.34. Red points show the power law fit of equation 4.35. Blue points show the predicted rate of equation 4.34, with the analytic PDF replaced by the integral of the measured PDF.

off, and claimed that there was minimal change. The most likely answer, though, is that the root grid resolution in these simulations is too coarse, and numerical viscosity damps the turbulence at a much larger scale than it does naturally. This leads to a disruption of turbulent support at a much larger, thus much more massive, scale.

Chapter 5

Summary and Future Work

5.1 Summary

In this work, we have presented the implementation of MHD in the AMR cosmology code Enzo. EnzoMHD is capable of multi-resolution cosmological and non-cosmological astrophysical simulations using ideal MHD. We also presented preliminary results using the code to model self-gravitating isothermal MHD turbulence as the factory for the initial conditions of star formation.

In chapter 2, we presented the final version of EnzoMHD. EnzoMHD uses block structured AMR, which solves the hydrodynamic (and now magnetohydrodynamic) PDEs on fixed resolution patches, and communicates the finest resolution information between coarse and fine patches in way that is conservative in the volume-averaged quantities. This entails 4 basic components: the PDE patch solver, creation of fine grids (interpolation), communication of fine data back to coarse data (projection) and correction of the interface between coarse and fine grids (flux correction). MHD has the additional constraint that the divergence of the magnetic field, $\nabla \cdot \mathbf{B}$, must be zero to machine precision at all times, which requires additional machinery to advance the PDEs (Constrained Transport) and some modifications to the projection and flux correction steps. In addition to multi-resolution hydrodynamics, EnzoMHD includes the effects of gravitational acceleration and cosmological expansion, and a modification to the base PDE solver to account for flows with large disparity between kinetic and thermal energies (dual

energy formalism). In EnzoMHD, we use the PDE solver of Li et al. (2008) to solve the ideal MHD equations (section 2.1.6) for the patch solver, which is second order accurate in both time and space. We use a slightly modified version of the AMR algorithm procedure of Balsara (2001) to interpolate fine grids and project the more accurate fine grid data to the coarse grid (sections 2.1.11 and 2.4). We have used the CT methods of Balsara & Spicer (1999) and Gardiner & Stone (2005) to advance the induction equation while maintaining the constraint $\nabla \cdot \mathbf{B} = 0$(section 2.1.7). We have operator split the gravitational (2.1.8) and cosmological expansion (2.1.9) terms; and included the dual energy techniques of Ryu et al. (1993) and Bryan et al. (1995).

In section 2.2, we present the results of a broad array of tests to demonstrate the accuracy of the chosen methods. These include the shock tube of Brio and Wu 2.2.1, the isothermal shock of Kim 2.2.1, on dimensional MHD Caustics 2.2.1, the famous Zel'Dovich Pancake 2.2.1, the Vortex problem of Orzag-Tang 2.2.1, an adiabatic expanding universe 2.2.1. Some of these were additionally run with AMR, and the results compared to the unigrid case. The results of these overall agree with both what's been present in the literature before and comparisons with our existing PPM solver.

In chapter 3 we presented three other solvers extant in full or in part in EnzoMHD. The first of these is the solver of Ryu & Jones (1995), presented in section 3.1. This method is the MHD extension of the algorithm of Harten (1983). This solver combines the first order methods of Roe (1981) and Harten (1978) in a manner that is formally second order. Unfortunately this scheme proved too numerically diffusive to be able to provide reliable solutions to isothermal turbulence, and more important the small scale structure we will be relying upon to properly model the initial conditions of star formation. The second method is a new method, called DaveThena, and was presented in section 3.2. This method is a light weight variant of the solver of Gardiner & Stone (2005), which attempts to simplify the costly PPM integration by using a piecewise linear reconstruction. It is an unsplit algorithm, meaning it solves the 3d MHD equations in a single pass, rather than solving in successive sweeps. This is more suited to MHD. The fourth

and final method we introduced was the method of Ustyugov & Popov (2008), called PPML, presented very briefly in section 3.6. This has the most promise of all the solvers presented here due to its extremely low diffusivity, but due to its complex numerical structure it does not yet work with the AMR. These last two, DaveThena and PPML, both suffer from an explosive MHD instability that it is presently believed to be a problem with the unsplit nature of the solver.

In chapter 4, we presented new simulations of isothermal self gravitating MHD. These simulations, while somewhat preliminary, showcase the impressive dynamic range of the code and further bolster the case for MHD turbulence being the primary physical mechanism in star formation. In section 4.1, we presented a suite of 10 numerical experiments that were performed. These simulations varied the virial parameter α_{vir} in an attempt to explore its impact on the star formation rate. We found, as expected, that α_{vir} and the star formation rate are inversely proportional, but our simulations were too coarse on the root grid, so a detailed exploration was not meaningful. In section 4.3, we discussed at some length the density probability density function in self gravitating MHD, noting the prominent power law it develops in addition to the lognormal one expected from non-self-gravitating turbulence. In section 4.4, we examined the validity of the frequently practice of using the value of the virial parameter for a sphere to indicate collapse, noting that it often fails as a predictor for collapse. In section 4.5, we presented a brief resolution study as an indicator for the simulations that we hope to run in the future. We demonstrated that our while our simulations are unconverged, the increase of cores as resolution increased indicates that we are not susceptible to the artificial fragmentation reported elsewhere in under-resolved studies. In section 4.6 we explored the relationship between density and magnetic field strength. The column density vs. field strength as measured in cores in the simulation match the most recent observations of cores in the galaxy with unprecedented accuracy and range. Our simulations match both the observed relationship $B_{los} \propto N^{2/3}$ and $B \propto \rho^{1/2}$. It was also noticed that the upper envelop of the $B - \rho$ relation ship shows that peak field strengths are somewhat independent of density for high density collapsed regions. It is not clear if this is physical or a numeri-

cal effect, higher resolution simulations will explore this in the future. In section 4.7, we presented measurements of the relationship between velocity and size, reproducing observations with good accuracy. In section 4.8, we present the mass distribution in galactic cores and compare to those in our simulation. With one pair of star forming regions, our simulations match observations quite nicely, while for another they do not. The star forming region Ophiuchus shows a powerlaw in the normalized cumulative mass distribution. This is not seen in our simulations. However, Serpens and Perseus show a higher order turnover, which matches our simulations. This suggests to us that the long held belief that star formation is a universal process may not be exactly true. These three star forming regions are at different stages of evolution, or have different physical parameters, virial parameter, Mach number, Alfvén Mach number, which would alter the shape of the mass distribution somewhat. Since our simulations only varied one of these three parameters, virial parameter, the difference may show a dependence on one of the other two. Finally, in section 4.9 we compare the rate at which stars are formed in our simulation to the most prominent analytical model. Our simulations show a star formation that is roughly 3-10 times larger than predicted and observed. It is presently believed that the root grid resolution of this study was too low to accurately reproduce the model since the low resolution causes increased numerical dissipations, which decreases turbulent support at intermediate scales, which causes collapse of clumps that would normally be too large in spatial extent to collapse.

5.2 Future Work

The results presented here with the our newly developed AMR MHD code are extremely promising. There are several avenues we will be pursuing to adequately improve the picture of star formation.

Two new sets of simulations will be started shortly. These are a set of higher resolution simulations aimed at testing the convergence of these results and improving the turbulent support for collapsing structures, in order to improve

agreement with theory and observations. The second set of simulations will be a repeat of the four primary runs presented here, with the magnetic field set to zero. This will allow us to definitively examine the role of magnetic fields in this collapse process by comparing the magnetized and non-magnetized structures.

Two things that need to be more fully incorporated in analytic models of the star formation rate are the effects of MHD and the power law slope of the density PDF. Both MHD and power-law slopes are observed in simulations, but the analytic theory neglects them. MHD will likely shift the critical mass to higher densities, and the increased high mass power will add to the mass available to star formation. These need to be dealt with carefully analytically. Following that, we will be repeating this same suite of simulation expanding the root grid in an attempt to better resolve the severely unresolved turbulence scale, and comparing the analytic work to it. If the power-law and MHD can in fact be neglected, this will be apparent in the simulations that follow

With the data we already have, we will be finalizing a technique to track the collapsing clumps by examining the positions of the clumps closely spaced in time, to analyze the true history of the gas in a collapsed object. This will provide an unequivocal demonstration of the origin of the collapsed objects, thus strongly supporting or refuting the star formation picture.

The numerical software aspect of this project also has future plans. EnzoMHD diverged from the primary development branch of Enzo at the beginning of development. There have been a number of developments in Enzo that we wish to take advantage of, primarily the development of a generalizable Lagrangian particle that we will be using as sink particles. Sink particles will allow us to follow the ballistics and accretion of newly formed stars more accurately than we will be able to do with AMR alone.

Additionally we will be preparing EnzoMHD to work with the PPML method. It has been reported (A. Kritsuk, private communication) that the problems described in this work have been fixed since we began using the method described in chapter 2, and will prove to be the finest MHD code in existence.

Bibliography

André, P., Belloche, A., Motte, F., & Peretto, N. 2007, A&A, 472, 519

Anselmet, F., Gagne, Y., Hopfinger, E. J., & Antonia, R. A. 1984, Journal of Fluid Mechanics, 140, 63

Ballesteros-Paredes, J. 2006, MNRAS, 372, 443

Balsara, D. S. 2001, Journal of Computational Physics, 174, 614

Balsara, D. S. & Kim, J. 2004, ApJ, 602, 1079

Balsara, D. S. & Spicer, D. S. 1999, Journal of Computational Physics, 149, 270

Bardeen, J. M., Bond, J. R., Kaiser, N., & Szalay, A. S. 1986, ApJ, 304, 15

Berger, M. J. & Colella, P. 1989, Journal of Computational Physics, 82, 64

Bertoldi, F. & McKee, C. F. 1992, ApJ, 395, 140

Boldyrev, S., Nordlund, Å., & Padoan, P. 2002, ApJ, 573, 678

Brackbill, J. U. & Barnes, D. C. 1980, Journal of Computational Physics, 35, 426

Brio, M. & Wu, C. C. 1988, Journal of Computational Physics, 75, 400

Bryan, G. L., Norman, M. L., Stone, J. M., Cen, R., & Ostriker, J. P. 1995, Computer Physics Communications, 89, 149

Cargo, P. & Gallice, G. 1997, Journal of Computational Physics, 136, 446

Chabrier, G. 2003, PASP, 115, 763

Clark, P. C., Klessen, R. S., & Bonnell, I. A. 2007, MNRAS, 379, 57

Colella, P. & Glaz, H. M. 1985, Journal of Computational Physics, 59, 264

Colella, P. & Woodward, P. R. 1984, Journal of Computational Physics, 54, 174

Crutcher, R. M., Hakobian, N., & Troland, T. H. 2009, ApJ, 692, 844

Crutcher, R. M., Heiles, C., & Troland, T. H. 2003, Lecture Notes in Physics, Vol. 614 (Springer Berlin / Heidelberg)

Dedner, A., Kemm, F., Kröner, D., Munz, C.-D., Schnitzer, T., & Wesenberg, M. 2002, Journal of Computational Physics, 175, 645

Dib, S., Kim, J., Vázquez-Semadeni, E., Burkert, A., & Shadmehri, M. 2007, ApJ, 661, 262

Enoch, M. L., Glenn, J., Evans, II, N. J., Sargent, A. I., Young, K. E., & Huard, T. L. 2007a, ApJ, 666, 982

—. 2007b, ApJ, 666, 982

Enoch, M. L., Young, K. E., Glenn, J., Evans, II, N. J., Golwala, S., Sargent, A. I., Harvey, P., Aguirre, J., Goldin, A., Haig, D., Huard, T. L., Lange, A., Laurent, G., Maloney, P., Mauskopf, P., Rossinot, P., & Sayers, J. 2006, ApJ, 638, 293

Evans, C. R. & Hawley, J. F. 1988, ApJ, 332, 659

Falgarone, E., Troland, T. H., Crutcher, R. M., & Paubert, G. 2008, A&A, 487, 247

Fromang, S., Hennebelle, P., & Teyssier, R. 2006, A&A, 457, 371, ramses

Fryxell, B., Olson, K., Ricker, P., Timmes, F. X., Zingale, M., Lamb, D. Q., MacNeice, P., Rosner, R., Truran, J. W., & Tufo, H. 2000, ApJS, 131, 273, flash

Gardiner, T. A. & Stone, J. M. 2005, Journal of Computational Physics, 205, 509

Godunov, S. K., Zabrodin, A. V., & Prokopov, G. P. 1961, USSR Computational Math. Math. Phys., 1, 1187

Goldreich, P. & Sridhar, S. 1995, ApJ, 438, 763

Goldsmith, P. F., Heyer, M., Narayanan, G., Snell, R., Li, D., & Brunt, C. 2008, ApJ, 680, 428

Gotoh, T. & Kraichnan, R. H. 1993, Physics of Fluids, 5, 445

Harten, A. 1978, Mathematics of Computation, 32, 363

—. 1983, Journal of Computational Physics, 49, 357

Iroshnikov, P. S. 1964, Soviet Astronomy, 7, 566

Johnstone, D., Wilson, C. D., Moriarty-Schieven, G., Joncas, G., Smith, G., Gregersen, E., & Fich, M. 2000, ApJ, 545, 327

Kim, J., Ryu, D., Jones, T. W., & Hong, S. S. 1999, ApJ, 514, 506

Klessen, R. S. 2000, ApJ, 535, 869

Klessen, R. S., Heitsch, F., & Mac Low, M.-M. 2000, ApJ, 535, 887

Kolmogorov, A. N. 1941a, Doklady Akademii Nauk SSSR, 32, 16

—. 1941b, Doklady Akademii Nauk SSSR, 30, 299

—. 1991a, Proceedings of the Royal Society A, 434, 15

—. 1991b, Proceedings of the Royal Society A, 434, 9

Kraichnan, R. H. 1965, Physics of Fluids, 8, 1385

Kritsuk, A. G., Norman, M. L., Padoan, P., & Wagner, R. 2007, ApJ, 665, 416

Kritsuk, A. G. e. a. 2009

Kroupa, P. 2001, MNRAS, 322, 231

Krumholz, M. R. & McKee, C. F. 2005, ApJ, 630, 250

Laney, C. B. 1998, Computational gasdynamics (Cambridge ; New York, NY : Cambridge University Press)

Larson, R. B. 1981, MNRAS, 194, 809

Lax, P. D. 1954, Communications on Pure and Applied Mathematics, 7, 159

Lemaster, M. N. & Stone, J. M. 2008, ApJL, 682, L97

Li, P. S., Norman, M. L., Mac Low, M.-M., & Heitsch, F. 2004, ApJ, 605, 800

Li, S. 2005, Journal of Computational Physics, 203, 344

Li, S., Li, H., & Cen, R. 2008, ApJS, 174, 1

Lunttila, T., Padoan, P., Juvela, M., & Nordlund, Å. 2008, ApJL, 686, L91

Mac Low, M.-M. 1999, ApJ, 524, 169

Mac Low, M.-M. & Klessen, R. S. 2004, Reviews of Modern Physics, 76, 125

Matzner, C. D. & McKee, C. F. 2000, ApJ, 545, 364

McKee, C. F. & Ostriker, E. C. 2007, ARA&A, 45, 565

McKee, C. F. & Williams, J. P. 1997, ApJ, 476, 144

McKee, C. F. & Zweibel, E. G. 1995, ApJ, 440, 686

Mignone, A. 2007, Journal of Computational Physics, 225, 1427

Miyoshi, T. & Kusano, K. 2005, AGU Fall Meeting Abstracts, B1295+

Motte, F., Andre, P., & Neri, R. 1998, A&A, 336, 150

Mouschovias, T. C. 1976, ApJ, 207, 141

Mouschovias, T. C. 1987a, in NATO ASIC Proc. 210: Physical Processes in Interstellar Clouds, ed. G. E. Morfill & M. Scholer, 453–489

Mouschovias, T. C. 1987b, in NATO ASIC Proc. 210: Physical Processes in Interstellar Clouds, ed. G. E. Morfill & M. Scholer, 491–552

Müller, W.-C. 2009, Lecture Notes in Physics, Vol. 756 (Springer Berlin / Heidelberg), 223–254

Müller, W.-C. & Biskamp, D. 2000, Physical Review Letters, 84, 475

Nordlund, Å. K. & Padoan, P. 1999, in Interstellar Turbulence, ed. J. Franco & A. Carraminana, 218–+

Norman, M. L., Bryan, G. L., Harkness, R., Bordner, J., Reynolds, D., O'Shea, B., & Wagner, R. 2007

Orszag, S. A. & Tang, C.-M. 1979, Journal of Fluid Mechanics, 90, 129

Ostriker, E. C., Stone, J. M., & Gammie, C. F. 2001, ApJ, 546, 980

Padoan, P. 1995, MNRAS, 277, 377

Padoan, P., Bally, J., Billawala, Y., Juvela, M., & Nordlund, Å. 1999, ApJ, 525, 318

Padoan, P., Jones, B. J. T., & Nordlund, A. P. 1997a, ApJ, 474, 730

Padoan, P., Juvela, M., Kritsuk, A., & Norman, M. L. 2006, ApJL, 653, L125

Padoan, P. & Nordlund, Å. 1999, ApJ, 526, 279

—. 2002, ApJ, 576, 870

—. 2004, ApJ, 617, 559

Padoan, P., Nordlund, A., & Jones, B. J. T. 1997b, MNRAS, 288, 145

—. 1997c, MNRAS, 288, 145

Padoan, P., Nordlund, Å., Kritsuk, A. G., Norman, M. L., & Li, P. S. 2007, ApJ, 661, 972

Passot, T., Pouquet, A., & Woodward, P. 1988, A&A, 197, 228

Passot, T. & Vázquez-Semadeni, E. 1998, Phys Rev E, 58, 4501

Powell, K. G., Roe, P. L., Linde, T. J., Gombosi, T. I., & de Zeeuw, D. L. 1999, Journal of Computational Physics, 154, 284

Roe, P. L. 1981, Journal of Computational Physics, 43, 357

Rosolowsky, E. W., Pineda, J. E., Kauffmann, J., & Goodman, A. A. 2008, ApJ, 679, 1338

Rosswog, S. & Price, D. 2007, MNRAS, 379, 915, mAGMA, proxy for Phantom-SPH

Ryu, D. & Jones, T. W. 1995, ApJ, 442, 228

Ryu, D., Miniati, F., Jones, T. W., & Frank, A. 1998, ApJ, 509, 244

Ryu, D., Ostriker, J. P., Kang, H., & Cen, R. 1993, ApJ, 414, 1

Salpeter, E. E. 1955, ApJ, 121, 161

Saltzman, J. 1994, Journal of Computational Physics, 115, 153

Scalo, J., Vazquez-Semadeni, E., Chappell, D., & Passot, T. 1998, ApJ, 504, 835

She, Z.-S. & Leveque, E. 1994, Physical Review Letters, 72, 336

Shu, F. H., Adams, F. C., & Lizano, S. 1987, ARA&A, 25, 23

Slyz, A. D., Devriendt, J. E. G., Bryan, G., & Silk, J. 2005, MNRAS, 356, 737

Solomon, P. M., Rivolo, A. R., Barrett, J., & Yahil, A. 1987, ApJ, 319, 730

Sridhar, S. & Goldreich, P. 1994, ApJ, 432, 612

Stone, J. M. & Norman, M. L. 1992, ApJS, 80, 791

Toro, e. 1999, Riemann Solvers and Numerical Methods for Fluid Dynamics: A Practical Introduction (Springer, Berlin, New York)

Troland, T. H. & Crutcher, R. M. 2008, ApJ, 680, 457

Truelove, J. K., Klein, R. I., McKee, C. F., Holliman, II, J. H., Howell, L. H., & Greenough, J. A. 1997, ApJL, 489, L179+

Turk, M. 2008, in Proceedings of the 7th Python in Science Conference, ed. G. Varoquaux, T. Vaught, & J. Millman, Pasadena, CA USA, 46 – 50

Ustyugov, S. & Popov, M. 2008, submitted to *Journal of Computational Physics*

Vazquez-Semadeni, E. 1994, ApJ, 423, 681

Vázquez-Semadeni, E., González, R. F., Ballesteros-Paredes, J., Gazol, A., & Kim, J. 2008, MNRAS, 390, 769

Vázquez-Semadeni, E., Kim, J., Shadmehri, M., & Ballesteros-Paredes, J. 2005, ApJ, 618, 344

Vincent, A. & Meneguzzi, M. 1991, Journal of Fluid Mechanics, 225, 1

Williams, J. P., de Geus, E. J., & Blitz, L. 1994, ApJ, 428, 693

Williams, J. P. & McKee, C. F. 1997, ApJ, 476, 166

Young, K. E., Enoch, M. L., Evans, II, N. J., Glenn, J., Sargent, A., Huard, T. L., Aguirre, J., Golwala, S., Haig, D., Harvey, P., Laurent, G., Mauskopf, P., & Sayers, J. 2006, ApJ, 644, 326

Zuckerman, B. & Evans, II, N. J. 1974, ApJL, 192, L149